

PL-TR-96-2258

**AN INTEGRATED STUDY OF LITHOSPHERIC
STRUCTURE, REGIONAL SEISMIC WAVE
PROPAGATION, AND SEISMIC DISCRIMINATION
CAPABILITY IN THE MIDDLE EAST**

Keith Priestley

**University of Cambridge
Department of Earth Sciences
Madingley Rise, Madingley Road
Cambridge CB3 OEZ, UNITED KINGDOM**

7 October 1996

Scientific Report No. 1

APPROVED FOR PUBLIC RELEASE; DISTRIBUTION UNLIMITED



**PHILLIPS LABORATORY
Directorate of Geophysics
AIR FORCE MATERIEL COMMAND
HANSCOM AFB, MA 01731-3010**



**DEPARTMENT OF ENERGY
OFFICE OF NON-PROLIFERATION AND
NATIONAL SECURITY
WASHINGTON, DC 20585**

DTIC QUALITY INSPECTED 3

19961209 003

SPONSORED BY
Department of Energy
Office of Non-Proliferation and National Security

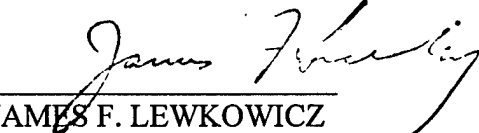
MONITORED BY
Phillips Laboratory
CONTRACT No. F19628-95-K-0017

The views and conclusions contained in this document are those of the authors and should not be interpreted as representing the official policies, either express or implied, of the Air Force or U.S. Government.

This technical report has been reviewed and is approved for publication.



DELAINE REITER
Contract Manager
Earth Sciences Division



JAMES F. LEWKOWICZ
Director
Earth Sciences Division

This report has been reviewed by the ESD Public Affairs Office (PA) and is releasable to the National Technical Information Service (NTIS).

Qualified requestors may obtain copies from the Defense Technical Information Center.
All others should apply to the National Technical Information Service.

If your address has changed, or you wish to be removed from the mailing list, or if the addressee is no longer employed by your organization, please notify PL/IM, 29 Randolph Road, Hanscom AFB, MA 01731-3010. This will assist us in maintaining a current mailing list.

Do not return copies of this report unless contractual obligations or notices on a specific document requires that it be returned.

REPORT DOCUMENTATION PAGE			Form Approved OMB No. 0704-0188
<p>Public reporting burden for this collection of information is estimated to average 1 hour per response, including the time for reviewing instructions, searching existing data sources, gathering and maintaining the data needed, and completing and reviewing the collection of information. Send comments regarding this burden estimate or any other aspect of this collection of information, including suggestions for reducing this burden, to Washington Headquarters Services, Directorate for Information Operations and Reports, 1215 Jefferson Davis Highway, Suite 1204, Arlington, VA 22202-4302, and to the Office of Management and Budget, Paperwork Reduction Project (0704-0188), Washington, DC 20503.</p>			
1. AGENCY USE ONLY (Leave blank)	2. REPORT DATE	3. REPORT TYPE AND DATES COVERED	
	7 October 1996	Scientific Report No. 1	
4. TITLE AND SUBTITLE	An Integrated Study of Lithospheric Structure, Regional Seismic Wave Propagation, and Seismic Discrimination Capability in the Middle East		5. FUNDING NUMBERS
6. AUTHOR(S)	Keith Priestley		PE 6912OH PR DENN TA GM WU AD Contract F19628-95-K-0017
7. PERFORMING ORGANIZATION NAME(S) AND ADDRESS(ES)	University of Cambridge Department of Earth Sciences Madingley Rise, Madingley road Cambridge CB3 OEZ, UNITED KINGDOM		8. PERFORMING ORGANIZATION REPORT NUMBER
9. SPONSORING/MONITORING AGENCY NAME(S) AND ADDRESS(ES)	Phillips Laboratory 29 Randolph Road Hanscom AFB, MA 01731-3010		10. SPONSORING/MONITORING AGENCY REPORT NUMBER
11. SUPPLEMENTARY NOTES			PL-TR-96-2258
Contract Manager: Delaine Reiter/GPE			
12a. DISTRIBUTION AVAILABILITY STATEMENT		12b. DISTRIBUTION CODE	
Approved for public release; distribution unlimited			
13. ABSTRACT (Maximum 200 words) <p>The upper mantle compressional wave velocity beneath the Iranian Plateau is determined by measuring two station interval velocities from first arrivals in the distance range 2 to 18 degrees reported in the ISC. The Pn velocity is near 8.1 km/s beneath the Zagros Mts. and most of the northern part of the plateau. A lower Pn velocity of about 7.8 km/s occur beneath NW Iran. Additional Pn velocity estimates are made using recordings of well located aftershocks, and these confirm the two station Pn velocity measurements. A new 1-D earth model for the crust and upper mantle beneath the Archaean core of southern Africa is determined. Below the 42-km thick crust there is an 80-km thick upper mantle lid. Vp and Vs are 8.09 and 4.62 km/s, respectively, at the top of the lid and the compressional and shear velocity gradients through the lid are 0.0008/s and 0.0013/s, respectively. Below the lid there is a substantial shear wave LVZ. Velocities and densities in the seismic model of the lid closely agree with velocity and density estimates from geochemical analysis of garnet peridotite nodules from kimberlites on the Kaapvaal Craton, implying that the estimates from kimberlites are representative of a wider region of the Archaean core of southern Africa.</p>			
14. SUBJECT TERMS		15. NUMBER OF PAGES	
Seismic studies	Upper mantle structure	128	
Iranian plateau	Crustal structure	16. PRICE CODE	
17. SECURITY CLASSIFICATION OF REPORT	18. SECURITY CLASSIFICATION OF THIS PAGE	19. SECURITY CLASSIFICATION OF ABSTRACT	20. LIMITATION OF ABSTRACT
Unclassified	Unclassified	Unclassified	SAR

CONTENTS

UPPER MANTLE COMPRESSIONAL WAVE VELOCITY BENEATH IRAN

Introduction	1
Interval Velocity Estimates Using ISC Arrival Times	2
Data	4
Results	4
Assessment of Errors	5
P_n Velocity Estimates From ILPA Recordings of the Tabas Aftershocks	9
P_n Velocity Estimates From ISC Arrival Times of Large Well-Recorded Regional Events	9
References	10

AVERAGE LITHOSPHERIC STRUCTURE OF SOUTHERN AFRICA

1. Introduction	31
2. Geological and Geophysical Characteristics of Southern Africa	31
3. Determination of the Velocity and Density Structure of the Southern African Crust and Upper Mantle	32
3.1 Data and Method of Analysis	32
3.2 Velocity Structure of the Southern African Crust	33
3.3 Velocity Structure of the Southern African Mantle	35
3.3.1 Body-wave Constraints	35
3.3.2 Modeling of Regional Surface Waves	36
3.3.3 Modeling of P_{nl} Waveforms	37
3.3.4 One-dimensional Earth Model for the Southern African Craton	38
4. Discussion	39
4.1 Comparison Seismically Determined Velocities With Those Estimated From Kimberlite Nodule Data	39
4.2 Geological Implications of the Velocity Structure	40
4.3 Comparison With Previous Southern African Seismological Models	41
4.4 Comparison With Other Earth Models for Shield Regions	42

5. Conclusions	43
References	44
Appendix A: Teleseismic Receiver Function Analysis	73
Appendix B: Regional Waveform Analysis	81
Appendix C: Physical Properties	113

UPPER MANTLE COMPRESSIONAL WAVE VELOCITY BENEATH IRAN

by Keith Priestley

ABSTRACT

The upper mantle compressional wave velocity beneath the Iranian Plateau has been determined by measuring two station interval velocities from first arrivals in the distance range 2° to 18° reported in the Bulletin of the International Seismological Centre (ISC). These results show that the P_n velocity is near 8.1 km/sec beneath the Zagros Mountains and most of the northern part of the Iranian Plateau and is not as variable as reported in past studies. A lower P_n velocity of about 7.8 km/sec occur beneath northwestern Iran. The magnitude of various sources of error are discussed. Teleseismic P-wave delays are used to estimate the crustal delays and the apparent P_n velocities are corrected. Additional P_n velocity estimates are made using digital recordings of well located aftershocks of the 1978 Tabas earthquake in northeastern Iran from the Iranian Long Period Array. P_n velocity from the aftershock seismograms confirm the two station P_n velocity measurements from the ISC data. Using ISC travel times from events with focal depths constrained by waveform modelling proved to still have too great a scatter to refine the P_n velocity estimates over previous single station measurements in this region.

INTRODUCTION

This study attempts to refine the measurement of upper mantle compressional velocity beneath the high topographic region of Iran. Accurate P_n velocity estimates are an important parameter in locating small magnitude events in this region since most such events are located with a few seismographs at regional distance ranges. Several previous studies have estimated the P_n velocity in this region but the results are conflicting. For example Chen et al (1980), Kadinsky-Cade et al (1981) and Hearn & Ni (1994) all find low upper mantle velocity in the region of the Turkish-Iranian border NW of the station TAB (Fig. 1), but SE of TAB in Iran Chen et al (1980) and Asudeh (1982a) find the P_n velocity to be about 7.8 km/sec while Kadinsky-Cade et al (1981) find the P_n velocity to be 8.6 km/sec.

Seismologists use the term P_n for two distinctly different seismic phases. In controlled source refraction experiments the term P_n is used to denote the headwave propagating immediately beneath the Moho. The apparent velocity of this phase in the case of plane,

horizontal layers is equivalent to the upper mantle velocity directly beneath the Moho. Depending on the upper mantle velocity gradient (Hill, 1971), the P_n headwave can be observed to a distance of several hundred kilometers, after which it is typically replaced by sets of delayed arrivals with a similar apparent velocity (Hirn et al, 1973). Earthquake seismologists use the term P_n to denote the first arrival from earthquakes in the distance range from about 200 km to as great as 2000 km. Beyond about 2000 km the P_n phase is replaced as the first arrival by direct P turning below the 410-discontinuity, but P_n can often be observed as a secondary arrival to greater distance. This regional distance range seismic phase has nearly constant phase velocity over this entire distance range. This second sense of the term P_n is used in this work.

In an area such as Iran, the determination of upper mantle velocities must depend on seismograms from earthquakes. However it is well known that earthquakes, especially smaller events ($m_b < 5$), are poorly located (Asudeh, 1983). Many regions in Iran have high seismicity but the seismograph density is too low to permit the simultaneous solution for the velocity and hypocentral parameters. In this study I have examined three ways of improving the estimates of the upper mantle compressional velocity: (a) using two station interval velocity measurements from regional arrival times reported by the Bulletin of the International Seismological Center (ISC); (b) using digital recordings of well located aftershocks of the Tabas earthquake; and (c) using ISC arrival time data from moderate events whose focal depths are constrained by waveform modelling.

Interval Velocity Estimates Using ISC Arrival Times

METHOD

The two station interval velocity method is a modified form of the time-term method of Scheidegger & Willmore (1957) and Willmore & Bancroft (1960). Several studies have used this method to estimate uppermost mantle velocity from arrival times reported by the ISC (Asudeh, 1982a; Beghoul & Barazangi, 1989) or other networks (Haines, 1979, 1980; Kayal & Smith, 1984; Kayal & Reena De, 1987). Asudeh (1982a) used ISC arrival time data from Iranian seismographs to determine P_n velocity along several paths to a precision of considerably better than 0.1 km/sec.

If two seismographs S_1 and S_2 lie on the same great circle path as an earthquake (Fig. 2), then the apparent upper mantle velocity, c , between the two stations is given by

$$c = \frac{\Delta_2 - \Delta_1}{T_2 - T_1} \quad (1)$$

where $\Delta_{1,2}$ is the epicentral distance and $T_{1,2}$ is the arrival time at the seismographs 1 and 2, respectively. If Δ is in the range of a few degrees the curvature of the Earth may be ignored

and if the crustal delays are the same beneath both stations, the uppermost mantle velocity, v , between the two stations is equal to the apparent velocity,

$$v = c = \frac{\Delta}{T} . \quad (2)$$

where Δ and T are the difference in epicentral distance and arrival time, respectively. Errors in the focal depth and origin time are eliminated by taking the arrival time difference in (1). If the crustal thickness or velocity varies beneath the two seismographs then different apparent velocities will be observed along the forward and reversed path. In this case the true upper mantle velocity will be approximately the average of the forward and reversed apparent velocities.

Earthquakes in Iran are known to be poorly located by the ISC (Asudeh, 1983). Location errors will map into errors in the measured velocity. These probably account for much of the scatter in travel time curves derived from a single station when the ISC locations are used, even when the arrival times are determined from the original records (Chen et al, 1980; Kadinsky-Cade et al, 1981). Asudeh (1982a) and Beghou & Barazangi (1989) have shown that the two station method minimized the effect of location errors. Following Asudeh (1982a), if E' (Fig. 2) is the epicenter reported by the ISC and E is the true epicenter, then EE' (with components δx , δy , and δz) is the mislocation vector. The effect of δx and δz cancel in taking the arrival time difference $T_2 - T_1$ and distance difference $\Delta_2 - \Delta_1$, and only the component δy perpendicular to the great circle path will affect the velocity calculation. From Figure 2

$$\sin \Psi = \frac{\delta y}{\Delta_1} . \quad (3)$$

Small errors in the location and interstation travel time leads to errors in the velocity, δv . From (2) and (3)

$$v \approx \frac{\Delta \cos \Psi}{T} , \quad (4)$$

thus

$$\delta v = \frac{-\Delta \cos \Psi}{T^2} \cdot \delta T - \frac{\Delta}{T} \sin \Psi \cdot \delta \Theta . \quad (5)$$

For magnitude 4.5 to 5 events in Iran the mislocation vector EE' is likely to be 10 to 20 km (Asudeh, 1983). The crust beneath the Iranian plateau is 40 to 50 km thick (Asudeh, 1982b) therefore Δ_1 is about 200 km. For Δ_1 greater than about 400 km, which is more typical of the events used in this study, the error introduced by the second term on the right-hand side of (5) is less than 0.01 km/s (Asudeh, 1982a) and can be ignored and (5) reduces to

$$\delta v = \frac{-\Delta \cos \Theta}{T^2} \cdot \delta T \quad . \quad (6)$$

Thus errors in the epicenter have a small effect on the velocity calculation; errors in the focal depth and origin time cancel entirely. In the absence of clock errors, δT reflects timing errors which should be normally distributed and hence should be reduced by repeated measurement. Also, the magnitude of δv is inversely proportional to T , so large Δ which give large T lead to more accurate velocity estimates. For $\Delta \approx 700$ km and $P_n \approx 8.1$ km/sec which is typical in this study, a one-second reading error gives less than 0.1 km/sec error in the P_n velocity.

DATA

Data for the two station interval velocity measurements have been taken from the ISC CD-rom. This includes data from January 1, 1964 to August 31, 1987. Arrival time data for the sixteen stations in Iran, eastern Iraq, and southern Azerbaijan shown in Figure 1 were used (Table 1). All crustal events for which (a) the ISC had used at least 25 stations in the location, (b) the stations lay within the epicentral distance range 2° to 18° , and (c) whose travel time residual was less than 5 seconds were chosen. The first restriction ensured that the epicenters were reasonably well located. In most cases the number of locating stations was much greater than 25. The second restriction ensured that the first arrival was in the P_n distance range. Timing errors are common in the ISC arrival data. Many of these are obvious 10 and 60 second notation errors. The third restriction removes the affect of these large timing errors. To obtain a large number of arrival time data the requirement that the event and two stations lie on the same great circle path was relaxed. Both Asudeh (1982a) and Beghoul & Barazangi (1989) allowed the opening angle Θ (Fig. 2) to be 6° . In this study Θ equal 7° was used in selecting events. The increased error from using this larger value of Θ is probably insignificant compared to that from using 6° as in Beghoul & Barazangi (1989) and $\Theta = 7^\circ$ seems to correspond to what Asudeh (1982a) actually used to obtain the events he shows in his Table 1. The selection criteria will be discussed further below when the effects of errors are assessed.

RESULTS

The routines for selecting the data from the ISC file and for computing the two station interval velocity were first tested to reproduce the results in Table 1 of Asudeh (1982a). Other than specifying a maximum opening angle of 6° , Asudeh (1982a) does not cite his criteria for choosing his data. Using the portion of the ISC data between July 26, 1967 and October 2, 1976, a number of test selections were made to determine the criteria Asudeh used. To select the seven events in his Table 1 required $\Theta = 7^\circ$, travel time residuals less than 5.5 seconds, and ISC focal depths to 57 km. Many ISC focal depths for events in Iran are sub-Moho but there is no reliable evidence for mantle events except in the Makran (Jackson & Fitch, 1981). There are a large number of events which occur during this time period

which also satisfy these selection criteria but which Asudeh did not use and he does not comment why the events in his Table 1 were chosen and the other events rejected. Using the arrival time data from the CD-rom, phase velocity values were determined to within ± 0.02 km/sec for six of the seven values shown in Table 1 of Asudeh (1982a), but the apparent velocity of the October 2, 1976 event was nearly 0.4 km/sec. The arrival time difference for this event in Table 1 of Asudeh (1982a) is wrong by 4 seconds.

The two station interval velocity measurements are show as a function of position and direction in Figure 3. These values plus their average error are tabulated in Table 1. Northern Iran is well sampled, however, the values for central Iran all depend on the WWSSN station SHI. The apparent P_n velocity in central and NE Iran is 8.1 ± 0.1 km/sec. Beneath the Talesh and Albroz Mountains along the Iranian shore of the Caspian Sea and in NW Iran near the Turkish border, the P_n velocity is less than 8.0 km/sec. The apparent P_n velocity measurements in Figure 3 suggest less variability in the upper mantle compressional wave velocity than found in previous studies. The velocity average errors in Table 2 are significantly larger than those reported in Asudeh (1982a). Ignoring the error in his Table 1, the lower errors he reports seem to arise from the way he has culled the data.

ACCESSION of ERRORS

The effect of epicentral mislocations has been discussed above. However, there are several other potential sources of error in the procedure outlined above.

Effect of Spherical Wave Front: For Θ greater than zero, the true curved wavefront arrives at the distant station at a later time than if the wavefront was planar as assumed. Beghoul & Barazangi (1989) show that this difference in distance is given by

$$HH' = \Delta_2 - \Delta_1 \sin^2 \Theta - \cos \Theta \sqrt{(\Delta_2)^2 - (\Delta_1)^2 \sin^2 \Theta} \quad (7)$$

and that for Θ equal 6° and an interstation distance of 14° HH' is 7.4 km which leads to less than a 0.5% error in the estimated P_n velocity. Thus neglecting the wavefront curvature leads to insignificant error.

Effect of Variation in Θ : There is a trade-off in choosing Θ . To obtain a large number of events to make the interval velocity estimates, larger Θ is desirable. However, larger Θ couples with epicentral mislocation to produce larger errors in the apparent P_n velocity. Beghoul & Barazangi (1989) constrained Θ to 6° and from tests of the data in Table 1 of Asudeh (1982) he appears to have let Θ be at least 7° . Figure 4 shows the combined effect of varying Θ and epicentral mislocation. The magnitude of the error decreases with increasing distance. Figure 4a shows the error for Θ of 14° and an epicentral mislocation of 28 km (20 km perpendicular to the interstation line and 20 km in line with the interstation line). Figure 4b assumes the same epicentral mislocation, but is for Θ of 7° and is the data used

in measuring the apparent P_n velocities shown in Figure 3. For this Θ and for an assumed epicentral mislocation of 28 km, which should be representative for the Middle East events used in this study, the error is less than 1.5%.

Effect of Lid Velocity Gradient: The propagation of the mantle lid P-wave is primarily controlled by the lid compressional wave velocity gradient including the pseudo-velocity gradient caused by Earth sphericity. Braile & Smith (1975) used reflectivity synthetic seismograms to show the effect of the velocity gradient directly below the Moho on P_n propagation. Even in the presence small negative velocity gradient in the lid, the pesudo-gradient as a result of curvature results in turning rays in the lid and P_n propagates to distances of 400 to 700 km. P_n is not observed only in cases where the negative gradient is enough to off-set that resulting from curvature. Menke & Richards (1980) modelled teleseismic P_n as a sum of whispering gallery waves which propagate in a waveguide composed of the high velocity mantle lid overlying the upper mantle low velocity zone. The velocity gradient of the lid, including the pseudo-gradient resulting from Earth curvature, is the most important parameter controlling propagation and both crustal structure and upper mantle velocity are of secondary importance. Lid velocity structures which have weak velocity gradients have nearly constant apparent velocity with increasing range. The observation that P_n falls along a linear travel-time branch suggests that velocity gradient in the mantle lid is low and hence the P_n velocity found at larger distances is representative of the true upper mantle material speed.

The two station method assumes that both stations record the same phase. If a strong positive velocity gradient exist in the mantle lid then the two station P_n velocity estimate would depend on the epicentral distance of the two stations since the near station would be recording a shallow turning phase while the far station recorded a deeper turning phase. To estimate the strength of the lid gradient beneath the Middle East, travel times for all stations in the distance range 2° - 25° were plotted as a reduced travel time curve. Travel time curves for four stations are shown in Figure 5. These, and those for the other twelve stations not shown, indicate that the first arrival in the distance range from about 2° to about 18° fall on a linear travel time branch. Based on this observation, only events more than 200 km from the near station and less than 1800 km from the far station were used in computing the apparent P_n velocity.

Table 3 gives the intercept times for the ISC arrival time data for each of the stations. In computing these intercept times, only arrivals from events in the distance range 250 to 1600 km with residuals less than 5 seconds were used.

Effect of crustal delay times beneath the stations: The source crustal delay term is common to the arrival times at both stations and therefore cancels when taking the time difference in the interval velocity calculation. In the case of a crust of uniform thickness and velocity, the apparent P_n velocity from the two station interval velocity measurement would be equivalent

to the upper mantle compressional wave velocity. In the case where the crustal structure changes between receivers but where reversed apparent velocity estimates are available, the upper mantle velocity is approximately the average of the two way measurements. However, variations in crustal thickness or crustal velocity in the vicinity of the receivers, neither of which are known for Iran, can combine to produce time delays which would bias the estimate of the P_n velocity. Even though the crustal structure of Iran is poorly known we can make some estimate of the magnitude of the effects of the crustal delays. The magnitude of the effect of crustal structure variation depends on the path length between the two stations. For a path length of 250 km, replacing 5 km of crust of velocity 6.1 km/sec with upper mantle material of velocity 8.1 km/sec changes the estimated P_n velocity from the true velocity of 8.10 km/sec to 8.18 km/sec but for a path length of 750 km a 5 km thinning of the crust only changes the estimated P_n velocity to 8.12 km/sec.

One estimate of the variation in crustal delay terms exist through comparing relative teleseismic delay times across Iran. Figure 6 (Table 4) is a plot of the teleseismic delay times at 15 seismographs relative to the station SHI in the Zagros Mountains. These residuals were determined by finding the mean of the difference in the P-wave residual at a recording station minus the residual at station SHI. Station SHI was chosen because it had the largest number of recordings. Only events greater than 35° distance and which were not emergent arrivals were used. With one exception, Figure 6 shows a very consistent pattern. Except for the station MSH, all the stations in eastern Iran show relative residuals of about 0.55 ± 0.15 second. Four stations MSH, MHI, MAIO, and MUI are located close together at Mashhad. MHI and MAIO are co-located and have similar relative travel time residuals. MUI and MSH are located about 15 km from MHI and MAIO, and about 2 km from each other. MUI has a relative residual similar to that at MHI/MAIO but the delay at MSH is much greater. Dziewonski & Anderson (1983) examined teleseismic P-wave residuals from the ISC arrival time data and found that MSH showed much larger delays than nearby stations. MSH also produces anomalously low velocity estimates from the first arrival of regional earthquakes. Without knowing more details of the site condition at MSH, it is impossible to determine whether the station has a large relative residual compared to nearby stations due to site condition, such as being located above a sedimentary basin, or whether other factors contribute to the larger delay at MSH. Since MSH produced no interval velocity estimates which fell in the P_n velocity range and since MSH shows more than a half second larger delay compared to the nearby stations, data from MSH has not been used in this study. There is about a half second relative delay from the northeastern Iranian stations compared to the Zagros Mountains stations. If this is solely do to crustal thinning this would imply that the crust beneath the Zagros is about 5 km thinner than the crust beneath northeast Iran. However, both lower crust or upper mantle velocity beneath NE Iran could contribute to their delays.

The three stations in northern Iran south of the Caspian Sea (TEH, ILPA, SRI) show

similar teleseismic delays of about 1 second relative to SHI. If the crustal velocities in the two regions are similar, the crust beneath the Alborz Mountains is about 10 km thicker than the crust beneath the Zagros Mountains. The station TAB in northwest Iran and the nearby station LNK in southeastern Azerbaijan show similar delays of about 1.45 seconds, although there are few arrival times for the LNK station. TAB is in a region of recent volcanism and this has previously been cited as a possible explanation for the low P_n velocities reported in this area (Chen et al, 1980; Kadinsky-Cade et al, 1981; Asudeh, 1982a). This might also explain part of the large teleseismic delay observed at TAB relative to SHI. However the delay at TAB is identical to that observed at LNK 200 km ENE.

LNK is the only station in this region where the crustal structure beneath the station is well known. Mangino & Priestley (1996) have analyzed broadband teleseismic waveforms from a digital seismograph co-located with the analogue seismograph which reports arrival times to the ISC. To determine the crustal structure they have inverted radial receiver function data using the routine of Ammon et al (1990), then forward modelled the radial receiver function to assess which features of the inversion model were significant. The results of this analysis for LNK are summarized in Figure 7. The inversion results (Fig. 7a) imply the presence of a low velocity ($V_p < 4.8$ km/s) upper most crust (0-6 km), a large (>2.0 km/s) velocity contrast between 6-12 km depth, a high velocity ($V_p 7.0$ km/s) mid- to lower-crust and a complex crust-mantle boundary. Between 8-12s the amplitude of the tangential component is about equal to that of the radial and there is a negative gradient between 20-25 km depth which is producing the synthetic radial motion at this time. The forward modelling result (Fig. 7b) shows that the main features of the radial receiver function can be fit with a much more simple crustal velocity model. Thus the LNK teleseismic delay is largely the result of the low velocity upper crust. This is not likely to be representative of the structures in the Zagros Mountains and the Iranian plateau.

The actual crustal thickness is not important. If the teleseismic delays in Figure 6 are the result of varying crustal thickness or crustal velocity and not from varying upper mantle velocity, then a crude correction of the apparent P_n velocities can be made by converting the teleseismic crustal delay into an equivalent crustal delay for P_n . Waveform modelling of regional seismic waveforms of central and southern Iran earthquakes digitally recorded on stations of the Caspian Seismic Network (Priestley, work in progress), and receiver function analysis for a seismograph station within 1 km of the Iran border in Turkmenistan (Mangino & Priestley, 1996) show that the average crustal velocity in the Iranian plateau is about 6.1 km/sec which is low for continental crust. Using this and an average P_n velocity of 8.1 km/sec gives a critical angle for P_n of 48.9° . The ratio of the teleseismic delay to the P_n delay is inversely proportional to the ratio of the cosine of the teleseismic emergent angle to the cosine of the P_n critical angle, which in this case is 1.42. Using this factor, the teleseismic delays were converted to equivalent P_n crustal delay and the P_n velocities shown in Figure 3 were corrected.

Figure 8 plots these corrected apparent P_n velocities and the average of the two-way measurements. Over most of the Zagros Mountains and the Iranian plateau the P_n velocity is 8.05 ± 0.10 km/sec. In northwest Iran the P_n velocity is 7.79 ± 0.10 km/sec, significantly lower than in central Iran.

P_n Velocity Estimates from ILPA Recordings of the Tabas Aftershocks

The September 16, 1978 Tabas-e-Golshan (M_S 7.7) earthquake in central Iran was followed by a large aftershocks sequence. The University of Cambridge deployed a local seismic array of nine stations in the epicentral region on September 28 and maintained this network until October 28. 1560 aftershocks were located and of these, 329 are thought to have uncertainties in the hypocenter of about 1 km in the epicenter and 2 km in focal depth. Many of these have well constrained focal mechanisms. The ILPA array (≈ 650 km distance) was in partial operation for most of this period and ILPA recordings of these aftershocks provide support for the P_n velocity from the two station ISC data. Figure 9 is a composite record section consisting of seismograms of several Tabas aftershocks recorded across the IPLA array. The aftershocks range in focal depth from 10 to 18 km, but have been normalized to 12 km depth (the median focal depth) using a average crustal P-wave velocity of 6.1 km/sec and a P_n velocity of 8.1 km/sec. The travel times have been reduced by $\Delta/8.1$ seconds and the line is for a velocity of 8.1 km/sec. This combination of sources and receivers averages the P_n velocity both beneath the region of the Tabas sequence and the ILPA array. The 8.1 km/sec line closely matches the first arrivals. Other plots of multiple aftershocks recorded at a single ILPA array element suggest that the apparent P_n velocity beneath the aftershock sequence may be slightly less and the apparent P_n velocity across the array from a single aftershock suggest that the P_n velocity beneath the array may be slightly higher. However, these differences are probably not significant.

P_n Velocity Estimates from ISC Arrival Times of Large Well Recorded Regional Events

A third method of refining the P_n velocity beneath Iran was explored but proved unfruitful. There have been several studies of the mechanisms of moderate to large earthquakes in the region of Iran using waveform modelling (Baker et al, 1993, Baker, 1993, Priestley et al, 1994). Besides the fault plane solution, the initial P-wave shape is controlled by the interference of direct P and the depth phases pP and sP. The focal depths from these studies were used with the ISC locations and the ISC first arrival times at regional seismograph stations to derive single station travel time curves corrected for source depth. Even with improved focal depth estimates, these travel time curves showed too much error to prove useful.

ACKNOWLEDGEMENTS

I would like to thank Drs. John Cipar and Anton Dainty for critically reviewing this manuscript. This research has been supported by a summer research fellowship at the Phillips Laboratory, Hanscom AFB, Ma and contract F19628-95-K-0017 from the Phillips Laboratory, Hanscom AFB, Ma.

References

Ambraseys, N.M., The relocation of epicentres in Iran, *Geophys. J. R. astr. Soc.*, **53**, 117–121, 1978.

Ammon, C., G. Randall, & G. Zandt, On the Nonuniqueness of receiver function inversions, *J. Geophys. Res.*, **95**, 15303–15318, 1990.

Asudeh, I., Pn velocities beneath Iran, *Earth Planet Sci. Lett.*, **61** 1,982a

Asudeh, I., Seismic structure of Iran from surface and body wave data, *Geophys. J. Roy. Astron. Soc.*, **71**, 715–730, 1982b.

Asudeh, I., I.S.C. Mislocation of earthquakes in Iran and geometrical residuals, *Tectono-physics*, **95**, 61–74, 1983.

Baker, C., J. Jackson, & K. Priestley, Earthquakes on the Kazerun Line in the Zagros Mountains of Iran: strike-slip faulting within a fold-and-thrust belt, *Geophys. J. Int.*, **115**, 41–61, 1993.

Baker, C., The active seismicity and tectonics of Iran, PhD dissertation, University of Cambridge library.

Beghoul, N., & M. Barazangi, Mapping high P_n velocity beneath the Colorado plateau constrain uplift models, *J. Geophys. Res.*, **94**, 7083–7104, 1989.

Berberian, M., I. Asudeh, R.G. Bilham, C.H. Scholz, and C. Soufleris, Mechanism of the main shock and the aftershock study of the Tabas-e-golshan (Iran) earthquake of September 16, 1978: A preliminary report, *Bull. Seismo. Soc. AM.*, **69**, 1851–1859, 1979.

Braile, L., & R.B. Smith, Guide to the interpretation of crustal refraction profiles, *Geophys. J. Roy. Astron. Soc.*, **40**, 145–176, 1975.

Chen, C.Y., W.P. Chen, & P. Molnar, The uppermost mantle P wave velocities beneath Turkey and Iran, *Geophys. Res. Lett.*, **7**, 77–80, 1980.

Dziewonski, A., & D. Anderson, Travel times and station corrections for P waves at teleseismic distances, *J. Geophys. Res.*, **88**, 3295–3314.

Hains, A.J., Seismic wave velocities in the uppermost mantle beneath New Zealand, *N. Z. J. Geol. Geophys.*, **22**, 245–257, 1979.

Hains, A.J., Differences in the time terms between New Zealand seismograph stations and implications for crustal structure, *N. Z. J. Geol. Geophys.*, **23**, 541–549, 1980.

Hearn, T.M., & J.F. Ni, P_n velocities beneath continental collision zones: the Turkish-Iranian Plateau, *Geophys. J. Int.*, **117**, 273–283.

Hill, D.P., Velocity gradients and anelasticity from crustal body wave amplitudes, *J. Geophys. Res.*, **76**, 3309–3325, 1971.

Hirn, A., L. Steinmetz, R. Kind, & K. Fuchs, Long range profiles in Western Europe, II. Fine structure of the lower lithosphere in France (Southern Bretange), *Z. Geophys.*, **39**, 363–384, 1973.

Jackson, J., & T. Fitch, Seismotectonic implications or relocated aftershock sequences in Iran and Turkey, *Geophys. J. R. astr. Soc.*, **57**, 209–229, 1981

Kadinsky-Cade, K., M. Barazangi, J. Oliver, & B. Isacks, Lateral variations of high-frequency seismic wave propagation at regional distances across the Turkish and Iranian Plateaus, *J. Geophys. Res.*, **86**, 9377–9396.

Kayal, J. & E. Smith, Upper mantle P-wave velocities in the southeast North Island, New Zealand, *Tectonophysics*, **104**, 115–125, 1984

Kayal, J.R., & Reena De, P_n velocity study using a temporary seismographic network in the Shillong plateau, northeast India, *Bull. Seismo. Soc. Am.*, **77**, 1718–1727, 1987.

Menke, W., & P. Richards, Crust–mantle whispering gallery phases: A deterministic model of teleseismic P_n wave propagation, *J. Geophys. Res.*, **85**, 5416–5422, 1980.

Niazi, M., I. Asudeh, G. Ballard, J. Jackson, G. King and D. McKenzie, The depth of seismicity in the Kermanshah region of the Zagros mountains (Iran), *Earth Planet. Sci. Lett.*, **40**, 270–274, 1978.

Noponen, I., & P. Heikkinen, Velocities of earthquake generated P_n waves in Japan measured by the time-term method, *Phys. Earth Planet. Inter.*, **14**, 71–76, 1977.

Priestley, K, Baker, and J. Jackson, Implications of earthquake focal mechanism data for the active tectonics of the south Caspian basin and surrounding regions, *Geophys. J. Int.*, **118**, 111–141, 1994.

Scheidegger, A. & P. Willmore, The use of a least squares method for the interpretation of data from seismic surveys, *Geophysics*, **17**, 9–22, 1957.

Willmore, P., & A. Bancroft, The time term approach to refraction seismology, *Geophys. J. R. astr. Soc.*, **3**, 419–432, 1960.

Table 1 – Station Locations

Location	Designation	Latitude (°N)	Longitude (°E)	Elevation (meters)
Baghdad, Iraq	BHD	33.2744	44.3558	32
ILPA (site 1), Iran	IR1	35.4162	50.6887	1347
ILPA (site 2), Iran	IR2	35.6628	50.8976	1172
ILPA (site 3), Iran	IR3	35.4761	51.0238	1106
ILPA (site 4), Iran	IR4	35.2387	50.9012	1373
ILPA (site 7), Iran	IR7	35.7028	50.6089	1305
Kermanshah, Iram	KER	34.3522	47.1058	1310
Kakhk, Irna	KHI	34.1433	58.6417	1600
Lenkoran, Azerbaijan	LNK	38.7100	48.7788	-2
Mashhad, Iran (SR))	MAIO	36.3000	59.4945	1150
Mashhad, Iran (WWSSN)	MHI	36.3083	59.4717	1150
Mashhad, Iran (WWSSN)	MSH	36.3111	59.5878	987
Mosul,Iraq	MSL	36.3817	43.1482	242
Mashhad University, Iran	MUI	36.3117	59.6050	1000
Shahrud, Iran	SHD	36.4333	54.9417	1500
Shiraz, Iran (WWSSN)	SHI	29.6444	52.5261	1595
Safid Rud, Iran	SRI	36.7583	49.3833	243
Tabriz, Iran (WWSSN)	TAB	38.0675	46.3267	1430
Tehran, Iran	TEH	35.7378	51.3856	1360
Taghi Ghanbar, Iran	TGI	32.9611	59.1933	1800

Table 2 – Apparent P_n Velocities

Path	Apparent Velocity	No.	Average Error	Path	Apparent Velocity	No.	Average Error
SHD to IR1	8.05	7	0.08	MHI to SHD	7.96	4	0.06
IR1 to TAB	7.83	2	0.04	MHI to SHI	8.02	10	0.04
KHI to IR2	8.15	5	0.07	TAB to MSL	8.01	5	0.13
TAB to IR2	7.72	2	0.19	SHD to TEH	7.94	10	0.14
IR2 to TAB	7.98	3	0.44	SHD to TGI	8.06	6	0.11
SHD to IR7	8.17	3	0.33	TGI to SHI	8.16	14	0.18
TAB to IR7	8.08	5	0.40	TEH to SHI	8.08	7	0.08
TGI to IR7	8.08	4	0.23	SHI to SRI	7.94	2	0.16
KER to SHI	8.21	19	0.18	SRI to SHI	8.10	15	0.08
SHI to KER	8.16	27	0.14	SRI to TAB	8.09	4	0.25
TAB to KER	7.83	8	0.13	TAB to SRI	8.10	7	0.22
TEH to KER	8.13	22	0.16	SRI to TEH	7.88	5	0.20
MHI to KHI	8.00	3	0.06	TAB to TEH	7.81	5	0.13
KHI to MHI	7.83	36	0.12	TEH to TAB	7.86	10	0.14
KHI to SHD	7.98	5	0.11	TGI to TEH	7.97	10	0.12
SHD to KHI	8.16	10	0.09	TEH to TGI	8.20	9	0.16
KHI to SHI	8.03	8	0.09	MSL to BHD	8.14	2	0.25
KHI to TEH	8.04	2	0.01	KER to BHD	7.99	3	0.29
TEH to KHI	8.24	2	0.18	MSL to KER	8.09	3	0.07
KHI to TGI	8.22	6	0.10	KER to MSL	8.03	2	0.05
TGI to KHI	7.93	4	0.19				

Table 3 - P_n Travel Time Curve Intercept

Station	No.	intercept (sec)	standard error of intercept
BHD	80	7.60	0.77
IR1	53	6.62	0.91
KER	401	7.73	0.49
KHI	533	7.70	0.30
LNK	38	5.22	1.02
MAIO	260	7.64	0.44
MHI	534	7.20	0.26
MSL	138	8.03	0.53
MUI	50	6.75	0.65
SHD	225	6.82	0.41
SHI	571	7.34	0.27
SRI	223	6.70	0.56
TAB	486	7.47	0.30
TEH	576	6.21	0.31
THI	236	6.84	0.44

Table 4 - Teleseismic Delay Terms Relative to SHI

Station	Delay (sec)	Average Error	No.
LNK	1.44	0.72	9
MAIO	0.57	0.62	383
MHI	0.52	0.73	253
MSH	1.28	0.81	869
MUI	0.64	0.59	20
KHI	0.69	0.74	120
KER	0.01	0.64	198
SRI	1.01	0.86	541
SHD	0.59	0.62	79
TAB	1.46	0.75	846
TGI	0.40	0.58	83
TEH	1.00	0.85	342
IR1	0.81	0.61	67
IR2	0.93	0.63	19
IR7	0.74	0.59	100
BHD	0.93	1.01	94
MSL	0.66	1.01	94

Figure Captions

Figure 1. Station locations shown on a topography map of the Iran region.

Figure 2. Schematic representation of the two-station method. (a) Cross section showing the P_n ray paths to the two seismographs. The base of the crust is hatched, and the vertical scale is exaggerated. (b) Map view showing a two station pair and defining the opening angle Θ . Only events at an epicentral distance greater than 250 km from the near station and less than 2000 km from the far station are used. (c) An exaggerated schematic map view showing the effect of the mislocation vector EE' .

Figure 3. Apparent P_n velocity map for the Iran region. The solid triangles denote the station locations and the arrows denote the direction of the apparent P_n velocity estimate. The dot at the tail of the arrow denotes the midpoint of the two station path and the value beside the arrow is the apparent velocity.

Figure 4. Relative errors in the P_n velocity versus average epicentral distance for two opening angle (a) $\Theta = 7^\circ$ and (b) $\Theta = 14^\circ$. A location error of 28 km (20 km perpendicular to the great circle path connecting the stations, and 20 km in line with the stations) has been assumed. The data shown in (a) are those used to compute the apparent velocities in Figure 4.

Figure 5. Travel time curves for KER, SHI, TAB, and KHI. The times have been reduced by 8 km/sec.

Figure 6. Teleseismic delays in seconds relative to the station SHI.

Figure 7. Receiver function structure for LNK. (a) Inversion crustal model, (b) Simplified crustal model from forward modelling of the main features of the receiver function.

Figure 8. Two-way and crustal delay time corrected P_n velocity map. The one-way, delay time corrected P_n values are shown in parentheses.

Figure 9. Record section from ILPA recordings of the Tabas aftershocks. Depths of the events have been normalized to 12 km and the times have been reduced by $\Delta/8.1$ seconds.

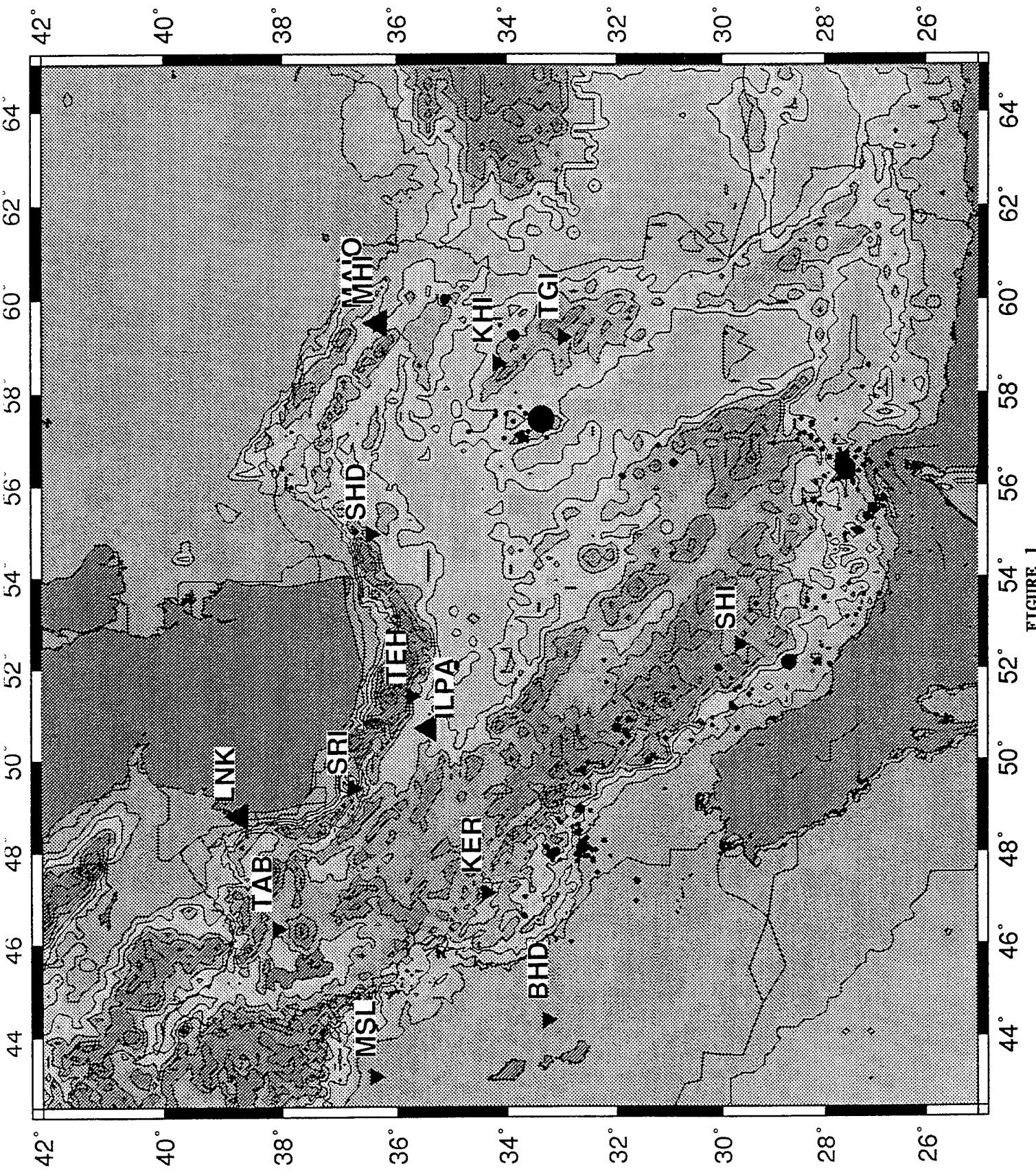


FIGURE 1

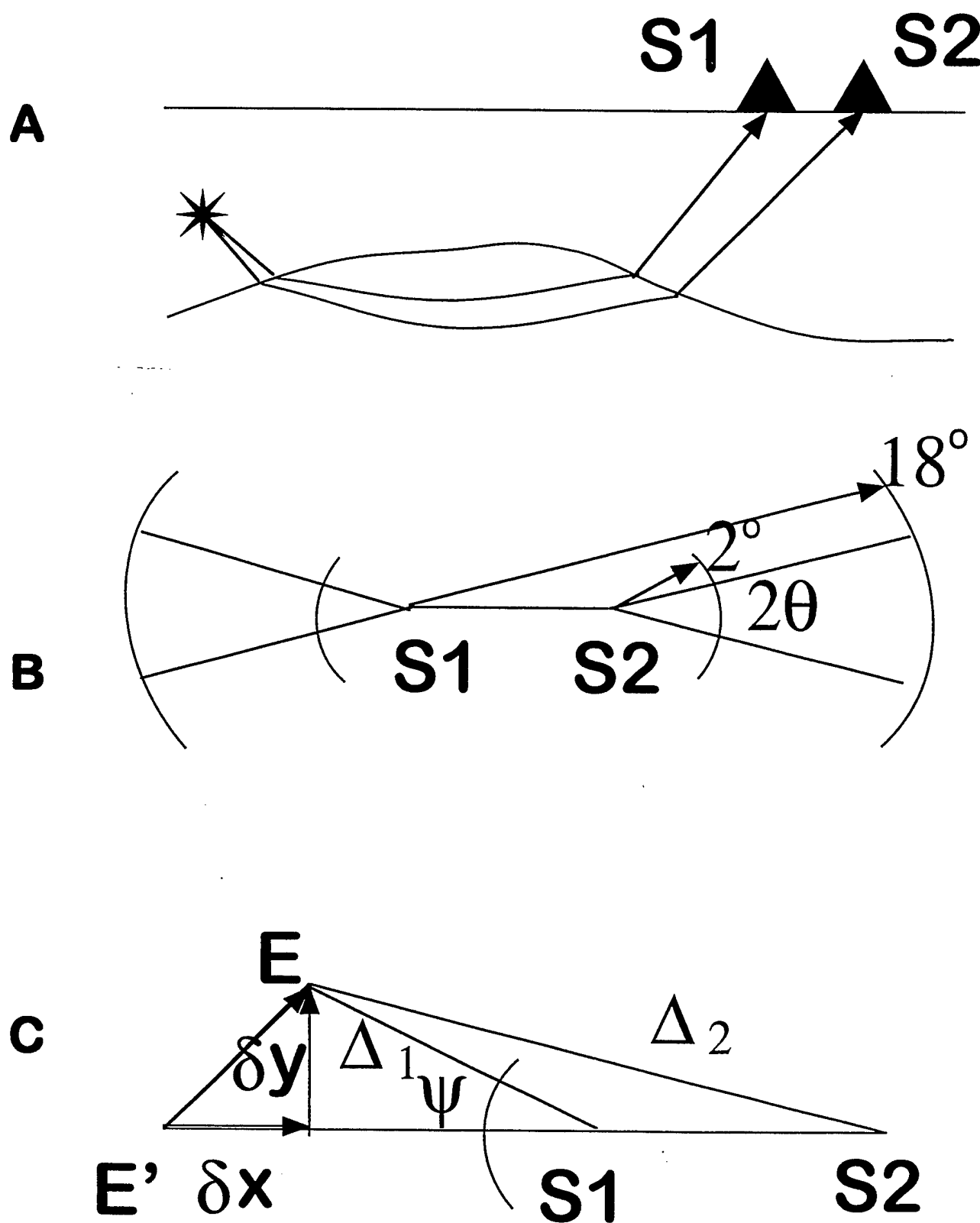


FIGURE 2

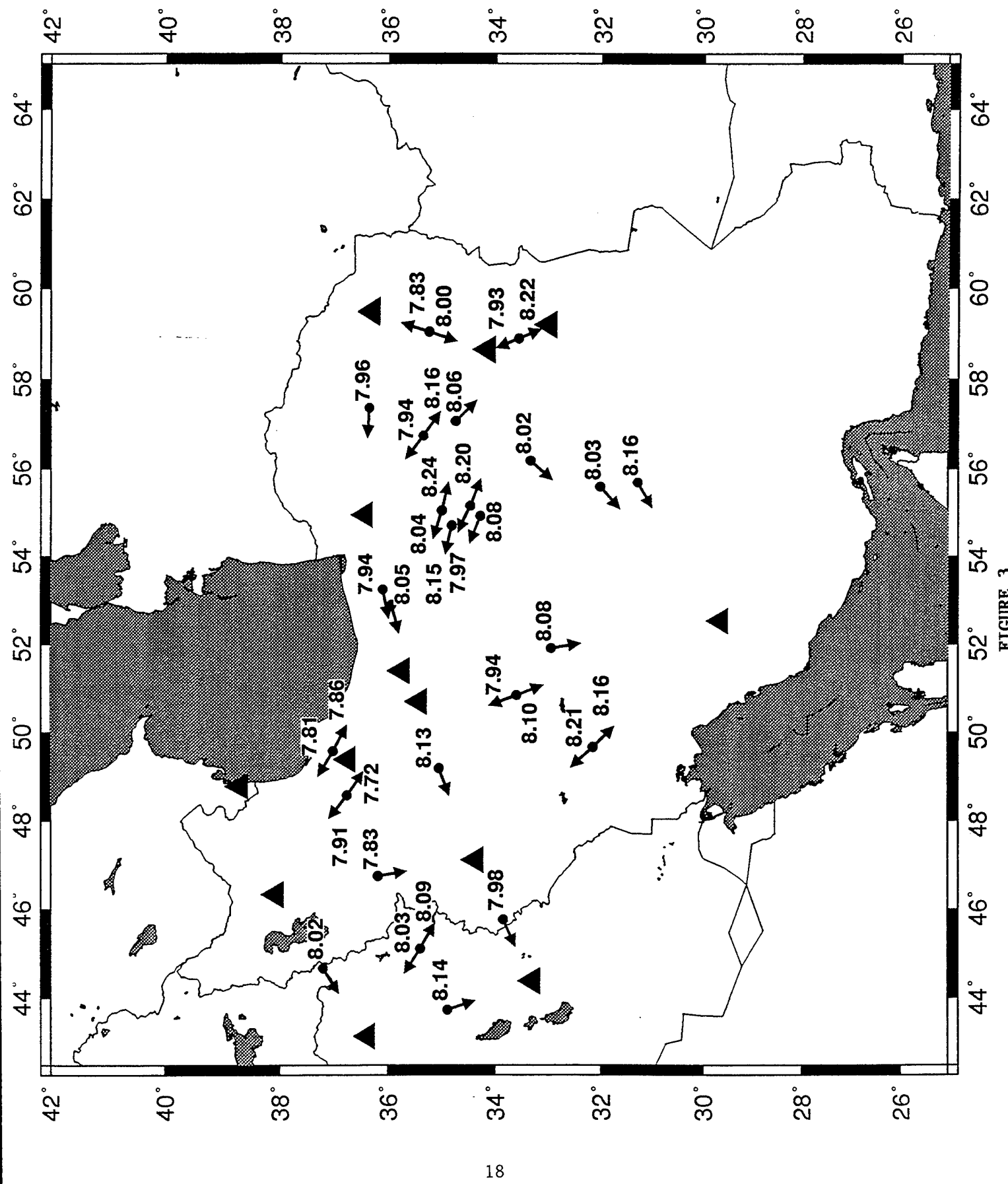


FIGURE 3

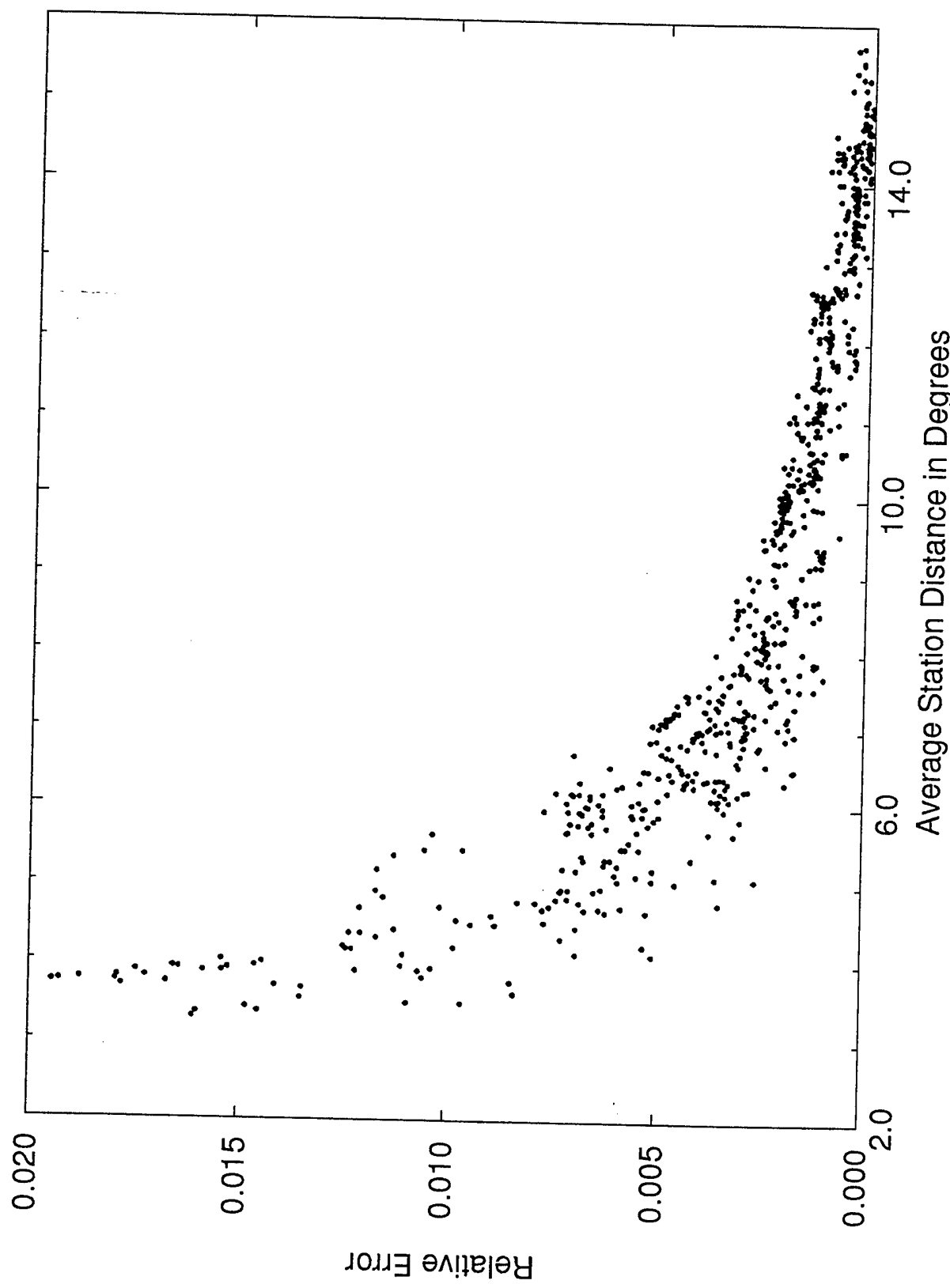


FIGURE 4a

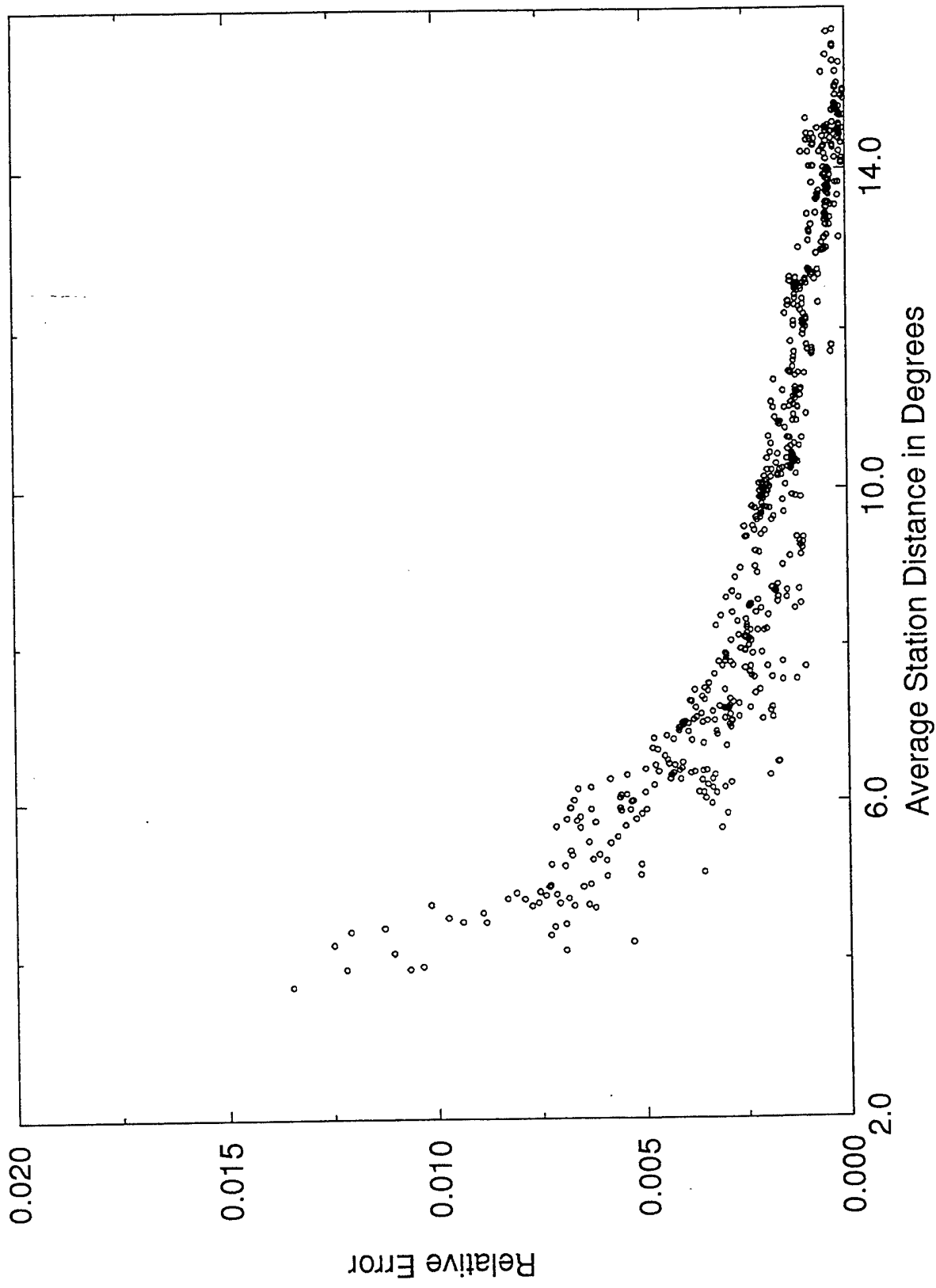
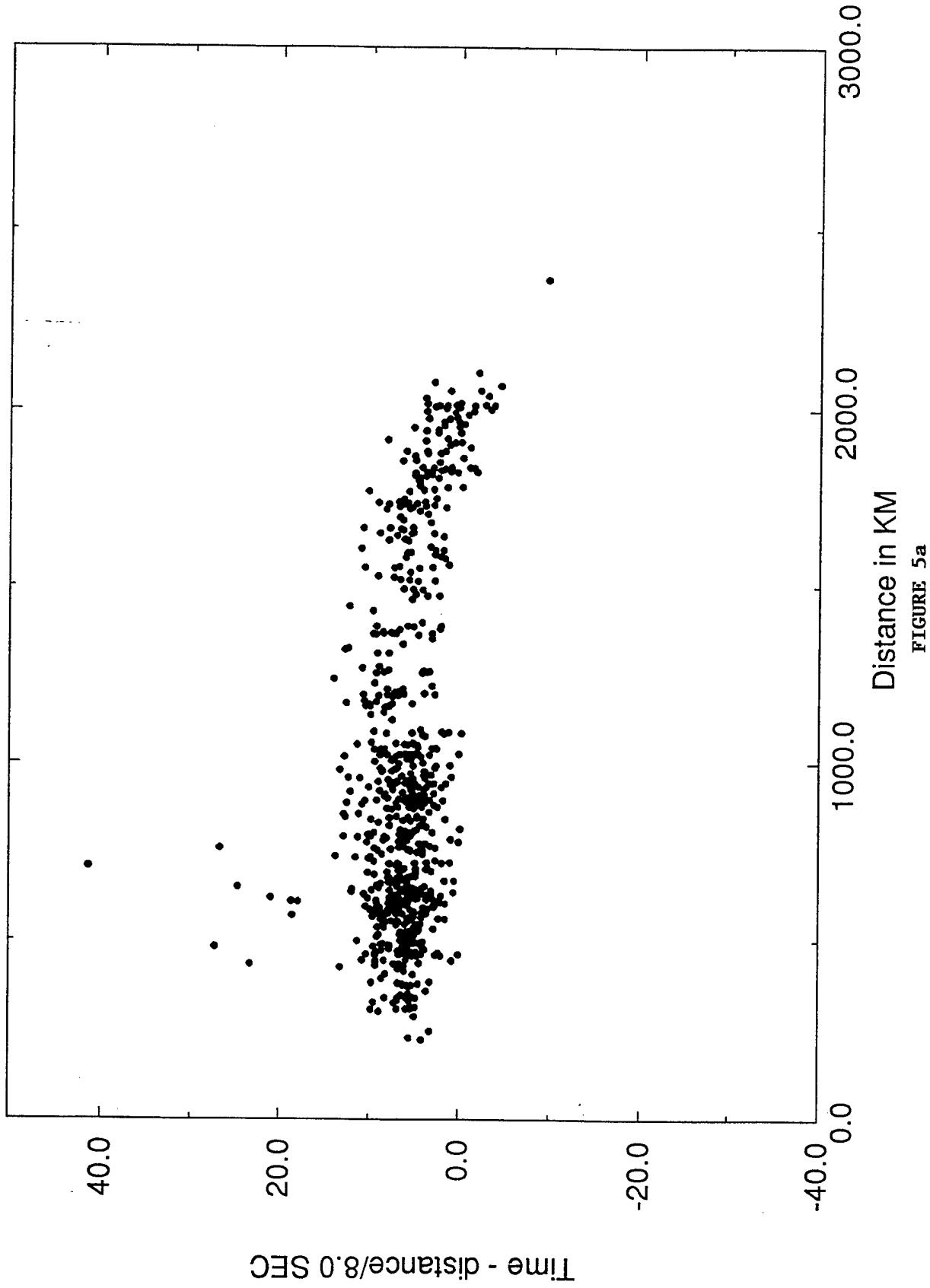


FIGURE 4b

TEH



SHI

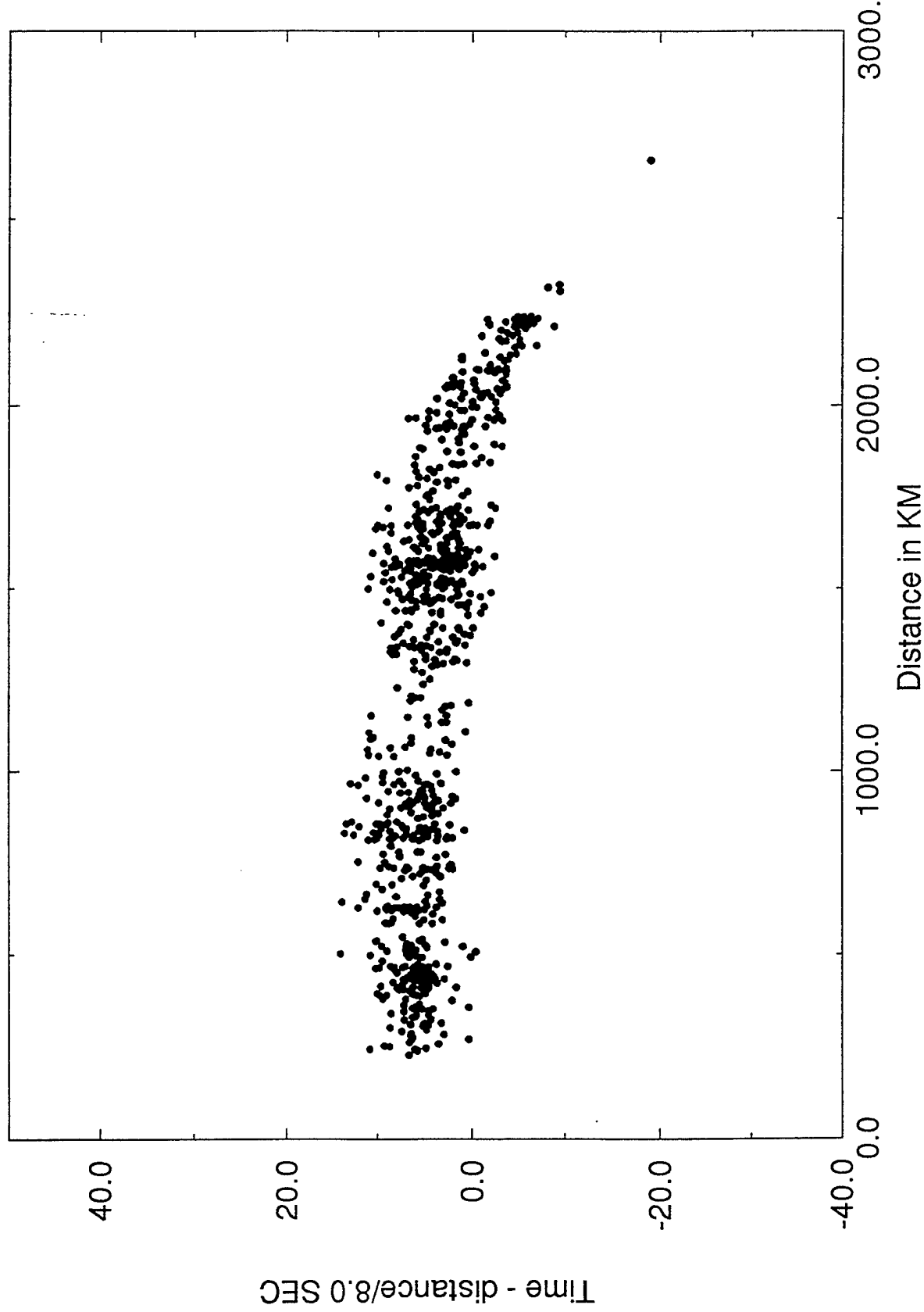


FIGURE 5b

TAB

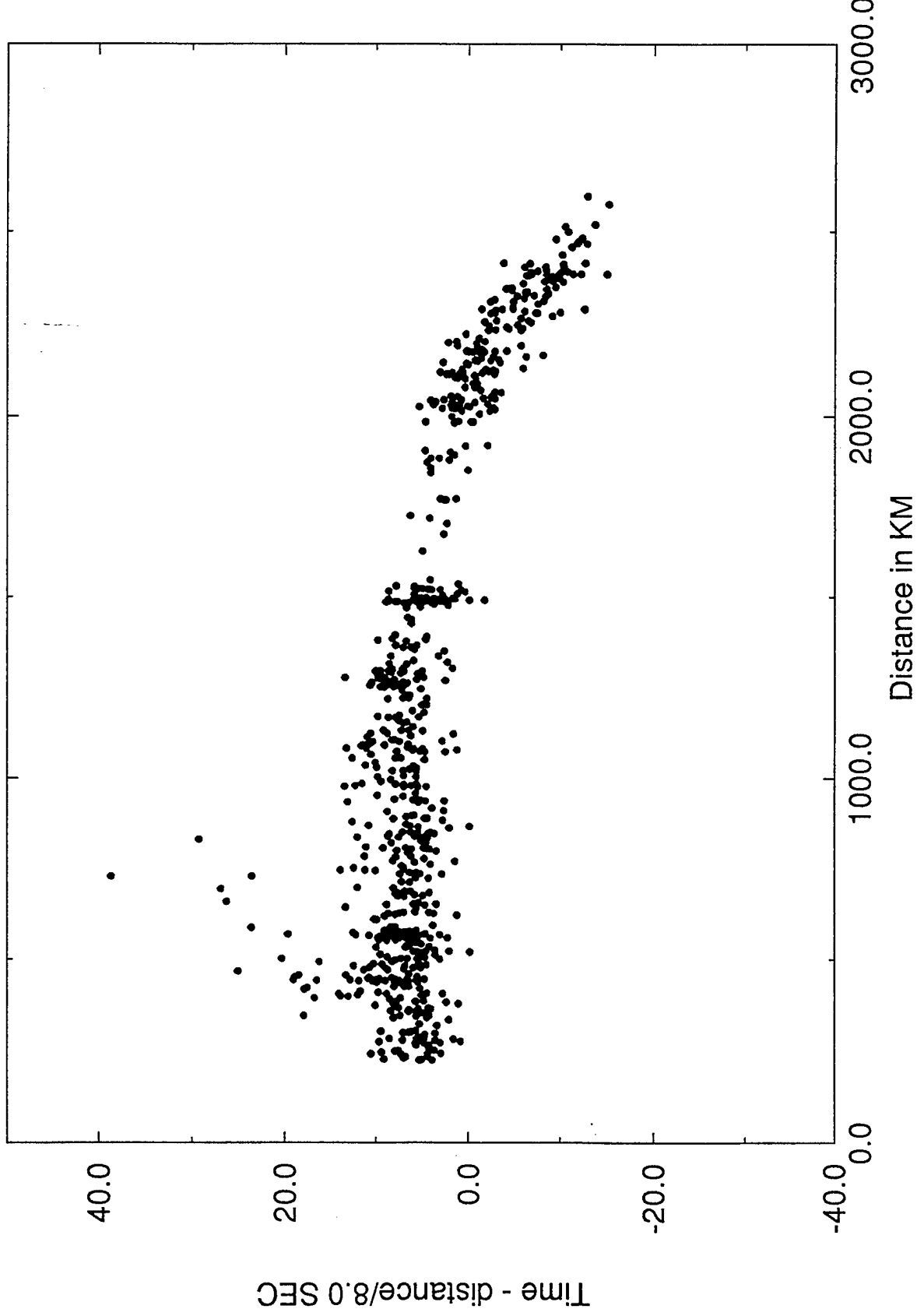
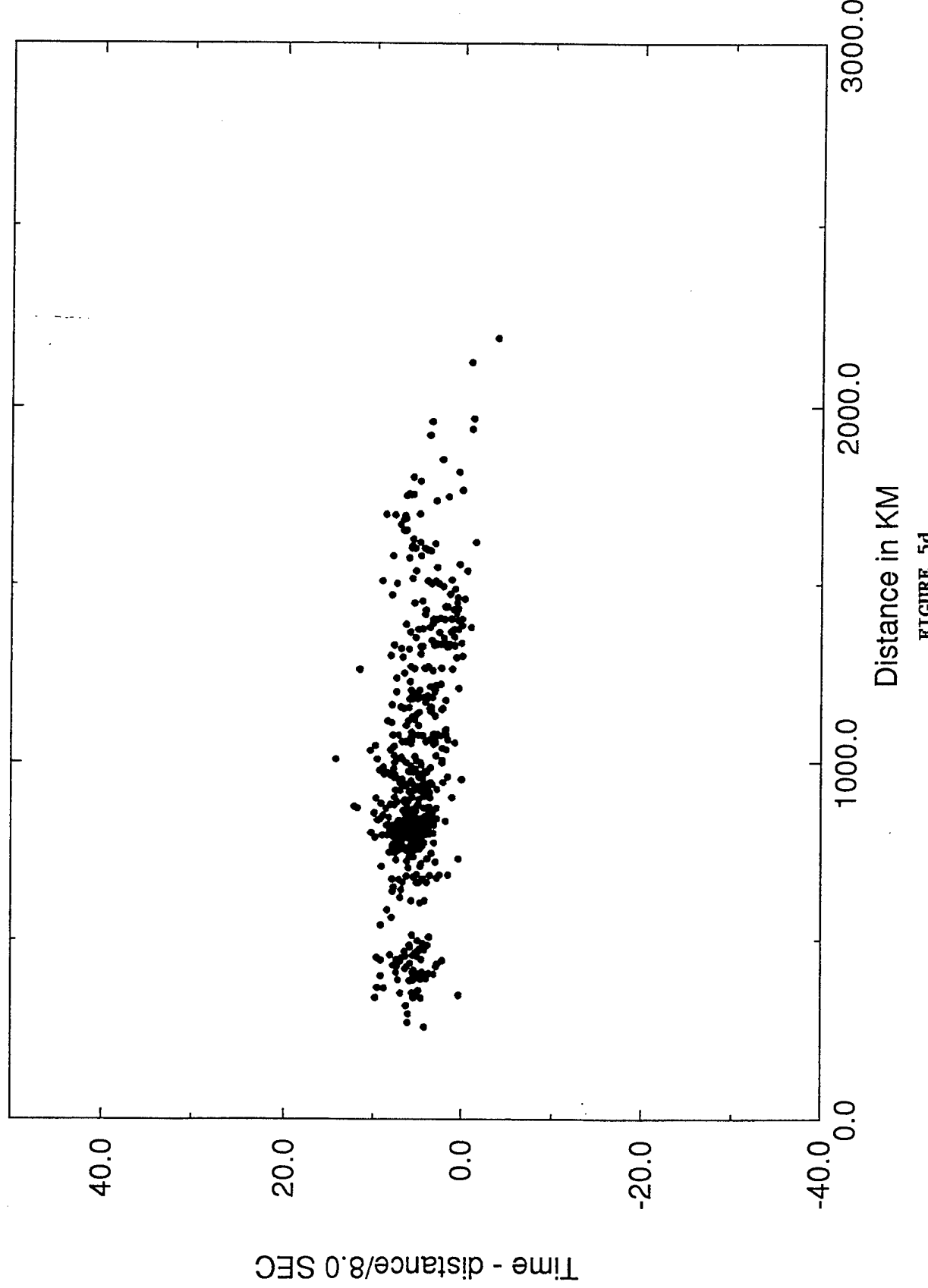
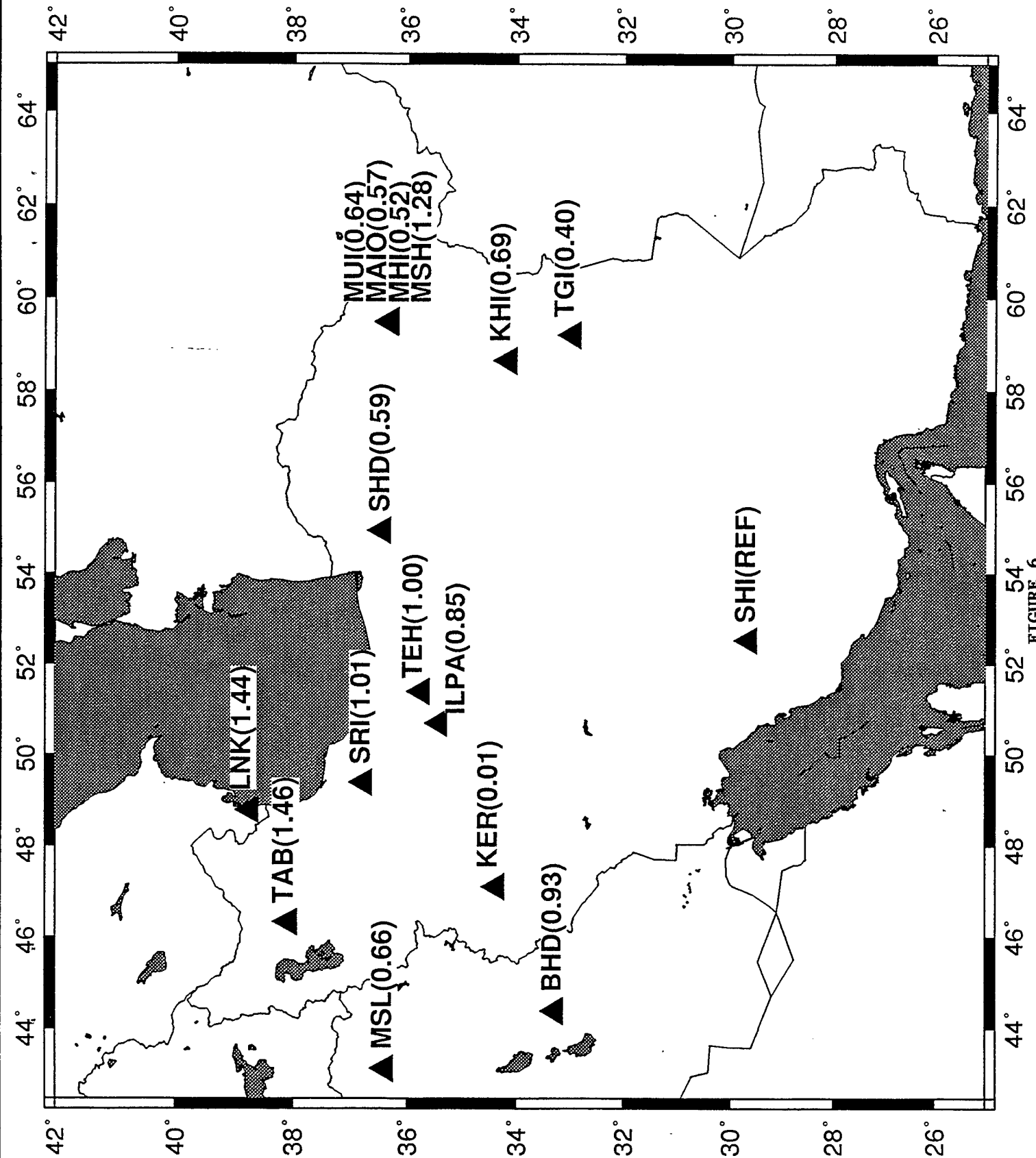


FIGURE 5c

KHI





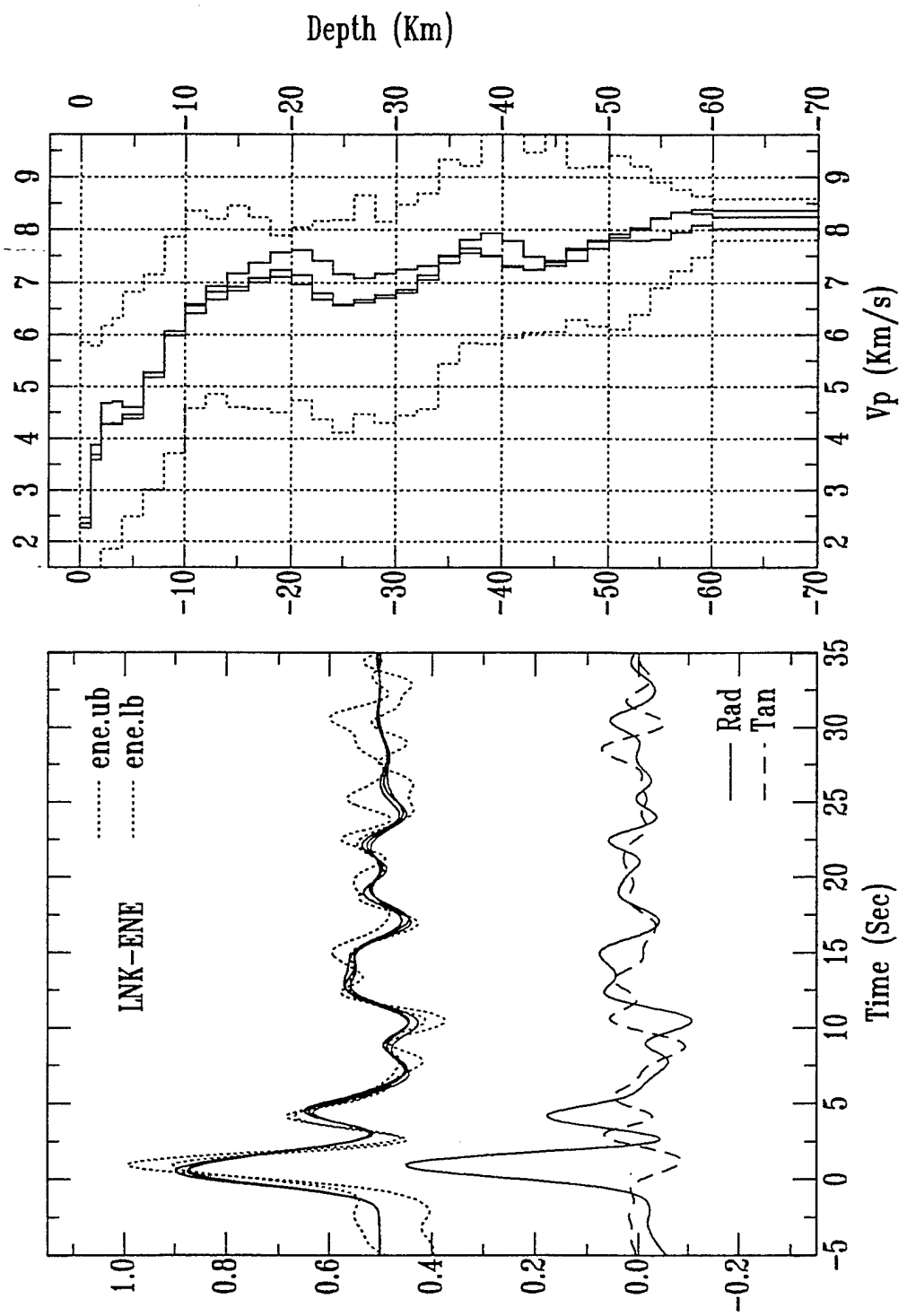


FIGURE 7a

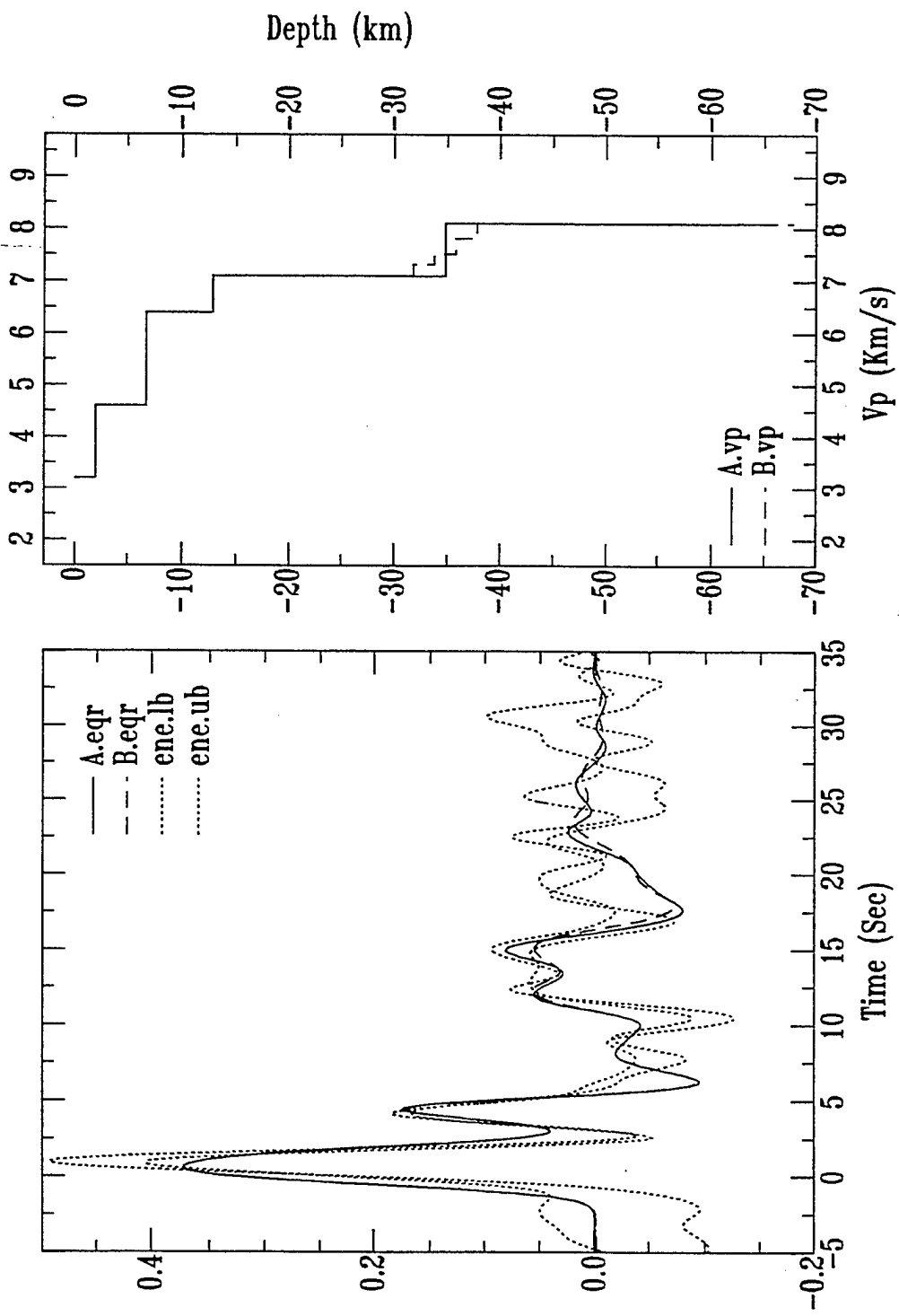


FIGURE 7b

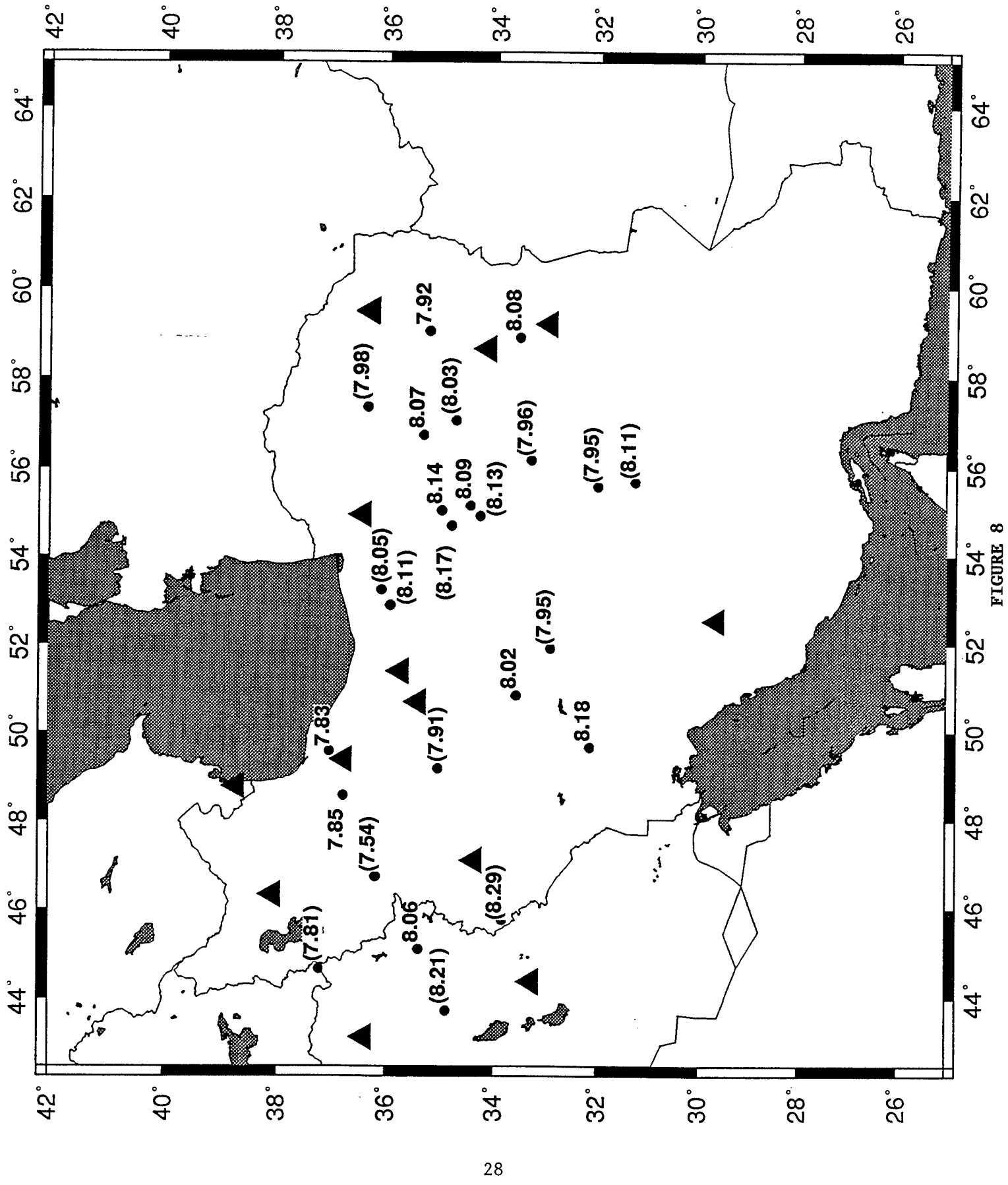


FIGURE 8

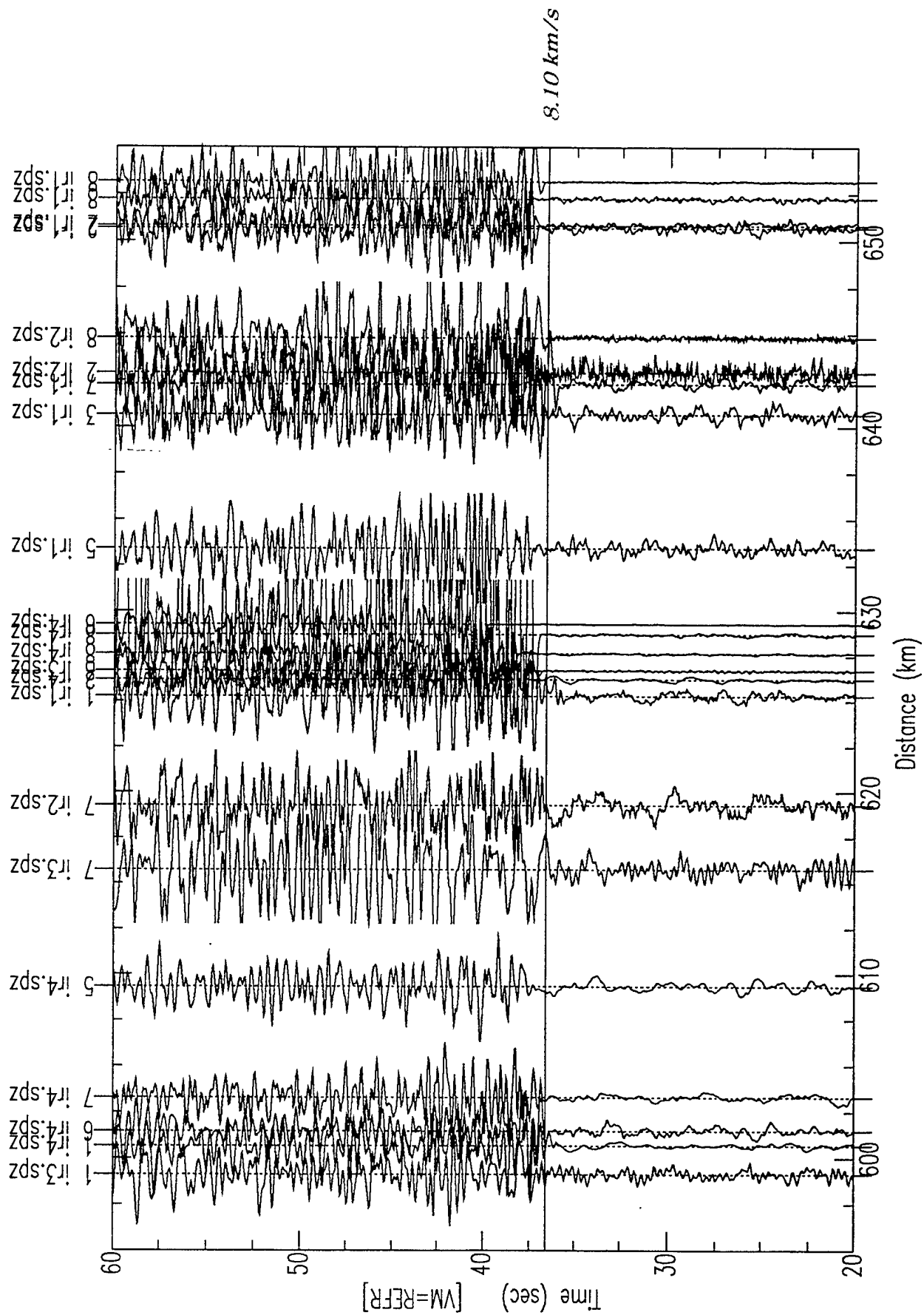


FIGURE 9

AVERAGE LITHOSPHERIC STRUCTURE OF SOUTHERN AFRICA

X. Qiu¹, K. Priestley, and D. McKenzie

Bullard Laboratories, University of Cambridge, Cambridge CB3 0EZ, UK

SUMMARY

We present a new 1-D earth model for the crust and upper mantle beneath the Archaean core of southern Africa. The crustal structure is constrained by published seismic refraction/reflection data and by modeling of teleseismic receiver function data. The mantle structure is constrained by travel time measurements for P_n and S_n waves, by waveform inversion of multi-mode surface waves, and by forward modeling of P_{nl} waveforms for regional earthquakes. The 42 km thick crust of southern Africa consists of four layers: a 2 km thick 5.05 km s^{-1} surface layer, a 5 km thick 6.08 km s^{-1} upper crust, a 20 km thick 6.30 km s^{-1} mid-crust, and a 15 km thick 6.73 km s^{-1} lower crust. Below the crust there is an 80 km thick upper mantle lid. V_P and V_S are 8.09 and 4.62 km s^{-1} , respectively, at the top of the lid and the compressional and shear velocity gradients through the lid are 0.0008 s^{-1} and 0.0013 s^{-1} , respectively. Below the lid there is a substantial shear wave LVZ with the shear wave velocity dropping from 4.72 km s^{-1} in the lower part of the lid to 4.32 km s^{-1} at 250 km depth. The shear wave LVZ is required to fit both the V_{S_n} measurements and the regional surface waveforms. Forward modeling of P_{nl} suggests that no upper mantle P-wave LVZ exists. There is an increase in the P-wave velocity gradient at 125 km depth to 0.0015 s^{-1} and a second increase at 250 km depth to 0.0035 s^{-1} . Velocities and densities in the seismic model of the lid closely agree with velocity and density estimates from geochemical analysis of garnet peridotite nodules from kimberlites on the Kaapvaal Craton, implying that the estimates from kimberlites are representative of a wider region of the Archaean core of southern Africa – not just the restricted region beneath where the kimberlites are found. A comparison of the southern African seismic model with seismic models for other shield regions where nodule data are not available shows that the nodule results may also be representative of the upper mantle in those regions.

Key words: crustal structure, precambrian, southern Africa, upper mantle

¹Present address: South China Sea Institute of Oceanology, Chinese Academia of Sciences, 164 West Xingang Road, Guangzhou 510301, P.R. China

1. INTRODUCTION

Knowledge of the geological and geophysical characteristics of the continental lithosphere and upper mantle is a prerequisite for unraveling continental evolution. In this study we focus on the seismic velocity and density structure of southern Africa, a region important in understanding continental evolution for two reasons. First, xenoliths from the large number of kimberlitic extrusions have provided unique data on the pressure and temperature environment in the upper mantle beneath southern Africa and estimates of upper mantle elastic properties predicted from the xenoliths can be tested with seismic measurements. Second, because of the vast amount of geophysical and geological data accumulated for southern Africa, this region has become the "Archetype" of Archaean continental evolution.

Here we analyze regional and teleseismic distance range earthquakes recorded on digital seismographs in southern Africa. We use teleseismic body waves in combination with existing seismic refraction and reflection results to constrain the crustal velocity structure, and we use waveform modeling of regional seismograms to constrain the velocity and density structure of the upper mantle. Our analysis results in twelve path-averaged models of earth structure for the region of the Archaean core. Since there are only minor differences between these models we have averaged them to form a 1-D earth model for this region. We then compare this 1-D earth model with: (a) velocity and density estimates derived from geochemical studies of the upper mantle xenoliths from South Africa, (b) previously derived upper mantle seismic velocity models for southern Africa, and (c) seismic velocity models derived for other shield regions. The goals of our study are to place better constraints on the velocity structure of the upper mantle beneath the Archaean core of southern Africa; to determine whether the predictions of *in situ* conditions based on the geochemical and petrological analysis of the xenoliths agree with seismic measurements in the same region; and to determine if the xenolith estimates are representative of the wider region of the Archaean core. In the main text, we briefly discuss the data and analytical method we follow, summarize the seismological results, and discuss their significance in light of the geochemical analysis of nodules from the kimberlites. The details of the seismological analysis and the geochemical calculations are given in the appendices.

2. GEOLOGICAL AND GEOPHYSICAL CHARACTERISTICS OF SOUTHERN AFRICA

Southern Africa consists of a well-defined Archaean core surrounded by Proterozoic mobile belts, which are in turn surrounded by late Proterozoic/early Phanerozoic mobile belts (Fig. 1). The Archaean core consisting of the Kaapvaal and Zimbabwe cratons and the Limpopo mobile belt has formed a stable unit for the past 2.3 Ga years (McElhinny & McWilliams, 1977). There have been no major tectonic events within southern Africa in at least the last 2 Ga years except in the Cape Fold belt (Clifford, 1970). The geologic and tectonic evolution of southern Africa is discussed in a number of past publications (e.g., Kroner, 1977; Tankard *et al.*, 1982; de Wit *et al.*, 1992).

Two observations suggest possible differences in the lithospheric structure within southern Africa. Although kimberlites are found over much of this region (Pasteris, 1983), diamond-bearing kimberlites have a more restricted distribution and occur almost totally within the cratons (Gurney, 1990). Since the diamond stability field is at higher pressure (i.e., greater depths) than that of the graphite found in many of the kimberlites, the distribution of diamond-bearing kimberlites suggests that the lithosphere of the central core of the cratons is thicker than the lithosphere of the surrounding regions. Some South African kimberlites are as old as 1.75 Ga years but the age of most southern African kimberlites clusters around 80–90 million years (Dawson, 1980). However, many of the diamonds are Archaean in age (Richardson *et al.*, 1984), implying

that the possible differences in lithospheric thickness within southern Africa suggested by the diamond-bearing kimberlite distribution may have existed since the early stages of continental lithospheric evolution. This in turn implies that these deeper portions of the lithosphere are less dense than the surrounding mantle since they have not delaminated as they have cooled.

Heat flow observations also suggest possible differences in the lithospheric structure within southern Africa. A large number of heat flow measurements have now been made in southern Africa. Ballard & Pollack (1987) point out that the heat flow in the interior of the Archaean core is typically about 40 mWm^{-2} but increases to about 60 mWm^{-2} at the craton boundaries with the surrounding Proterozoic and Pan-African mobile belts and as high as 70 mWm^{-2} within the mobile belts. They suggest two possible mechanisms to explain how this heat flow contrast might arise: a shallow geochemical mechanism resulting from a difference in crustal heat production within the Archaean core and surrounding mobile belts, and a deeper geodynamical mechanism arising from a thicker lithospheric root beneath the Archaean core compared to that beneath the mobile belts. They conclude that at least 50% and possibly 100% of the observed heat flow difference results from a thicker lithospheric root beneath the Archaean core which diverts mantle heat away from this region into the surrounding mobile belts. To achieve this they suggest that the cratonic root beneath southern Africa extends to a depth of 200 to 400 km. Such a thick, low density lithospheric root for the craton should have a distinctive seismic signature.

3. DETERMINATION OF THE VELOCITY AND DENSITY STRUCTURE OF THE SOUTHERN AFRICAN CRUST AND UPPER MANTLE

3.1 Data and Method of Analysis

We have used seismograms of teleseismic and regional earthquakes (Table 1 & 2) recorded at six digital seismographs (Table 3) in southern Africa to determine the crust and upper mantle structure of this region. The locations of the regional earthquakes and seismograph stations are shown in Figure 2.

We employ a variety of seismological techniques to determine models for the crust and upper mantle velocity structure. We determine the gross features of the crustal structure beneath the seismograph stations using teleseismic receiver function modeling (Owens *et al.* 1984). The direct teleseismic P-wave interacts with velocity interfaces and gradients in the crust beneath the seismograph to produce a seismogram consisting of the direct P-wave plus P-wave reverberations and P-to-S converted phases plus their reverberations. Source effects can be largely removed from the radial component by deconvolving from it the vertical component seismogram (Langston, 1979). For laterally homogeneous structures the resulting radial component seismogram, called the receiver function, primarily contains P-to-S conversions and their reverberations, and the resulting tangential component is zero. Thus the ratio of the tangential to radial amplitude gives an indication of the degree of scattered energy due to lateral variation in earth structure in the vicinity of the seismograph. We have modeled the receiver functions to verify that crustal thickness estimates from this technique do not differ significantly from crustal thickness estimates from nearby seismic refraction data where they exist and to constrain crustal thickness in the vicinity of the seismograph stations where nearby refraction results do not exist.

We determine the path-averaged shear wave velocity structure for the crust and upper mantle by inverting multi-mode surface waveforms for regional earthquakes using the technique of Gomberg & Masters (1988). The seismogram is represented as a sum of locked-mode traveling waves (surface waves) in a plane-layered structure. The earth-flattening transformations of Biswas & Knopoff (1970) and Biswas (1972) are used for the Love and Rayleigh waves, respectively, and physical dispersion is accounted for using the correction of Liu *et al.* (1976). The difference between an observed and synthetic seismogram can be directly related to perturbations

in the model velocity and density structure through the partial derivatives of the phase velocity with respect to the model parameters. A new model is determined and the process repeated until a satisfactory variance reduction is achieved. This procedure is superior to inverting surface wave dispersion curves for earth structure because fundamental mode surface waves, whose dispersion curves can readily be obtained, on their own are not very sensitive to the details of the upper mantle velocity structure. Dispersion curves of higher modes are more sensitive to upper mantle structure but are difficult to determine because of the complex interference of the waves arriving between S and the fundamental mode wavetrain. By directly modeling the waveforms this interference is taken into account and there is no need to determine spectral properties of individual modes. We have inverted the data for each path separately but we have simultaneously inverted the seismograms from the vertical, radial, and transverse components.

To constrain the P-wave velocity gradient in the upper mantle we forward model P_{nl} waveforms for the regional earthquakes. P_{nl} is a combination of two phases: the P_n phase resulting from P-wave energy turning beneath the Moho and the following P_l mode trapped in the crustal wave guide (Helmberger & Engen, 1980). P_l is the near monochromatic long-period wavetrain often seen in the epicentral distance range 5–20° following the P_n phase from crustal earthquakes (e.g. Oliver & Major, 1960; Oliver, 1964). P_l propagates in the crustal waveguide as a partially trapped P-Sv wave whose phase velocity is bracketed by the compressional and shear wave velocity of the upper mantle ($V_s < c_{P_l} < V_p$). The P-wave is therefore post-critical and energy leaks to the mantle as Sv, resulting in a decay of P_l with range. The P_l waveform is primarily controlled by the P-wave travel time through the crust (Shaw & Orcutt, 1984) resulting in a particular interference pattern for the trapped energy and a characteristic period for P_l . Because P_l is only weakly affected by the upper mantle velocity structure (Shaw & Orcutt, 1984), it forms a good reference for comparing the amplitude of P_n or direct P at regional distance ranges (Clouser & Langston, 1990), which is very sensitive to the compressional velocity gradient and attenuation in the mantle lid (Hill, 1971; 1973). We forward model the observed P_{nl} waveforms using reflectivity synthetics (Fuchs & Müller, 1971) to provide a constraint on the upper mantle compressional velocity gradients.

3.2 Velocity Structure of the Southern African Crust

This study is primarily concerned with the average velocity structure of the upper mantle and not with the details of the velocity structure of the crust. However, a reasonably accurate knowledge of crustal structure is important to our study because if large scale lateral variations in crustal structure exist, they may, if not properly accounted for, map into the structure of the upper mantle. A number of seismic refraction/reflection studies have been conducted in southern Africa over the past 50 years. Many of these studies have used mine tremors as the seismic energy source. These have the advantage that they are a rich source of shear wave energy but have the disadvantage that their origin times and locations are poorly known compared to those of explosions. Both the quality of these data and the methods of interpretation have varied between these studies, so it is not easy to directly compare results for the details of the crustal features. However, the crustal thickness determined in these studies can be compared. All of the cratonic seismic profiles are for the Kaapvaal Craton. Durrheim & Green (1992) analyzed refraction data for two seismic profiles in the central Kaapvaal Craton by matching observed and synthetic seismograms, and their study provides the best constraints on the velocity gradients and layering in the Kaapvaal Craton crust. The crust in this region has the following features: a shallow crust (<5 km depth) consisting of a stratified section varying in compressional velocity from 3.5 to 6.8 km s^{-1} , a relatively uniform upper crust (5–12 km depth) with velocities ranging from 6.0 to 6.2 km s^{-1} , a transition from upper to lower crust marked by a change in velocity gradient at 12 to 14 km depth; a uniform lower crust with velocities varying from about 6.4 km s^{-1} at 14 km

depth to about 6.7 km s^{-1} at about 32 km depth, and a gradational crust/mantle transition near 35 km depth with velocities increasing from less than 7 km s^{-1} to greater than 8 km s^{-1} over a 2 to 3 km depth range. The crustal shear wave velocity from traveltimes studies varies from 3.66 km s^{-1} (Gane *et al.*, 1956) to 4.15 km s^{-1} (Hales & Sacks, 1959). Durrheim & Green (1992) find the average shear wave velocity of the crust to be 3.8 km s^{-1} . The P_n velocity beneath the Kaapvaal Craton is $8.0 - 8.2 \text{ km s}^{-1}$ (Willmore *et al.*, 1952; Hales & Sacks, 1959; Durrheim & Green, 1992). Willmore *et al.* (1952) observe S_n to have a velocity of 4.83 km s^{-1} , significantly higher than the $4.70 - 4.73 \text{ km s}^{-1}$ observed by Gane *et al.* (1956) and Durrheim & Green (1992).

To determine the crustal structure in the immediate vicinity of the four broadband seismograph stations, we have analyzed teleseismic receiver functions. This is particularly important in the case of LSZ (Fig. 2) where no nearby refraction data exist and the crustal structure is otherwise unknown. Appendix A summarizes the receiver function analysis. In analyzing the receiver function data we are primarily concerned with determining the crustal thickness and average crustal velocity. Since the receiver functions consist of few events we have concentrated on fitting the early arrivals and have not emphasized fitting later weak arrivals.

Figure 3 shows the stacked radial and transverse receiver functions for BOSA, along with the $\pm 1\sigma$ bounds determined from the variance of the stack. These bounds provide a useful measure of the coherence of the arrivals comprising the stack. The radial receiver function shows a large amplitude arrival 4 seconds after the main direct P arrival. There are two smaller amplitude arrivals; a positive arrival ~ 14 seconds after direct P and a negative arrival ~ 18 seconds after direct P. The amplitudes of these arrivals on the radial are large compared with the amplitudes of the tangential at the same time. If we interpret the first of these later arrivals as a P-to-S conversion at the Moho (Ps), assume an average crustal P-wave velocity of 6.4 km s^{-1} and a Poisson's ratio of 0.25, the timing of this arrival suggests a 35 km thick crust beneath BOSA.

We have inverted the BOSA receiver function data in Figure 3 and similar data for LBTB, LSZ, and SUR using the linearized inversion procedure of Ammon *et al.* (1990). The receiver function result for BOSA is shown in the inset in Figure 3 and the results for the other three sites are shown in Figures A2–5. The receiver function crustal model for BOSA has a steep gradient in the shallow crust with the shear wave velocity increasing from 2.35 km s^{-1} at the surface to 3.67 km s^{-1} at 2.6 km depth. The crystalline crust is composed of a 26 km thick section with an average velocity of 3.67 km s^{-1} . There is a steep gradient between 29 and 35 km depth with the Moho transition between velocities of 3.98 and 4.75 km s^{-1} occurring from 35 to 38 km depth. The synthetic receiver function fits the general features of the observation but not the details. Much better fits were achieved than that shown in Figure 3 by allowing more complex earth models. However, since the receiver functions were composed of few events and because our purpose was to confirm the gross crustal features and not to examine the details of the crustal velocity structure, we have chosen only to model the main features of the receiver functions.

Four seismic refraction studies (Willmore *et al.*, 1952; Gane *et al.*, 1956; Hales & Sacks, 1959; Durrheim & Green, 1992) show the crust is 36 ± 1 km thick over a wide region of the central part of the Kaapvaal Craton (Fig. 4). The teleseismic receiver function result for BOSA in the SW part of the craton shows the crust is 35 km thick in this region also. The receiver function result for LBTB (Fig. A2) in the NW part of the craton shows the crust in this region is 44 km thick, significantly thicker than to the south. This difference is clearly seen from comparing the Ps-P time differences for the BOSA and LBTB receiver functions: this time difference is nearly one second greater for LBTB (Fig. A2) than for BOSA (Fig. 3). Wright & Hall (1990) suggest that their seismic reflection data from the Kalahari of western Botswana to the NW of LBTB show the crust thickening to the SE approaching the Kaapvaal Craton. They observe a 14 sec two-way travel time from a reflector they identify as the Moho. If the average crustal P-wave velocity is 6.4 km s^{-1} in this region as it is to the south, this corresponds to a Moho at about 45 km depth. Therefore it may be that beneath much of the Kaapvaal Craton the crust is 36 ± 1

km thick but is significantly thicker in the NW part of the craton.

The crustal structure of the Zimbabwe Craton and the Limpopo mobile belt is poorly known. The little seismic refraction data that exist suggest that the crust beneath the Zimbabwe Craton is about 40 km thick and that the crust beneath the Limpopo mobile belt is 34–36 km thick (Stuart & Zengeni, 1987; Durrheim *et al.*, 1992). These values agree with the crustal thickness estimates from gravity and electrical studies (de Beer & Stettler, 1992; Gwavava *et al.*, 1992). Beneath the crust of the Limpopo there exists a 5–10 km thick, 8.1 km s^{-1} layer overlying a 14 km thick layer where V_p drops to 7.6 km s^{-1} (Durrheim *et al.*, 1992); beneath this there is a positive velocity gradient with velocities reaching 8.5 km s^{-1} at a depth of 110 km.

Seismic refraction/reflection studies show that the crust beneath the Proterozoic/early Phanerozoic mobile belts is thicker (42–47 km) than beneath the the Archaean core (Baier *et al.*, 1983; Green & Durrheim, 1990; Wright & Hall, 1990). In addition, there is a suggestion (Durrheim & Mooney, 1991) that the lower crust beneath the mobile belts contains a thick, high velocity ($V_p > 7.0 \text{ km s}^{-1}$) section not observed in the lower crust of the cratons. However, most of the analysis of seismic refraction data in southern Africa predate the use of synthetic seismogram modeling and hence this proposed difference in the lower crust between the mobile belts and the cratons requires substantiation. SUR is near the boundary of the Namaqua Province and the Cape Fold Belt. Inversion of two receiver function data (Fig. A3–4) shows that the crust beneath this site is 52 ± 1 km thick. Green & Durrheim (1990) find the crustal thickness from seismic refraction measurements in the Namaqua metamorphic complex 300 km NW of SUR is significantly thinner (42 km). LSZ is located north of the Zimbabwe Craton in the Irumide mobile belt. We have inverted the single event receiver function from LSZ (Fig. A5) and the result suggests a crustal thickness of about 42 km. Since the receiver function consists of only a single event, we have less confidence in this result than in the other receiver function results; however, this is the only crustal thickness estimate available for this region.

Figure 4 summarizes the data for crustal thickness in southern Africa. From these data we form an average 1-D velocity model for the southern African crust to use as a starting model for the regional waveform inversion. This crustal model is 41.4 km thick and has the following main features: a 1.4 km thick sedimentary layer with P-wave velocity 4.2 km s^{-1} , a 5 km thick upper crust with P-wave velocity 6.2 km s^{-1} , a 20 km thick mid-crust with P-wave velocity 6.4 km s^{-1} , and a 15 km thick lower crust with P-wave velocity 6.8 km s^{-1} . Poisson's ratio is assumed to be 0.25 throughout the crust.

3.3 Velocity Structure of the Southern African Mantle

3.3.1 Body-wave constraints

Knowledge of the compressional and shear wave speeds directly beneath the Moho (V_{P_n} and V_{S_n}) provide important constraints in the inversion of the regional surface waveforms. More precise knowledge of V_{S_n} beneath the Archaean core is particularly important in our study since surface wave propagation is primarily controlled by the shear wave structure. Both the fact that S_n travels with a constant surface velocity near that of the upper mantle shear speed and that S_n has a substantial high frequency component suggest that it propagates as S-wave energy trapped in the upper mantle lid, and is thus diagnostic of the upper mantle shear wave speed. Independent knowledge of the upper mantle shear wave speed is important since it can aid in distinguishing between velocity models with low average upper mantle shear wave velocities but no LVZ and velocity models containing a higher velocity upper mantle lid above a shear wave LVZ, both of which could agree with the surface wave observations.

V_{P_n} measurements from seismic refraction profiles in several areas of southern Africa (Fig. 4) show V_{P_n} is $8.1 \pm 0.1 \text{ km s}^{-1}$. The measured S_n velocity observed along three of the refraction

profiles in the Kaapvaal Craton (Willmore *et al.*, 1952; Gane *et al.*, 1956; Durrheim & Green, 1992) varies from 4.70 to 4.83 km s⁻¹. Gumper & Pomeroy (1970) measured V_{P_n} 8.06 km s⁻¹ and V_{S_n} 4.55–4.72 km s⁻¹ using earthquakes from over a wider region of southern and eastern Africa. However, several of the paths they examined traversed the East African Rift. Molnar & Oliver (1969) and Gumper & Pomeroy (1970) note that S_n is only observed for paths in southern Africa and for paths south of 10°S crossing the rift. The observed values of V_{S_n} (Gumper & Pomeroy, 1970) over this wider region of southern Africa span the range observed for shields (e.g. Brune & Dorman, 1963; The Canadian Shield) to regions of active continental rifting (e.g. Priestley & Brune 1978; The Basin and Range).

To improve the constraint on V_{S_n} in southern Africa we constructed a composite record section of seismograms from southern African events recorded in the distance range 300–2,000 km. The propagation paths for these events are primarily confined to the stable regions of southern Africa (Fig. 2 & Table 1) although some of the events occur in the southernmost part of the rift. These seismograms (Fig. 5) show a clear S_n phase with a travel time curve given by $T=12.0 + \Delta/4.64$. $V_{S_n} \sim 4.64$ km s⁻¹ falls in the middle of the Gumper & Pomeroy (1970) V_{S_n} range but is low compared with V_{S_n} observed for shorter range refraction recordings within the Kaapvaal Craton (Willmore *et al.*, 1952; Gane *et al.*, 1956; Durrheim & Green, 1992) and for most shields (Huestis *et al.*, 1973). In the surface wave inversion we use $V_S = 4.64$ km s⁻¹ as a constraint on the S-wave velocity immediately below the Moho. In modeling events with most of their path length within the Archaean core or mobile belts of southern Africa we require $V_{S_n} \geq 4.64$ km s⁻¹ but relaxed this requirement for events with larger fractions of their path length in the southern portions of the East African Rift.

3.3.2 Modeling of Regional Surface Waves

We determine the mantle shear velocity structure using the differential seismogram technique of Gomberg & Masters (1988). We have inverted twelve, three-component long period seismograms from eight regional earthquakes (< 30°) in southern Africa (Fig. 2 & Table 1) recorded at the digital stations BOSA, LBTB, LSZ, SLR, and SUR (Table 3). This has resulted in twelve path-averaged earth models. The propagation paths are primarily confined to the cratons and portions of the surrounding mobile belts; however, some paths also sample small portions of the east African rift. Appendix B describes in more detail the analysis and summarizes the inversion of the regional surface waveforms.

The seismogram of the July 18, 1986 (Event 2, Table 1 & 2) earthquake recorded at SLR is typical of the data we have inverted for earth structure and we use it as an example of our analysis procedure. This event occurred on the northern boundary of the Zimbabwe Craton; thus, the propagation path to SLR was confined almost entirely to the Archaean core. The event is almost due north of SLR and the seismograms (Fig. 6) are therefore close to being naturally rotated (N–S radial; E–W tangential). The short-period P-wave consists of an impulsive P_n (group velocity 7.80 km s⁻¹) and no significant P_g phase. This observation is typical of short-period P-wave propagation in stable regions (Evernden, 1967; Langston, 1982). The S_n phase (group velocity 4.46 km s⁻¹) is followed by a large amplitude L_g phase (beginning group velocity ~ 3.67 km s⁻¹). The long-period seismograms are relatively simple. The first arrival on the vertical and N–S (radial) primarily consists of the P_{nl} wave. The surface waves begin with the higher Rayleigh and Love modes near the predicted S-wave arrival time (~ 235 sec) and culminate with the fundamental Love mode Airy phase at about 300 seconds and fundamental Rayleigh mode Airy phase at about 335 seconds.

The starting earth model for the waveform inversion consists of the average crustal model discussed in section 3.2 and the upper mantle S-wave model from Bloch *et al.* (1969) (Fig. 7c). The upper mantle P-wave velocity was related to the S-wave velocity assuming a Poisson's

ratio of 0.25 and the upper mantle density was related to the P-wave velocity assuming $\rho = 0.77 + 0.32V_p$. Figure 7a compares the long-period seismograms with synthetic seismograms (fundamental and eight higher modes) computed for Event 2 at SLR using the ISC location (Table 1) and the CMT source parameters (Table 2) and the starting earth model. The phase of the synthetic higher mode matches the observed higher mode although the synthetic amplitude is larger than the observed amplitude. The long period synthetic fundamental mode phase and amplitude are in reasonable agreement with the observed waveform but the fundamental mode Airy phase is in poor agreement. Before inverting the surface waveforms for a new earth model we first checked to verify that the observed misfit could not simply be explained by reasonable errors in the hypocentral location or mechanism for the event. The ISC location accuracy in southern Africa is uncertain but a comparison of the teleseismic locations of the ISC with regional locations of the South African Geological Survey for large rock bursts suggest that the ISC location errors do not greatly exceed ± 10 km for the three hypocentral coordinates. Altering the hypocenter by these amounts and the source parameters (strike, slip, dip) $\pm 10^\circ$ from the CMT values did not produce a better fit between the observed and synthetic seismograms computed for the starting model.

The three-component long-period seismograms were inverted for the path-average earth model using the waveform fitting approach of Gomberg & Masters (1988). The new earth model is shown in Figure 7c. The mantle consists of a 76 km thick upper mantle lid with $V_{S_n} = 4.64 \text{ km s}^{-1}$ directly beneath the Moho. The two layer lid corresponds to a shear wave velocity gradient of about 0.0011 s^{-1} . Below the lid is a substantial upper mantle LVZ. At the bottom of the lid V_s equals 4.72 km s^{-1} , but drops to 4.10 km s^{-1} at 200–330 km depth. The synthetic seismograms computed for the inversion earth model are shown in Figure 7b. We found that the fit was improved by reducing the hypocentral depth of the earthquake from 17 to 12 km. The phase of the higher mode wave train arriving between about 240 and 300 sec is well fit by the synthetic seismogram although the synthetic amplitude is still somewhat high. The low frequency portion of the fundamental mode wavetrain is well fit and the phase of the fundamental mode Airy phase is matched; however, the amplitude of the main peak on the vertical component is underestimated by about 40%.

In Appendix B we discuss a series of tests we have conducted to assess the effects of errors in our assumptions and in the data on the inversion earth model. We assume that the hypocenter may be in error by ± 10 km in distance and depth and that the source mechanism may be in error by $\pm 10^\circ$ in strike, dip, and slip. We then reinvert the surface waveforms to find the effects of these values on the earth structure. The results of these tests are shown as the bounds on the velocities and density in Figure 7c. We have also conducted tests to evaluate the resolution of the data in controlling the thickness of the upper mantle lid and the existence of a LVZ. While the details of the LVZ velocity structure varied, we were unable to find shear wave upper mantle models which satisfied the V_{S_n} data from Figure 5 and which did not contain a S-wave LVZ. We therefore conclude that at least an upper mantle shear wave LVZ exists beneath the Archaean core of southern Africa.

3.3.3 Modeling of P_{nl} Waveforms

Surface wave observations do not constrain upper mantle compressional wave velocity structure. We determine the compressional velocity structure of the upper mantle by forward modeling P_{nl} waveforms from the seismograms of the same eight regional earthquakes used in the surface waveform inversion. We follow an approach similar to Clouser & Langston (1990). Appendix B also summarizes our forward modeling of the P_{nl} waveform data.

Figure 8 is an enlargement of the P-wave for Event 2 recorded at SLR. To gain insight into the composition of the P-wave we first smoothed the coarse “blocky” inversion model by

increasing the number of layers and changing some of the velocity steps in the coarse model into gradients. We then computed generalized ray synthetic seismograms for this smoothed surface wave inversion model for the separate arrivals making up the Event 2 P-wave. Based on these synthetics the first arrival is the direct P-wave and the second arrival is composed of upper mantle turning rays from the S-to-P conversion at the Moho beneath the source and from the depth phases pP and sP. Comparing the individual amplitudes of these phases shows that sP is primarily responsible for the observed waveform for this event. Figure 9a shows reflectivity synthetics computed for the smoothed surface wave inversion model compared with the Event 2 long-period SLR seismograms. Whereas the overall fit of the P_{nl} waveform is good, the amplitude of the synthetic first arrival is small compared to that of the observed first arrival suggesting that there is insufficient energy present in the synthetic mantle turning wave at this range.

We replaced the mantle lid P-wave velocity structure derived from the surface wave modeling with the mantle lid P-wave structure SACM06c found by Clouser & Langston (1990) and recomputed the reflectivity synthetic seismograms. This produces a much better match to the observed first arrival. We then used a trial-and-error forward modeling approach of matching the synthetic waveform to the observed waveforms by adjusting the upper mantle P-wave velocity gradient. The Event 2-SLR path is 1038 km long, similar to the most distant event studied by Clouser & Langston (1990). The match between the synthetic and observed seismograms for this event imply that there is a positive compressional velocity gradient in the upper mantle lid beneath the Archaean core, and that the base of the "P-wave lid" is at least 50 km deeper than the base of the "S-wave lid". However in modeling events at greater distance ranges (see Appendix B) we found that the top of the "P-wave" LVZ must be even deeper and that a good fit to all P_{nl} data was obtained for the case of no P-wave LVZ. The final earth model for the analysis of seismograms from event 2 is depicted in Figure 9c and tabulated in Table 4. The smoothing of the upper mantle velocity and density gradients has also improved the amplitude fit of the higher mode surface waves (Fig. 9b).

Our study of P_{nl} waveforms confirms Clouser & Langston's (1990) observation that a positive P-wave velocity gradient exists in the upper mantle beneath the Archaean core but we find the gradient is 0.0008 s^{-1} , smaller than in model SACM06c. However, our data imply that if a P-wave LVZ exists, it is much deeper than Clouser & Langston's (1990) upper bound of 170 km.

3.3.4 One-Dimensional Earth Model for the Southern African Craton

Data for eleven other source-receiver paths (Fig. 2) have been analyzed in the same manner as described above, and the results for these are given in Appendix B. The synthetic fits to the observed waveforms shown above for the July 18, 1986 event are typical; some synthetic fits shown in Appendix B are better than those for Event 2 while others are somewhat poorer. The propagation paths for these events primarily sample the stable region of southern Africa but waveforms for some paths sample larger portions of the Proterozoic belts than other paths. There are differences between the models for the twelve paths; however, these are in details and not in the main upper mantle features, suggesting that there are no major lateral variations in the upper mantle structure. We have averaged these models to obtain a 1-D earth model for the Archaean core of southern Africa (Fig. 10 & Table 5). This earth model has the following features. The 42 km thick crust consists of four layers: a 2 km thick 5.05 km s^{-1} surface layer, a 5 km thick 6.08 km s^{-1} upper crust, a 20 km thick 6.30 km s^{-1} mid-crust, and a 15 km thick 6.73 km s^{-1} lower crust. Below the crust there is an 80 km thick upper mantle lid. V_{P_n} and V_{S_n} are 8.09 km s^{-1} and 4.62 km s^{-1} , respectively, and the compressional and shear velocity gradients in the lid are 0.0008 s^{-1} and 0.0013 s^{-1} , respectively. Below the lid there is a substantial shear wave LVZ with the S-wave velocity dropping to 4.32 km s^{-1} at 250 km depth. Below 125 km depth the P-wave gradient increases to 0.0015 s^{-1} and increases again to 0.0035 s^{-1} between 250 km depth and

the 410 discontinuity.

4. DISCUSSION

4.1 Comparison Seismically Determined Velocities with those Estimated from Kimberlite Nodule Data

An important reason for investigating seismic wave propagation across the Archaean cratons of southern Africa is that a great deal of information is now available about the composition, pressure and temperature at depth beneath these cratons from studies of mantle nodules, and the kimberlitic host magmas that transported them to the surface. The pressure and temperature at which the nodules last equilibrated can be estimated from two metamorphic reactions. The intersolubility of ortho- and clinopyroxene is principally dependent on temperature, whereas the solubility of Al_2O_3 in orthopyroxene, in the presence of garnet, is principally controlled by pressure. Finnerty & Boyd (1987) review these and other reactions that can be used as geothermometers and geobarometers. These estimates have been combined with thermal models of the lithosphere (McKenzie, 1989) to obtain the thicknesses of the mechanical and thermal boundary layers beneath the Kaapvaal Craton and surrounding regions. This model is used here, with a mechanical boundary layer thickness of 165 km and a viscosity of $4 \times 10^{15} \text{ m}^2\text{s}^{-1}$ in the thermal boundary layer, to estimate the temperature at depth. It gives a thermal boundary layer thickness of 36 km, a lithospheric thickness of 185 km and a mantle heat flow of 23.1 mWm^{-2} .

The seismic velocities and density depend on the composition and mineralogy of the mantle, as well as on the pressure and temperature. The nodules provide samples of mantle minerals, and the average composition of the more important minerals is listed in Table C1 (see McKenzie & O'Nions, 1991, for details). The proportions of these minerals present at depth, known as the modal mineralogy, can be determined either by point counting, or by finding the proportions of the minerals that best fit the bulk composition of the nodules. The bulk composition can either be measured or calculated from a compositional model of the source. Tainton & McKenzie (1994) showed that all these approaches gave similar estimates of modal mineralogy. Unfortunately the modal mineralogy, mineral and bulk composition have not all been reported for the same nodules. We therefore used the melting models of Tainton & McKenzie (1994) that are consistent with all the information available from the nodules and their host kimberlites to estimate the modal mineralogy as a function of depth. We used the models for four nodule suites: PKP (phlogopite K-richterite peridotite), and GP and GPP (garnet peridotite and garnet phlogopite peridotite) from Erlank *et al.* (1987), and the depleted and fertile nodules from Nixon *et al.* (1981), and obtained the modal mineralogy by minimising the misfit between the bulk composition and that calculated from the phases in Table C1. The minimization used 6 phases, olivine, orthopyroxene, clinopyroxene, garnet, phlogopite and chrome-spinel, and the misfit function was the sum of the squares of the differences between the oxide compositions, with the difference for K_2O weighted by a factor of ten. The modal mineralogy of the four nodule suites is listed in Table C1, together with the parameters used to calculate the density and the seismic velocities from the modal mineralogy. In all cases the ratio of MgO to FeO was fixed to be the same as that in the nodule suite in olivine, orthopyroxene and clinopyroxene. The method used to obtain ρ , V_P and V_S is outlined in the Appendix C, and can be used to calculate these parameters for any rock that consists of the minerals in Table C1.

The nodule compositions from southern Africa show that the composition of the upper mantle sampled by the kimberlites varies with depth. Unfortunately, accurate depth estimates cannot be made for the four suites listed in Table C1 because their mineral compositions have not been reported. But Waters & Erlank (1988) suggest that the PKP nodules come from depths of about 100 – 130 km. Depleted, GP and GPP nodules give pressure estimates from 100 – 150 km and

fertile nodules from 160 – 200 km (see Tainton & McKenzie, 1994).

The velocities and density computed from the nodules are given in Table 6; the details of the calculations are given in Appendix C. The petrological estimates are compared with the seismic velocities and density in Figure 10 and the lid values are in excellent agreement, which gives strong support for the proposed upper mantle composition and also implies that the upper mantle conditions deduced from the petrological data are representative of the Archaean core of southern Africa,

However, we predict significantly higher velocities and densities from the deepest nodules (Table 6) compared to the velocities and density at corresponding depths in our seismic model. The largest difference is for the S-wave velocity. The depth to the top of the S-wave LVZ in our model for southern Africa is 122 km and we argue in Appendix B that this is resolvable to about ± 30 km. Thus even the maximum depth to the top of the LVZ is in disagreement with the deepest nodule data. This discrepancy is greatest for the S-wave velocity and the reason for this may be due to the presence of small melt fractions just below the seismically defined upper-mantle lid. McKenzie (1989) has shown that small melt fractions are likely to be present beneath the lithosphere and these will separate from the matrix when there is more than about $10^{-3}\%$ melt present if their viscosity is 0.1 Pa s. Once separated these melts will migrate upwards but, since such melts movement cannot transport heat, they will solidify within the mechanical boundary layer at temperatures between 950° and 750° (McKenzie, 1989). The corresponding depths can be estimated from the nodule data and for the Kaapvaal Craton these temperatures correspond to depths of 120 to 100 km if the dihedral angle is as small as zero. Below this depth this small melt fraction can coat the grain boundaries of the matrix with a thin film. Such a film has been assumed to be absent when the bulk elastic parameters are calculated from the modal mineralogy. Though its presence would have little effect on the density and bulk modulus, the same is not true of the shear modulus. Lubrication of the grain boundaries could have a significant effect on the shear modulus, which controls V_s (O'Connell & Budiansky, 1974).

4.2 Geological Implications of the Velocity Structure

Though southern Africa has not been deformed since the Archaean, it has undergone regional uplift of at least 1 km over very large regions. McKenzie (1984) and Cox (1993) have suggested that this uplift results from the underplating of Karoo basalts. This suggestion is consistent with our velocity model if such material is emplaced in the lower crust. The velocities and density of the 15 km thick layer, at depths of 27-42 km, are typical of those of basalt, and emplacement of such a layer would produce an uplift of 1.4 km.

The velocity of the S waves in the high velocity mantle lid agree better with those calculated for the PKP nodules. Though the difference between the velocities of different nodule types is scarcely larger than the likely modelling errors, only the PKP nodules come from depths between 52 and 122 km, corresponding to the high velocity lid. The velocities of the PKP nodules are less than those of the other nodule types because their potassium oxide content of 0.86% stabilises phlogopite and the amphibole k-richterite (Table C1). Both minerals contain Al_2O_3 , hence reducing the proportion of garnet. Furthermore the seismic velocities of amphibole and phlogopite are considerably lower than are those of garnet (Table C1). The agreement between the PKP parameters and those of the best fitting seismic model therefore suggests that mica, rather than garnet, peridotite is the rock type that is present in the upper mantle over much of southern Africa. This conclusion is consistent with the petrological observations. Cox (1983) in particular has argued that the potassium concentration in the Karoo picrites from the Lebombo monocline requires them to have been derived from two end members, one of which is a typical low potassium plume basalt and the other a K-rich melt with 4% K_2O that is easily produced by melting material with the composition of PKP nodules. However, as Cox (1983) remarks, the

enormous volume of the picrites require a large source of the K-rich magma. If the lid consists of PKP material and is 60 km thick, 1% melting generates 600 m of magma. Cox's (1983) model requires the 2 km thickness of the picrites to contain about 500 m of the K-rich melt. There is therefore no obvious difficulty in accounting for the geological observations in this way.

The difference between the velocities estimated from the seismological observations below a depth of 122 km and those from the deeper nodules is considerably larger than the estimated uncertainties (Fig. 10). Though presence of a very small (0.1%) melt fraction with a dihedral angle that is small or zero seems a plausible explanation for the observations, and its upward percolation can account for the potassium enrichment seen in the PKP nodules, it is not likely that the whole region between 120 and 400 km contains melt. Melting is generally accompanied by an increase in volume, and hence the solidus temperature increases with pressure. However, the velocity structure of the LVZ is not yet well constrained by the seismic observations (see Fig. 10), and therefore may be less different from that calculated from the deeper nodules than our model suggests. Furthermore, all the nodules consist of mantle that has been depleted by considerable amounts of basalt extraction, a process that lowers the density and increases the seismic velocities. The upper mantle beneath the lithosphere has not been depleted in this way, and the density and seismic velocities at depths greater than about 200 km should be compared with those calculated for the undepleted material, and not with the values from the nodules.

4.3 Comparison with Previous Southern African Seismological Models

Figure 11 compares our earth model with several previously published models for southern Africa. Bloch *et al.* (1969) used fundamental mode Rayleigh wave phase velocity and fundamental and higher mode Love and Rayleigh wave group velocities to determine the crust and upper mantle shear wave structure in the same region as our study, and we used their mantle model for our starting model in the waveform inversion. The two shear wave models have similar upper mantle lids and LVZ; however, the average mantle lid velocity of the Bloch *et al.* (1969) model is higher than in our model and the average velocity in the LVZ is lower. Our lid shear wave velocity is controlled by the V_{S_n} observations (Fig. 5); if we had assumed a higher V_{S_n} , this would result in lower velocities in the LVZ. Figure 12 compares Bloch *et al.* (1969) dispersion data with the dispersion curves computed for our model. The observed Rayleigh wave group velocity curves are well fit by the group velocity curves predicted by our model at periods greater than about 5 seconds. The Love wave group velocity curves are well fit above about 9 seconds period where the fundamental and first higher mode interfere. The predicted Rayleigh wave phase velocity curves underestimate the observed phase velocities. The curvature of the fundamental mode Rayleigh wave phase velocity curves near 40 s period (the Airy phase) which is matched in Figure 12, provides the greatest dispersion constraint on the lid thickness (Priestley *et al.*, 1980). The observed phase velocities in this period range suggest that velocities in the lower part of the lid may be slightly higher than in our model; however Figure 7a shows that synthetic seismograms computed for the Bloch *et al.* (1969) model do not fit the observed seismograms. We feel that the inversion of the multi-mode waveform data coupled with the V_{S_n} data from Figure 5 provides stronger constraints on the upper mantle structure than is provided by the two-stage process of computing the fundamental mode dispersion curve and inverting that for the upper mantle structure.

Cichowicz & Green (1992) use the partitioned waveform inversion method of Nolet (1990) to invert Rayleigh wave data from two teleseismic earthquakes recorded on four broadband seismographs deployed along a profile extending southwest from the central Kaapvaal Craton into the adjacent Namaqua mobile belt. Three of their upper mantle shear wave models, obtained by including 3, 6, and 11 eigenvectors in their inversion, are shown in comparison to our shear velocity model in Figure 11. The model with 3 eigenvectors is almost horizontally homogeneous

whereas the other models show an upper mantle lid. However their lid is significantly thinner and their upper mantle shear wave LVZ significantly shallower than that found in our study. Figure 13 compares reflectivity synthetics for Event 2 computed from the final crustal model for this event, overlying the upper mantle models of Cichowicz & Green (1992). These synthetic waveforms show little resemblance to the observed waveforms. We used the Bloch *et al.* (1969) shear wave structure as the starting mantle model in our inversion. We constructed a new starting model using the average crustal model from the seismic refraction and receiver function modeling, and the Cichowicz & Green (1992) $n = 6$ mantle model and reinverted the Event 2 seismograms from SLR. The resulting inversion velocity structure which employed this new starting model converged towards our original result for this event, giving us confidence that the differences between our upper mantle model and those of Cichowicz & Green (1992) were not simply the result of our choice of a starting model.

Clouser & Langston (1990) derived upper mantle compressional wave models for both cratonic and mobile belt regions of southern Africa by forward modeling P_{nl} waveforms from two moderate earthquakes in Zimbabwe recorded on long period seismographs in southern Africa. In our study of the P_{nl} waveforms we have followed the same approach in deriving our upper mantle P-wave velocity model. Clouser & Langston (1990) conclude that a model with an upper mantle P-wave velocity gradient of 0.0033 s^{-1} and a P-wave LVZ no shallower than 170 km best fit the data for the craton. This velocity model, SACM06c, is shown in Fig. 11 for comparison with our model. Since SACM06c only extends to 275 km depth, we have extended the gradient below this depth. The seismograms which control the deeper part of model SACM06c were recorded at an epicentral distance of about 1100 km. Nearer events could be fit with structures containing a P-wave LVZ as shallow as 130 km. The events discussed in Appendix B have epicentral distances as great as 3000 km and hence have deeper turning depths. Figure 14a shows that reflectivity synthetics computed for the model SACM06c closely match the observed Event 2 waveforms at SLR ($\Delta = 1038 \text{ km}$). However, the synthetics P-wave computed for SACM06c arrives about 3 s earlier than the observed P-wave arrival time of the March 9, 1989 earthquake (Event 4, Table 1) recorded at SLR ($\Delta = 1479 \text{ km}$) (Fig. 14b). This early arrival time arises because of the steeper upper mantle gradient in model SACM06c compared to the upper mantle gradient in our model. However the narrow P-wave LVZ in model SACM06c has little effect on the deeper turning P-wave from the July 24, 1991 earthquake (Event 10, Table 1) recorded at SUR ($\Delta = 2106 \text{ km}$). From the tests we have made in comparing synthetics with the observations (see Appendix B), we conclude that if a P-wave LVZ exists beneath the Archaean core it is deeper than 250 km depth. It is more likely that there is no P-wave LVZ beneath the Archaean core.

Figure 11 also shows the P-wave model of Green (1978) for eastern and southern Africa which was derived from travel times of accurately located earthquakes in east Africa recorded at seismographs in eastern and southern Africa. The shallow part of the model (< 250 km depth) is constrained using seismograms of east African earthquakes recorded at east African stations and therefore characteristic of the upper mantle beneath the East African Rift. The P-wave velocity at these depths is low compared to that beneath the craton. The model below 250 km depth is constrained by seismograms recorded on the shield and at these depths Green's model is not significantly different from the model we have determined from the body wave modeling.

4.4 Comparison with other Earth Models for Shield Regions

The agreement of *in situ* velocities and density estimates at upper mantle depths beneath the Kaapvaal Craton made from petrological analysis of the kimberlite nodules and the seismically determined velocities and density suggests that the nodule estimates are representative of the wider region of the Archaean core. It is interesting to compare the southern African results with other shield regions from which little upper mantle nodule data is available. Figure 15 compares

earth models for the Australian, Baltic, and Canadian shields with the southern African model. The shear velocity models were derived from either forward fitting (Canadian Shield – Brune & Dorman, 1963) or inversion (Baltic Shields – Calcagnile, 1991) of surface wave dispersion data, or by forward modeling S-waves recorded in the regional distance range (Kennett *et al.*, 1994). The compressional velocity models were determined from either forward modeling long-period (Baltic – Given & Helmberger, 1980; Canadian Shields – LeFevre & Helmberger, 1989) or broadband (Australian Shield – Bowman & Kennett, 1990) P-waveforms but generally at larger distance ranges than those modeled for southern Africa.

The upper mantle model for southern Africa has features similar to the upper mantle beneath the Canadian and Baltic Shields. The shear wave structure for all three regions shows an upper mantle lid with shear wave velocities varying from about 4.65 to 4.70 km s^{-1} . Neither the Canadian nor Baltic shield models show a gradient in the lid but this is probably due to limitations in the method of analysis. The seismically determined velocities in the lid of all three models are in reasonable agreement with the velocity estimates from the nodule data from the Kaapvaal Craton kimberlites. The lid overlies a shear wave LVZ which begins at about 110 – 120 km depth. The lowest velocities in the LVZ are at depths of about 250 km depth in each of the three regions. The upper part of the Australian shield shear wave model is similar to the shear wave structure for the other three shields. However the S-wave velocity reversal seen below the other shields at 120 to 150 km depth does not occur beneath the Australian shield until depths of 200 to 225 km .

There is more variation in the P-wave models for the four shield regions. Below about 220 km depth the Canadian and Baltic Shield models are similar to the southern African model; however, above this the models are significantly different. Both the Canadian and Baltic Shield models have a high velocity P-wave lid above a P-wave LVZ but the nature of the lid and the LVZ is different in the two models. The P_n velocity in the Baltic Shield model is about 8.2 km s^{-1} and the lid extends to a depth of about 140 km ; the Canadian Shield model has a P_n velocity of about 8.4 km s^{-1} and the lid extends to a depth of about 170 km . In contrast, the southern African P_n velocity is 8.1 km s^{-1} and there is no P-wave LVZ. The P-wave velocity gradients in the lid of the Canadian and Baltic Shield models are similar to that in the southern African model. The P-wave velocities of the Canadian and Baltic Shield models do not agree with the estimates from the kimberlite nodules from the Kaapvaal craton. The Australian Shield P-wave model does not contain a LVZ but has a significantly higher velocity than the southern African model and does not correspond to the same structure as the other models below 220 km depth.

5. CONCLUSIONS

We present a new 1-D velocity and density model for the crust and upper mantle beneath southern Africa. The crustal velocity structure is derived from modeling teleseismic receiver function data and from published seismic refraction crustal models. The mantle model is derived from inversion of multi-mode regional surface waveforms and forward modeling of P_{nl} waveforms. The average crust and upper mantle model derived from analysis of data from twelve paths largely confined to the Archaean core of southern Africa has the following major features. The 42 km thick crust consists of four layers: a 2 km thick 5.05 km s^{-1} surface layer, a 5 km thick 6.08 km s^{-1} upper crust, a 20 km thick 6.30 km s^{-1} mid-crust, and a 15 km thick 6.73 km s^{-1} lower crust. Below the crust there is an 80 km thick upper mantle lid. V_{P_n} and V_{S_n} are 8.09 and 4.62 km s^{-1} , respectively, and the compressional and shear velocity gradients in the lid are 0.0008 s^{-1} and 0.0013 s^{-1} , respectively. Below the lid there is a substantial S-wave LVZ with the shear wave velocity dropping to 4.32 km s^{-1} at 250 km depth. The S-wave LVZ is required to both explain the V_{S_n} measurements and fit the regional surface waveforms. Forward modeling of P_{nl} waveforms does not require an upper mantle P-wave LVZ. Below 125 km depth the P-wave

gradient increases to 0.0015 s^{-1} and increases again to 0.0035 s^{-1} between 250 km depth and the 410 discontinuity. The distribution of earthquakes and seismographs used in this study has not provided adequate data to resolve the question of deep lithospheric differences in the structure beneath the Archaean cratons and the Proterozoic mobile belts.

We have estimated the upper mantle lid velocities and density from the composition of the nodules brought up by kimberlites through the Kaapvaal Craton. These values are in good agreement with the seismically determined upper mantle lid velocities and density for the Archaean core of southern Africa, suggesting that the nodule data is representative of the wider region and not just the region beneath where they are found.

ACKNOWLEDGEMENTS

We would like to thank Joan Gomberg for the copy of the locked-mode inversion routine and Rick Benson for assisting us with retrieving seismic data from the IRIS DMC. This research was partially supported by contract F19628-95-K-0017 from the Phillips Laboratory, Hanscom AFB, Ma.

REFERENCES

Ammon, C.J., Randall, G.E., & Zandt, G., 1990. On the nonuniqueness of receiver function inversions, *J. geophys. Res.*, **95**, 15303–15318.

Ammon, C.J., 1991. The isolation of receiver effects from teleseismic P waveforms, *Bull. seism. Soc. Am.*, **81**, 2504–2510.

Baier, B., Berckhemer, H., Gajewski, D., Green, R.W., Grimsel, C., Prodehl, C. & Vees, R., 1983. Deep seismic sounding in the area of the Damara Orogen, Namibia, southwest Africa, in *Intracontinental Fold Belts*, pp. 885–900, eds Martin, H. & Eder, F.W., Springer-Verlag, Berlin.

Ballard, S. & Pollack, H.N., 1987. Diversion of heat by Archaean cratons: a model for southern Africa, *Earth and Planetary Science Letters*, **85**, 253–264.

Bath, M., & Stefansson, R., 1966. S-P conversion at the base of the crust, *Ann. Geofis. (Rome)*, **19**, 119–130.

Biswas, N.N. & Knopoff, L., 1970. Exact-earth-flattening calculation for Love waves, *Bull. seism. Soc. Am.*, **60**, 1123–1137.

Biswas, N.N., 1972. Exact-flattening procedure for the propagation of Rayleigh waves, *Pageoph.*, **96**, 61–74.

Bloch, S., Hales, A.L. & Landisman, M., 1969. Velocities in the crust and upper mantle of southern Africa from multi-mode surface wave dispersion, *Bull. seism. Soc. Am.*, **59**, 1599–1629.

Bowman, J.R. & Kennett, B.L.N., 1990. An investigation of the upper mantle beneath north-western Australia using a hybrid seismograph array, *Geophys. J. Int.*, **101** 411–424.

Brune, J. & Dorman, J., 1963. Seismic waves and earth structure in the Canadian shield, *Bull. seism. Soc. Am.*, **53**, 167–210.

Cahen, L.C., & Snelling, N.J., 1966. *The Geochronology of Equatorial Africa*, North-Holland Publishing Co., Amsterdam.

Calcagnile, G., 1991. Deep structure of Fennoscandia from fundamental and higher mode dispersion of Rayleigh waves, *Tectonophysics*, **195**, 139–149.

Cichowicz, A., & Green, R., 1992. Tomographic study of upper-mantle structure of the South African continent using wave-form inversion, *Phys. Earth. Plant. Int.*, **72**, 276–285.

Clifford, T.N., 1970. The structural framework of Africa, in *African Magmatism and Tectonics*, ed. Clifford, T.N., & Gass, I.G., Hafner Pub. Co., Darien, Conn., 1–26.

Clouser, R.H. & Langston, C.A., 1990. Upper mantle structure of southern Africa from P_{nl} waves, *J. geophys. Res.*, **95**, 17,403–17,415.

Cox, K.G., 1983. The Karoo province of southern Africa: origin of trace element enrichment patterns, in: *Continental Basalts and Mantle Xenoliths* ed Hawkesworth, C.J., and Norry, M.J., Shiva Publishing, Nautwich, Cheshire, 139–157.

Cox, K.G., 1993. Continental magmatic underplating, *Phil. Trans. R. soc. Lond.*, **A342**, 155–166.

Dawson, J.B., 1980. *Kimberlites and their Xenoliths*, Springer-Verlag, Berlin.

de Beer, J.H., & Stettler, E.H., 1992. The deep structure of the Limpopo Belt from geophysical studies, *Precambrian Res.*, **55**, 173–186.

de Wit, M.J., Roering, C., Hart, R.J., Armstrong, R.A., de Ronde, C.E.J., Green, R.W.E., Tredoux, M., Peberdy, E. & Hart, R.A., 1992. Formation of an Archaean continent, *Nature*, **357**, 553–562.

Durrheim, R.J., Barker, W.H. & Green, R.W.E., 1992. Seismic studies in the Limpopo Belt, *Precambrian Res.*, **55**, 187–200.

Durrheim, R.J. & Green, R.W.E., 1992. A seismic refraction investigation of the Archaean Kaapvaal Craton, South Africa, using mine tremors as the energy source, *Geophys. J. Int.*, **108**, 812–832.

Durrheim, R.J. & Mooney, W.D., 1991. Archaean and Proterozoic crustal evolution: Evidence from crustal seismology, *Geology*, **19**, 606–609.

Erlank, A.J., Waters, F.G., Hawkesworth, C.J., Haggerty, S.E., Allsopp, H.L., Rickard, R.S., & Menzies, M.A., 1987. Evidence for mantle metasomatism in peridotite nodules from the Kimberly Pipes, South Africa, in *Mantle Metasomatism*, ed. M.A. Menzies and C.J. Hawkesworth, Academic Press, London, 221–311.

Evernden, J., 1967. Magnitude determination at regional and near-regional distances in the United States, *Bull. Seis. Soc. Am.*, **57**, 591–639.

Finnerty, A.A., & Boyd, F.R.. Thermobarometry for garnet peridotites: Basis for the determination of thermal and compositional structure of the upper mantle, in *Mantle Xenoliths* ed. P.H. Nixson, J. Wiley & sons, New York, 381–402.

Fuchs, K. & Müller, G., 1971. Computation of synthetic seismograms with the reflectivity method and comparison with observations, *Geophys. J. R. astr. Soc.*, **23**, 417–433.

Gane, P.G., Atkins, A.R., Sellschop, J.P.F. & Seligman, P., 1956. Crustal structure in the Transvaal, *Bull. seism. Soc. Am.*, **46**, 293–316.

Given, J.W. & Helmberger, D.V., 1980. Upper Mantle Structure of Northwestern Eurasia, *J. geophys. Res.*, **85**, 7183–7194.

Gomberg, J.S. & Masters, T.G., 1988. Waveform modelling using locked-mode synthetic and differential seismograms: application to determination of the structure of Mexico, *Geophysical Journal*, **94**, 193–218.

Green, A.G., 1978. An upper mantle P wave velocity model for eastern and southern Africa, *Pure Appl. Geophys.*, **116**, 1262–1273.

Green, R.W.E. & Durrheim, R.J., 1990. A seismic refraction investigation of the Namaqualand Metamorphic Complex, South Africa, *J. geophys. Res.*, **95**, 19 927–19 932.

Gumper, F. & Pomeroy, W., 1970. Seismic wave velocities and earth structure on the African continent, *Bull. seism. Soc. Am.*, **60**, 651–668.

Gurney, J.J. 1990. The diamondiferous roots of our wandering continent, *S. Afri. J. Geol.*, **93**, 424–437.

Gwavava, O., Swain, C.J., Podmore, F., & Fairhead, J.D., 1992. Evidence of crustal thinning beneath the Limpopo Belt and Lebombo monocline of southern Africa based on regional gravity studies and implications for the reconstruction of Gondwana, *Tectonophysics*, **212**, 1–20.

Hales, A.L. & Sacks, I.S., 1959. Evidence for an intermediate layer from crustal structure studies in the eastern Transvaal, *Geophys. J. R. astr. Soc.*, **2**, 15–33.

Helmburger, D.V. & Engen, G.R., 1980. Modeling the long-period body waves from shallow earthquakes at regional ranges, *Bull. Seism. Soc. Am.*, **70**, 1699–1741.

Hill, R., 1952. The elastic behaviour of a crystalline aggregate, *Proc. Phys. Soc. London, Ser. A.*, **65**, 349–354.

Hill, D.P., 1971. Velocity gradients and anelasticity from crustal body wave amplitudes, *J. geophys. Res.*, **76**, 3309–3325.

Hill, D.P., 1973. Critically refracted waves in a spherically symmetric radially heterogeneous Earth model, *Geophys. J. R. astr. Soc.*, **34**, 149–177.

Huestis, S., Molnar, P., & Oliver, J., 1973. Regional S_n velocities and shear velocity in the upper mantle, *Bull. seism. Soc. Am.*, **63**, 469–475.

Kennett, B.L.N., Gudmundsson, O., & Tong, C., 1994. The upper-mantle S and P velocity structure beneath northern Australia from broad-band observations, *Phys. Earth. Planet. Int.*, **86**, 85–98.

Kroner, A., 1977. Precambrian mobile belts of southern and eastern Africa: Ancient sutures or sites of ensialic mobility? A case for crustal evolution towards plate tectonics, *Tectonophysics*, **40**, 101–135.

Langston, C.A., 1979. Structure under Mount Rainier, Washington, inferred from teleseismic body waves, *J. geophys. Res.*, **84**, 4749–4762.

Langston, C.A., 1982. Aspects of P_n and P_g propagation at regional distances, *Bull. seism. Soc. Am.*, **72**, 457–471.

LeFevre, L.V. & Helmburger, D.V., 1989. Upper mantle P-velocity structure of the Canadian shield, *J. geophys. Res.*, **94**, 17749–17766.

Liu, H., Anderson, D.L. & Kanamori, H., 1976. Velocity dispersion due to anelasticity: implications for seismology and mantle composition, *Geophys. J. R. astr. Soc.*, **47**, 41–58.

McElhinny, M.W. & McWilliams, M.O., 1977. Precambrian geodynamics – a paleomagnetic view, *Tectonophysics*, **40**, 137–159.

McKenzie, D., 1984. A possible mechanism for epeirogenic uplift, *Nature*, **307**, 616–618.

McKenzie, D., 1989. Some remarks on the movement of small melt fractions in the mantle, *Earth and Planetary Sciences Letters*, **95**, 53–72.

McKenzie, D., & O'Nions, R.K., 1991. Partial melt distributions from inversion of rare earth element concentrations, *J. Petrology*, **32**, 1021–1091.

Molnar, P. & Oliver, J., 1969. Lateral variations of attenuation in the upper mantle and discontinuities in the lithosphere, *J. geophys. Res.*, **74**, 2648–2682.

Nataf, H.C., Nakanishi, I., & Anderson, D.L., 1984. Anisotropy and shear-velocity heterogeneities in the upper mantle, *Geophys. Res.*, **11**, 109–112.

Nixon, P.H., Rogers, N.W., Gibson, I.L., & Grey, A., 1981. Depleted and fertile mantle xenoliths from southern African kimberlites, *Ann. Rev. Earth. Planet. Sci.*, **9**, 285–309.

Nolet, G., 1990. Partitioned wave-form inversion and two-dimensional structure under the Network of Autonomously Recording Seismographs, *J. geophys. Res.*, **95**, 8499–8512.

O'Connell, R.J., & Budiansky, B., 1974. Seismic velocities in dry and saturated cracked solids, *J. geophys. Res.*, **79**, 5412–5426.

Oliver, J. & Major, M., 1960. Leaking modes and the PL phase, *Bull. seism. Soc. Am.*, **50**, 165–180.

Oliver, J., 1964. Propagation of PL waves across the United States, *Bull. seism. Soc. Am.*, **54**, 151–160.

Owens, T.J., Zandt, G., & Taylor, S.R., 1984. Seismic evidence for an ancient rift beneath the Cumberland Plateau, Tennessee: A detailed analysis of broadband teleseismic P waveforms, *J. geophys. Res.*, **89**, 7783–7795.

Pasteris, J.D., 1983. Kimberlites: A look into the Earth's mantle, *American Scientist*, **71**, 282–288.

Priestley, K. & Brune, J., 1978. Surface waves and the structure of the Great Basin of Nevada and western Utah, *J. geophys. Res.*, **83**, 2265–2272.

Priestley, K., Orcutt, J.A., & Brune, J.N., 1980. Higher-mode surface waves and the structure of the Great Basin of Nevada and western Utah, *J. geophys. Res.*, **85**, 7166–7174.

Richardson, S.H., Gurney, J.H., Erlank A.J. & Harris, J.W., 1984. Origin of diamonds in old enriched mantle, *Nature*, **310**, 198–202.

Shaw, P. & Orcutt, J., 1984. Propagation of PL and implications for the structure of Tibet, *J. geophys. Res.*, **89**, 3135–3152.

Stuart, G.W. & Zengeni, T.G., 1987. Seismic crustal structure of the Limpopo mobile belt, Zimbabwe, *Tectonophysics*, **144**, 323–335.

Tainton, K.M. & McKenzie, D., 1994. The Generation of kimberlites, lamproites, and their source rocks, *Journal of Petrology*, **35**, 787–817.

Tankard, A.J., Jackson, M.P.A., Eriksson, K.A., Hobday, D.K., Hunter, D.R. & Minter, W.E.L., (ed.), 1982. *Crustal evolution of southern Africa: 3.8 billion years of earth history*,

Springer-Verlag, New York.

Vinnik, L.P., Green, R.W.E., & Nicolaysen, L.O., 1995. Recent deformations of the deep continental root beneath southern Africa, *Nature*, **375**, 50–52.

Waters, F.G., & Erlank, A.J., 1988. Assessment of the vertical extent and distribution of mantle metasomatism below Kimberly, South Africa, *J. Petrol.*, Special Lithosphere issue, 185–204.

Willmore, P.L., Hales, A.L. & Gane, P.G., 1952. A seismic investigation of crustal structure in the western Transvaal, *Bull. seism. Soc. Am.*, **42**, 53–80.

Wright, J.A. & Hall, J., 1990. Deep seismic profiling in the Nosop Basin, Botswana: cratons, mobile belts and sedimentary basins, *Tectonophysics*, **173**, 333–343.

Table 1. Regional Events in Southern Africa

No	DATE			TIME			LAT.	LONG.	DEPTH	Mb	Ms
1 [†]	1983	7	7	20	35	37.4	-7.41	27.88	10	5.8	5.5
2 [†]	1986	7	18	15	7	52	-16.36	28.48	17	5.4	4.8
3 [†]	1988	4	16	21	17	9.9	-10.26	27.71	10	5.4	4.7
4 [†]	1989	3	9	2	37	0.2	-13.74	34.41	30	5.6	5.4
5 [†]	1989	3	10	21	49	45.8	-13.70	34.45	30	6.0	6.1
6 [†]	1989	9	29	6	16	31	-30.60	28.70	7	4.8	4.1
7 [†]	1990	9	26	23	8	23.1	-28.10	26.77	2	5.3	4.3
8 [†]	1990	11	3	0	31	28.9	-21.35	33.28	10	4.8	5.1
9 [†]	1991	5	10	1	12	38.5	-17.35	24.98	10	4.8	3.8
10 [†]	1991	7	24	13	54	51.9	-18.27	34.86	32	5.1	4.9
11 [†]	1991	11	3	18	28	55	-26.89	26.64	1	5.0	
12 [‡]	1994	8	18	0	45	47.2	-7.43	31.75	25	6.0	5.7
13 [‡]	1994	10	30	6	6	27.4	-28.03	26.74	5	5.6	4.7
14 [‡]	1995	1	2	15	16	2.2	-26.36	27.22	5	4.3	

[†]ISC

[‡]PDE

Table 2. Regional Earthquake Source Mechanisms

Event	CMT solutions*					source mechanisms used				
	depth (km)	$M_o \cdot 10^{24}$ (dyn cm)	ϕ	δ	λ	depth (km)	$M_o \cdot 10^{24}$ (dyn cm)	ϕ	δ	λ
830707	24.1	5.700	200	41	-111	6.0	5.700	200	41	-111
860718	15.0	0.783	238	43	-84	12.0	0.783	238	43	-84
880416	15.0	0.535	10	26	-120	10.0	0.428	353	18	-139
890309	15.0	3.690	128	23	-118	30.0	1.845	128	23	-118
890310	15.0	31.100	142	17	-102	30.0	15.552	154	34	-92
901103	15.0	0.592	345	35	-111	10.0	0.700	310	20	-132
910724	24.7	0.518	180	45	-90	32.0	0.518	180	45	-90
940818	30.9	9.300	306	28	-110	30.9	9.300	306	28	-110

*Harvard centroid moment tensor catalogue

Table 3. Southern African Digital Seismograph Stations.

Code	Lat.	Long.	Elev.	Site - Name
SLR	-25.7349	28.2816	1348.0	Silverton, South Africa
SUR	-32.3797	20.8117	1770.0	Sutherland, South Africa
BOSA	-28.6131	25.4156	1280.0	Boshof, South Africa
LBTB	-25.0145	25.5970	1128.0	Lobatse, Botswana, Africa
LSZ	-15.2766	28.1882	1184.8	Lusaka, Zambia, Africa
TSUM	-19.2022	17.5838	1240.0	Tsumeb, Namibia, Africa

Table 4. Earth Model for July 18, 1986 – SLR Path

Depth km	Thick. km	V_P km s^{-1}	V_S km s^{-1}	ρ g cm^{-3}	Depth km	Thick. km	V_P km s^{-1}	V_S km s^{-1}	ρ g cm^{-3}
0	1	4.52	2.44	2.09	199	21	8.34	4.26	3.41
1	5	5.80	3.67	2.31	219	21	8.38	4.14	3.44
6	20	6.45	3.71	2.80	240	23	8.44	4.10	3.45
26	14	6.60	3.92	2.88	263	23	8.53	4.10	3.46
40	13	8.10	4.64	3.35	287	23	8.62	4.10	3.48
53	13	8.12	4.65	3.35	310	17	8.69	4.17	3.49
66	13	8.13	4.67	3.35	327	17	8.75	4.29	3.51
78	13	8.15	4.68	3.35	343	17	8.81	4.42	3.52
91	13	8.17	4.69	3.35	360	17	8.88	4.55	3.54
104	13	8.20	4.72	3.35	377	17	8.94	4.68	3.55
116	21	8.21	4.56	3.35	393	17	9.03	4.87	3.57
137	21	8.24	4.48	3.37	410	42	9.36	5.07	3.76
158	21	8.27	4.41	3.38	452	8	9.50	5.16	3.81
178	21	8.31	4.33	3.40					

Table 5. Average Velocity Model for Southern Africa.

Depth km	Thick. km	V_P km s^{-1}	V_S km s^{-1}	ρ g cm^{-3}	Depth km	Thick. km	V_P km s^{-1}	V_S km s^{-1}	ρ g cm^{-3}
0	2	5.05	2.88	2.36	232	10	8.33	4.32	3.43
2	5	6.08	3.59	2.74	242	10	8.35	4.32	3.43
7	20	6.30	3.68	2.88	252	10	8.38	4.32	3.44
27	15	6.73	4.04	3.00	262	10	8.41	4.34	3.45
42	10	8.09	4.62	3.30	272	10	8.44	4.35	3.45
52	10	8.09	4.63	3.31	282	10	8.48	4.38	3.46
62	10	8.10	4.65	3.32	292	10	8.51	4.41	3.47
72	10	8.11	4.66	3.32	302	10	8.55	4.43	3.48
82	10	8.12	4.68	3.33	312	10	8.58	4.47	3.48
92	10	8.13	4.70	3.34	322	10	8.62	4.50	3.49
102	10	8.14	4.71	3.35	332	10	8.65	4.54	3.50
112	10	8.15	4.72	3.35	342	10	8.69	4.58	3.51
122	10	8.17	4.50	3.37	352	10	8.73	4.61	3.51
132	10	8.18	4.46	3.37	362	10	8.76	4.65	3.52
142	10	8.20	4.44	3.38	372	10	8.80	4.68	3.53
152	10	8.21	4.43	3.38	382	10	8.83	4.72	3.54
162	10	8.22	4.41	3.39	392	10	8.87	4.76	3.54
172	10	8.24	4.39	3.39	402	9	8.90	4.79	3.55
182	10	8.25	4.38	3.40	411	10	9.31	5.01	3.76
192	10	8.26	4.36	3.40	421	10	9.34	5.04	3.78
202	10	8.28	4.35	3.41	431	10	9.38	5.06	3.79
212	10	8.30	4.34	3.42	441	10	9.42	5.09	3.80
222	10	8.31	4.33	3.42	451	0	9.45	5.11	3.81

Table 6. Upper Mantle Parameters for Nodule Analysis.

Nodule	Comp.	Temp.	Press.	Depth	V_P	V_S	ρ
PKP	Sp. P.	371	1.61865	50	8.078	4.627	3.333
PKP	Sp. P.	557	2.42798	75	8.086	4.632	3.338
PKP	Gar. P	743	3.23730	100	8.094	4.637	3.343
PKP	Gar. P	854	3.72290	115	8.099	4.641	3.346
Depleted	Gar. P	1058	4.04663	125	8.327	4.830	3.298
Fertile	Gar. P	1380	5.82714	180	8.394	4.864	3.311

FIGURE CAPTIONS

Figure 1. Tectonic map of southern Africa showing the major geologic subdivisions (after Cahen & Snelling, 1966). The locations of the kimberlite pipes are shown by the solid diamonds and are those from which the samples used by Tainton & McKenzie (1994) were obtained.

Figure 2. Source – receiver paths for regional earthquake seismograms used in this study superimposed on the major crustal subdivisions of southern Africa. Solid triangles denote seismograph stations; stars denote earthquake locations; solid lines denote paths for the events used in the regional waveform modeling; and dotted lines denote paths for events used in constructing the P_n , S_n , L_g composite record-section. Events 2-SLR, 5-SLR, 8-SLR, and 12-LSZ were used for waveform modeling and the record section. The numbers for the earthquakes refer to Table 1.

Figure 3. Results of the teleseismic receiver function analysis for data from the station BOSA. The solid line is the observed receiver function and the dashed line denotes \pm one standard deviation. The dotted line corresponds to the synthetic receiver function computed from the crustal velocity structure shown in the inset. We have annotated the receiver function with the phases corresponding to the relevant features of the model shown in the inset. In labeling these phases we have used the convention of Bath & Stefansson (1966). The l and m in the inset velocity model denote the boundary where the corresponding P-to-S conversions in the synthetic receiver function occur.

Figure 4. Measured values of crustal thickness in southern Africa. Large circles denote location of teleseismic receiver function crustal thickness estimates from this study; small circles denote location of seismic refraction crustal thickness estimates. The letter in parenthesis following the refraction estimates corresponds to the following references: (i) Willmore *et al.*, 1952, (ii) Gane *et al.*, 1956, (iii) Hales & Sacks, 1959, (iv) Baier *et al.*, 1983, (v) Stuart & Zengeni, 1987, (vi) Green & Durrheim, 1990, (vii) Durrheim & Green, 1992, (viii) Durrheim *et al.*, 1992, (ix) Wright & Hall, 1990.

Figure 5. High-frequency body wave composite, reduced record-section from seismograms of the earthquakes and seismographs shown in Figure 2. The travel time relationships for the P_n , S_n , and L_g phases are shown on the right hand edge of the plot.

Figure 6. Vertical component short-period and three component long-period seismograms for the July 18, 1986 (Event 2, Table 1) earthquake recorded at SLR. The seismograms are annotated with the predicted IASPEI P and S wave arrival times and with our interpretation of the various arrivals.

Figure 7. (a) Comparison of the July 18, 1986 earthquake (Event 2, Table 1) long-period seismograms recorded at SLR (solid line) with normal mode synthetics seismograms computed for the starting model, the CMT source mechanism, and the ISC depth (dotted line). (b) Comparison of the same seismograms and locked-mode synthetic seismograms (dotted lines) computed using the velocity model obtained by inversion. For this comparison the CMT source mechanism was also used but the focal depth was reduced to 12 km. (c) Comparison of the starting S-wave velocity model (dashed line) and the S-wave inversion model (solid line). Qualitative bounds on our inversion model derived from the test discussed in Appendix B are shown as dotted lines.

Figure 8. Vertical component short-period and three component long-period P-wave seismograms for Event 2.

Figure 9. (a) Comparison of long-period P-waveform of Event 2 (solid line) with reflectivity synthetic seismograms computed for the inversion (dashed line), and for the final (dotted line) velocity models. The P_1 waveform which is primarily controlled by the crustal structure is equally well fit by synthetics waveforms for both models. However, the amplitude of the first arrival is better fit by the synthetic computed for the final model. (b) Comparison of long period seismograms for Event 2 with whole wavefield reflectivity synthetic seismograms for the final earth model. (c) Earth model from surface wave inversion (dotted lines) and final earth model (solid line) from forward modeling P_{n_l} waveforms for this Event 2. The shear wave velocity model remained fixed during this stage of the analysis. The P- and S-wave velocity is in km s^{-1} and the density is in gm cm^{-3} .

Figure 10. Average earth model (solid lines) for southern Africa determined by computing the mean and standard deviation of the velocities and density at each depth for the twelve path-average earth models. The dotted lines denote the range of velocity models from analysis of the individual source-receiver paths. The solid circles denote velocity and density estimates from geochemical analysis of the garnet peridotite nodules from kimberlites on the Kaapvaal Craton. The x-axis scale is in km s^{-1} for the P- and S-wave velocities and gm cm^{-3} for the density.

Figure 11. Southern African velocity model from this study (solid line) compared with previous models for southern Africa: (a) shear wave model of Bloch *et al.* (1969) (dotted line), compressional wave model of Clouser & Langston (1990) (dotted line), compressional wave model of Green (1978) (short dashed line); (b) shear wave models of Cichowicz & Green (1992) (short dashed line, $n=3$; long dashed lines, $n=6$; dash-dot line, $n=11$).

Figure 12. Comparison of the fundamental and higher mode Love (a) and Rayleigh (b) wave group velocity data and fundamental mode Rayleigh (b) wave phase velocity data from Bloch *et al.* (1969) (dotted line), and dispersion curves (solid lines) computed for the velocity and density model of Figure 10 and Table 5.

Figure 13. Comparison of Event 2 long-period seismograms (solid line) with reflectivity synthetics computed for the upper mantle shear wave models for the Kaapvaal Craton from Cichowicz & Green (1992) $n=6$ (dotted). This fit should be compared with the fit of the reflectivity synthetic seismograms computed for the final earth model (Table 4) for this event shown in Figure 9.

Figure 14. (a) Comparison of observed vertical component waveforms (solid lines) for the July 18, 1986 earthquake (Event 2, Table 1) recorded at SLR with synthetic waveforms computed for the final earth model for this event (dashed line) and for the SACM06c P-wave model of Clouser & Langston (1990) (dotted line). (b) Same comparison as in (a) but for the seismogram for the March 9, 1989 earthquake (Event 4, Table 1) recorded at SLR. (c) Same comparison as in (a) but for the seismograms of the July 24, 1991 earthquake (Event 10, Table 1) recorded at SUR.

Figure 15. Southern African velocity model from this study (solid line) compared with velocity models for other cratonic regions: (i) Canadian shield (long dashed line) (LeFevre & Helmberger, 1989; Brune & Dorman, 1963), (ii) Australian shield (dotted line) (Bowman & Kennett, 1990; Kennett *et al.*, 1994), and (iii) the Baltic shield (short dashed line) (Given & Helmberger, 1980; Calcagnile, 1991).

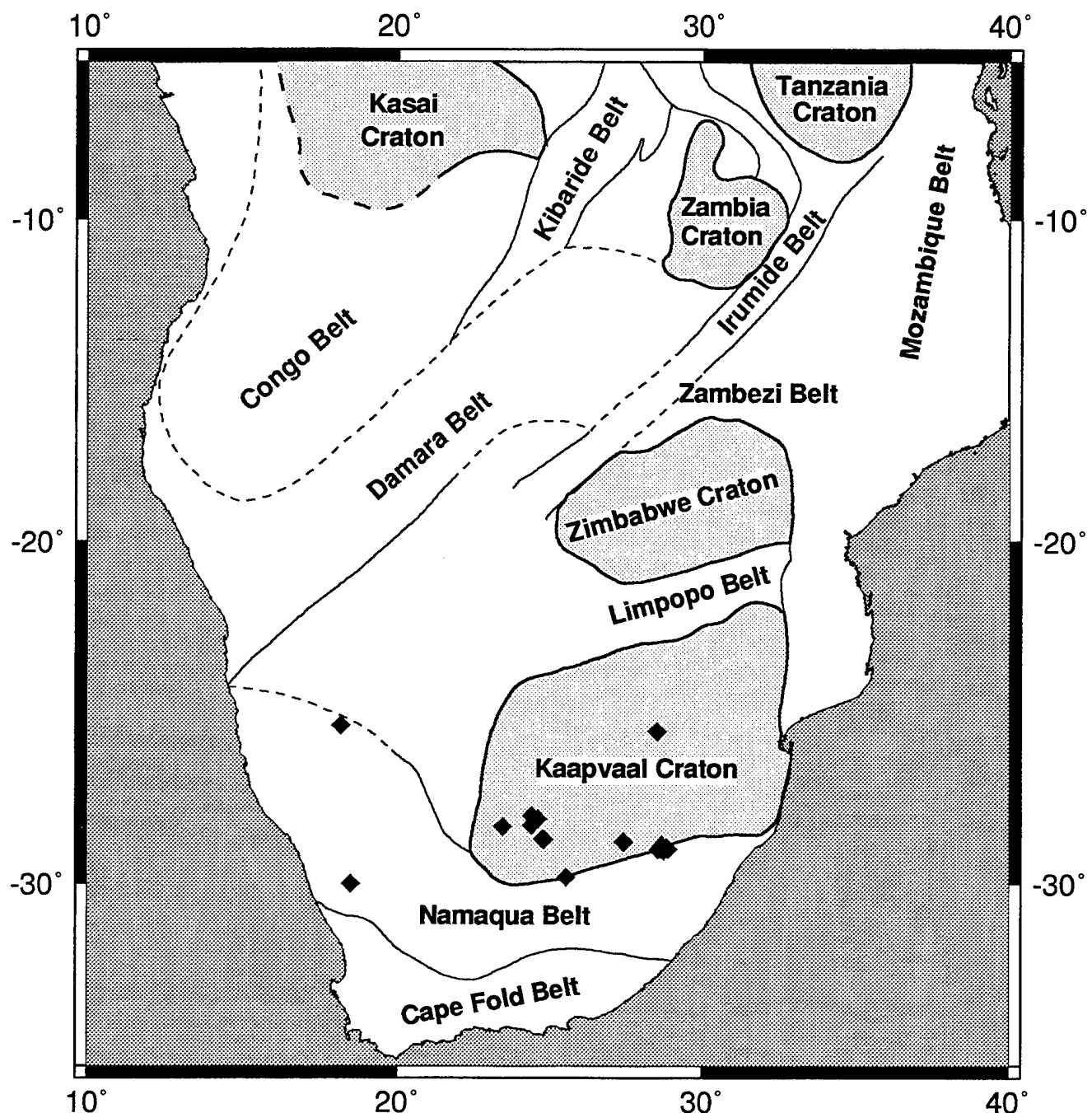


FIGURE 1

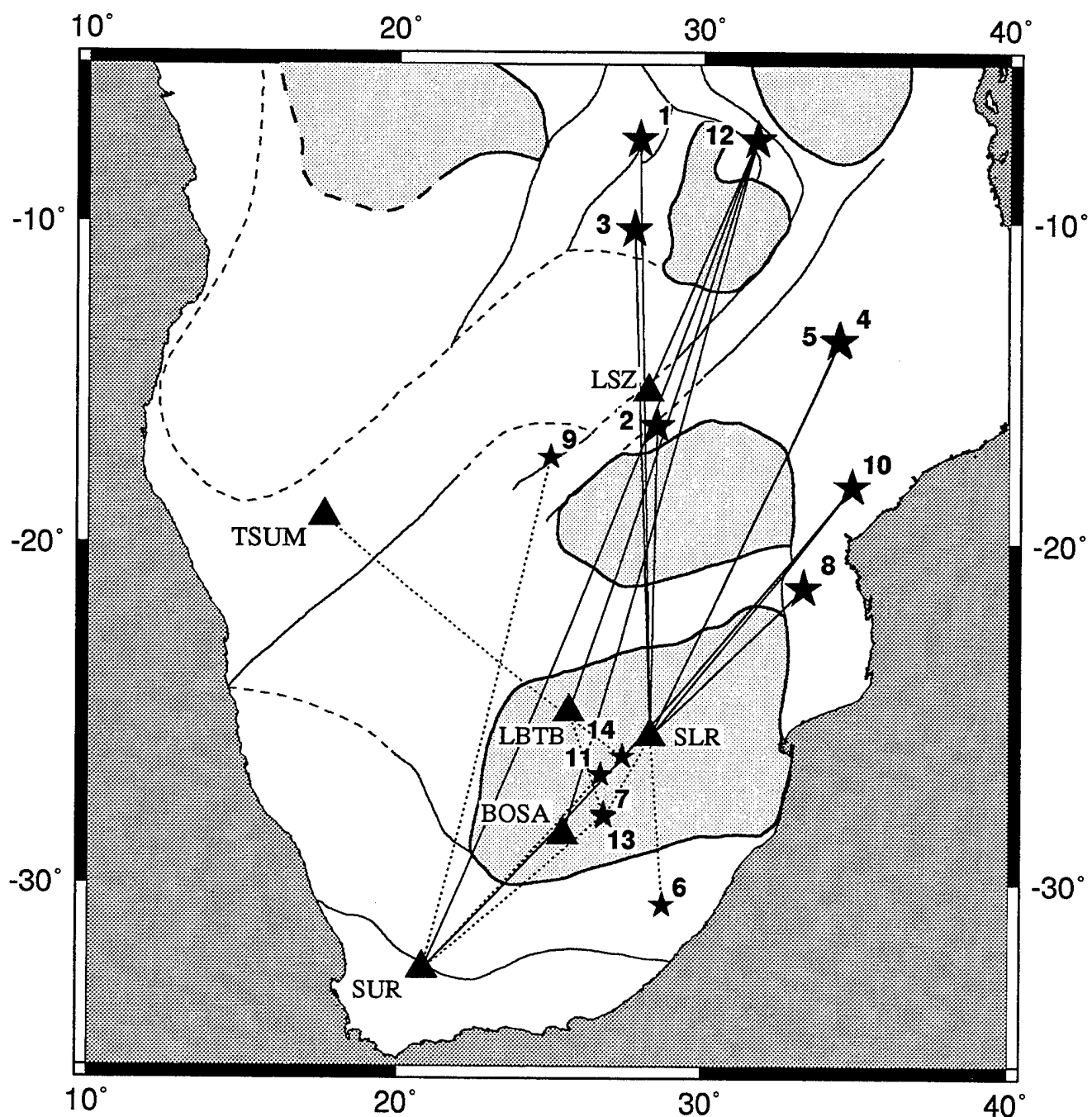


FIGURE 2

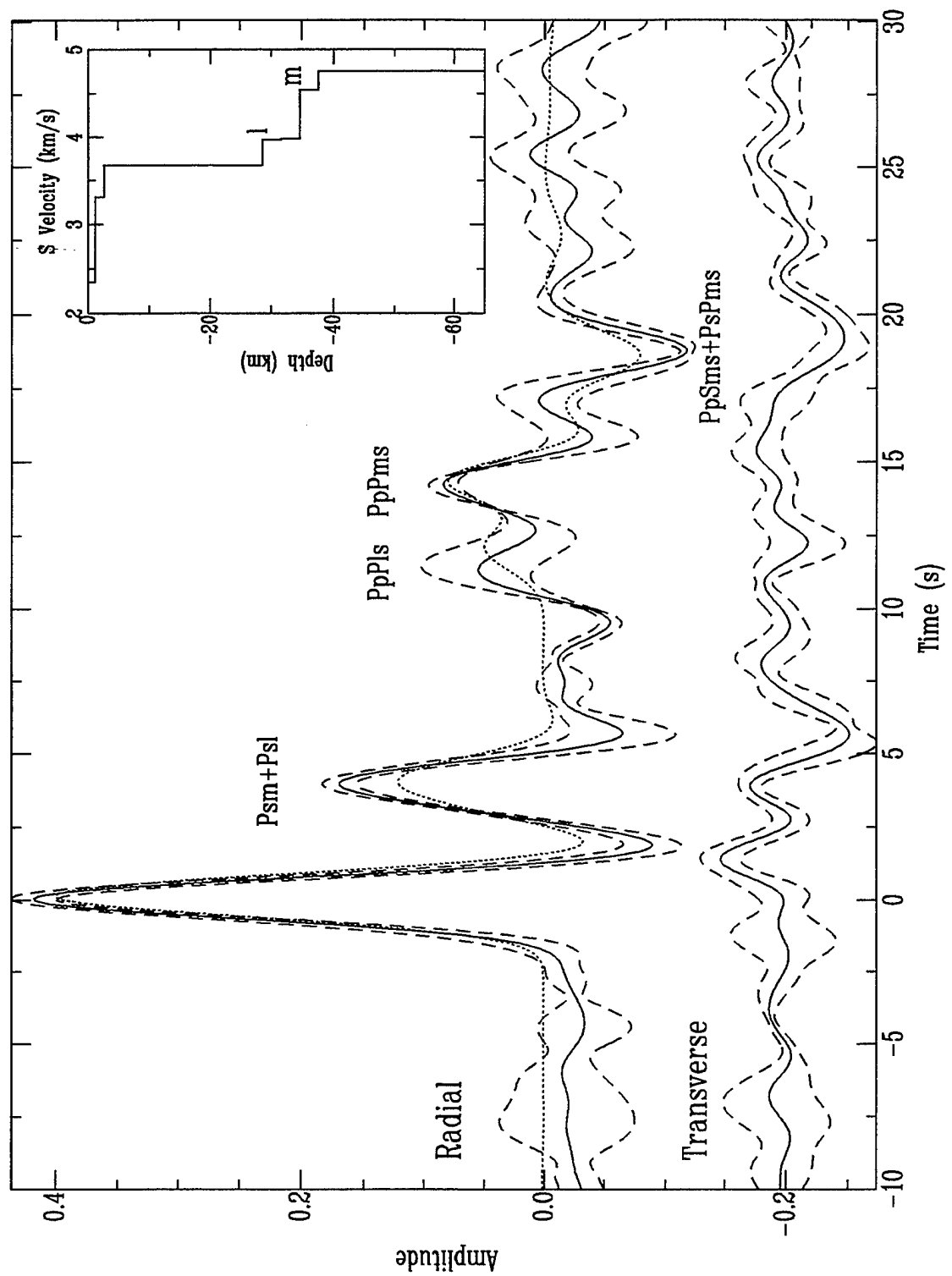


FIGURE 3

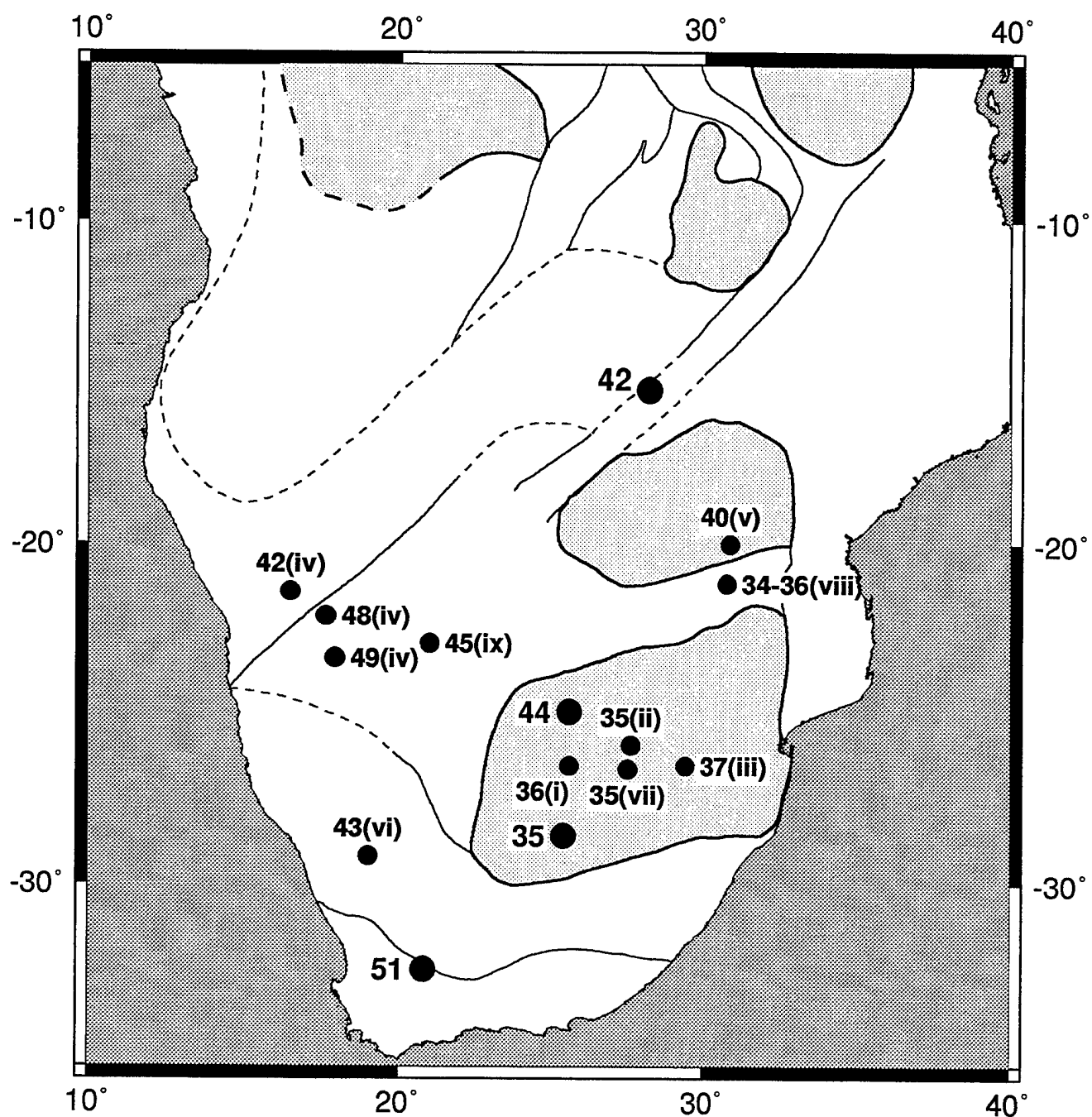


FIGURE 4

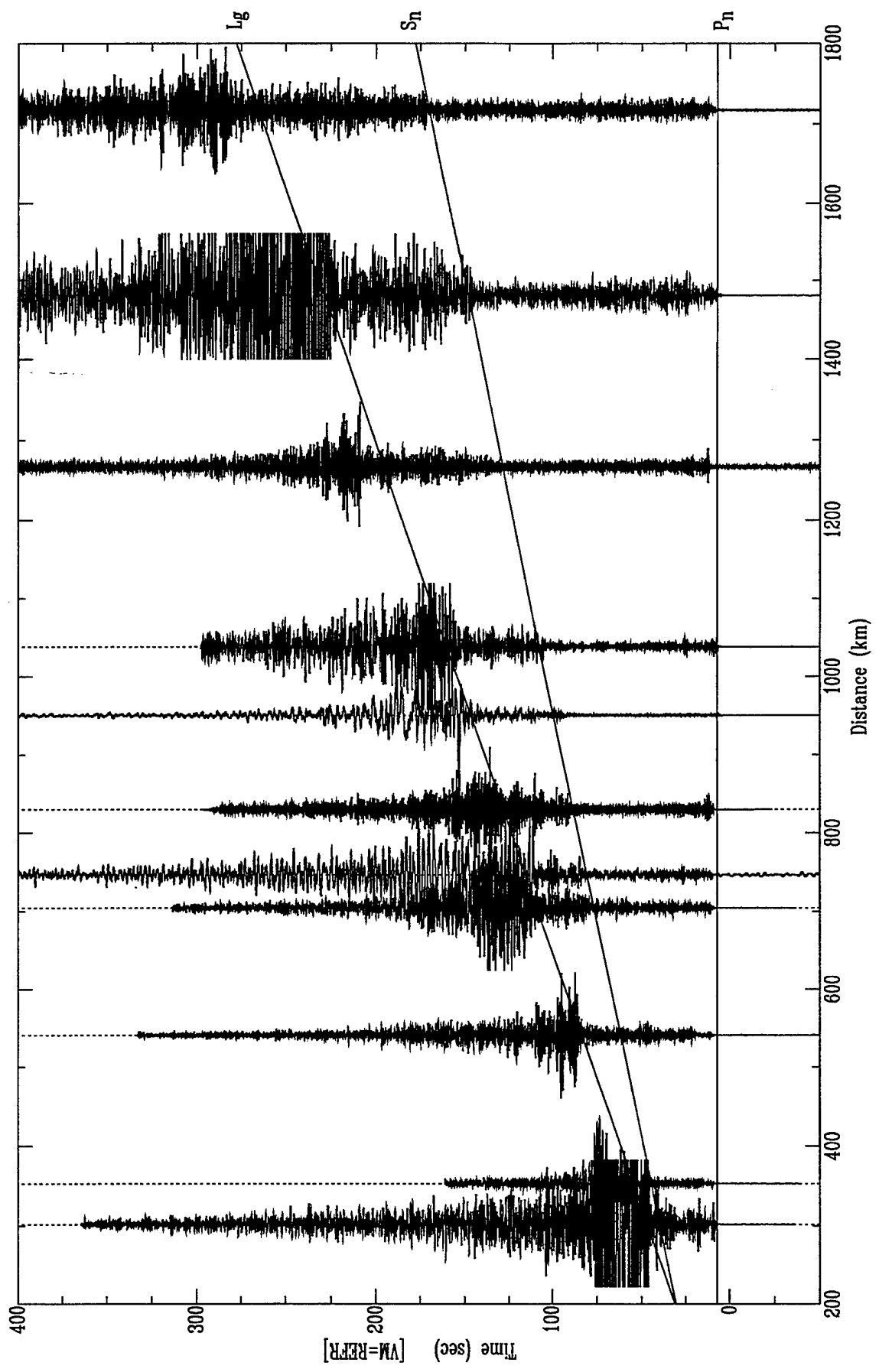


FIGURE 5

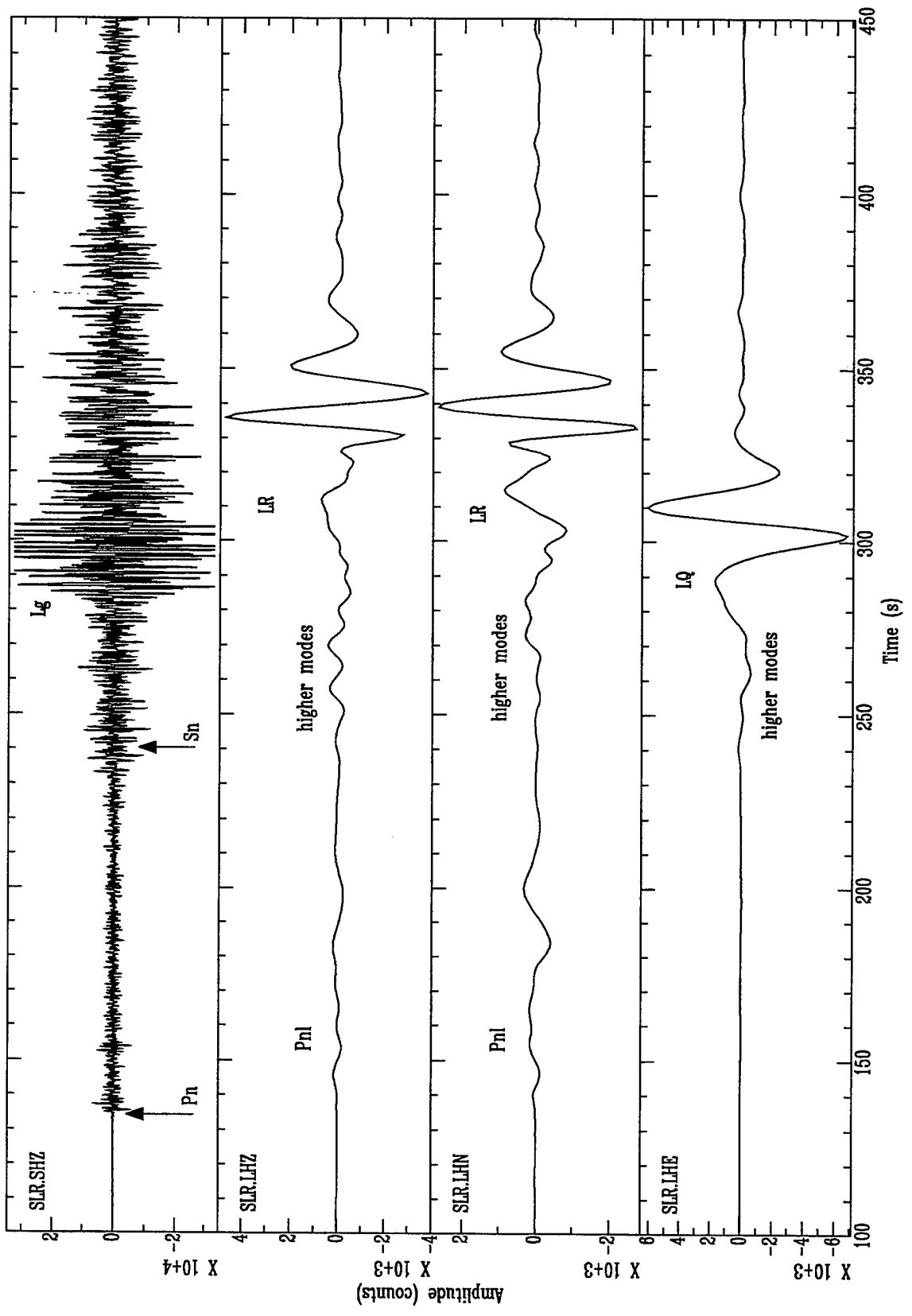


FIGURE 6

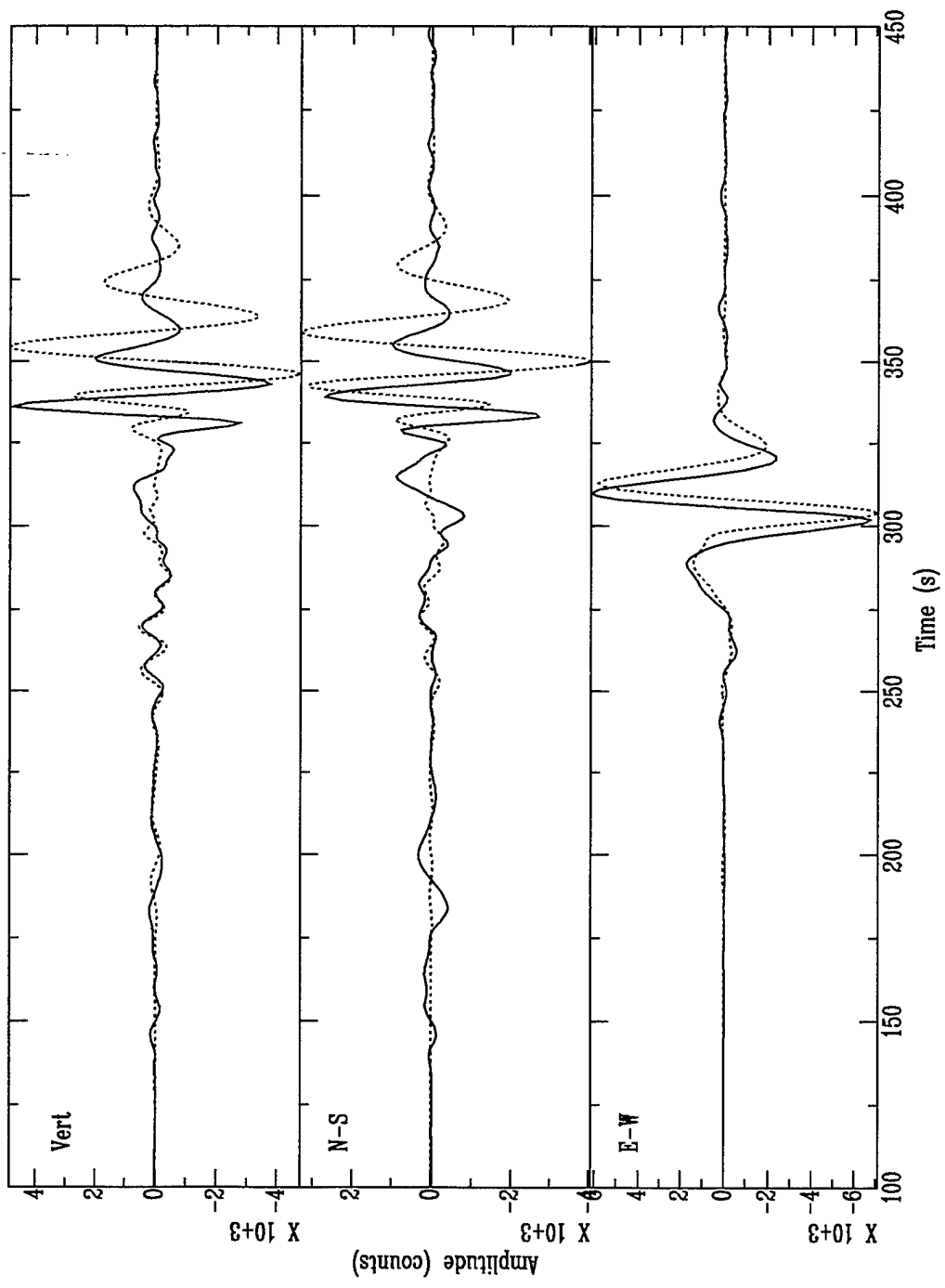


FIGURE 7a

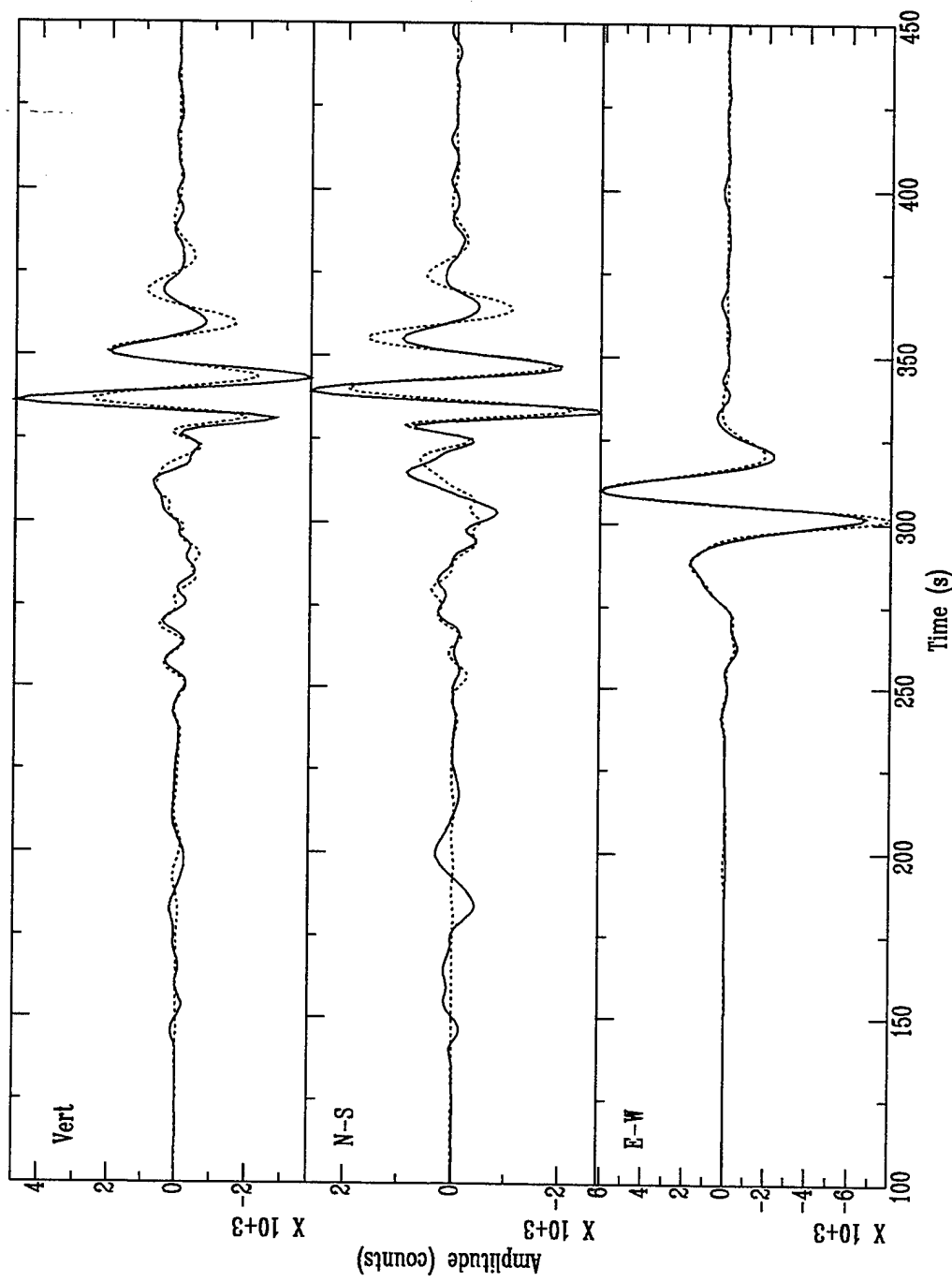
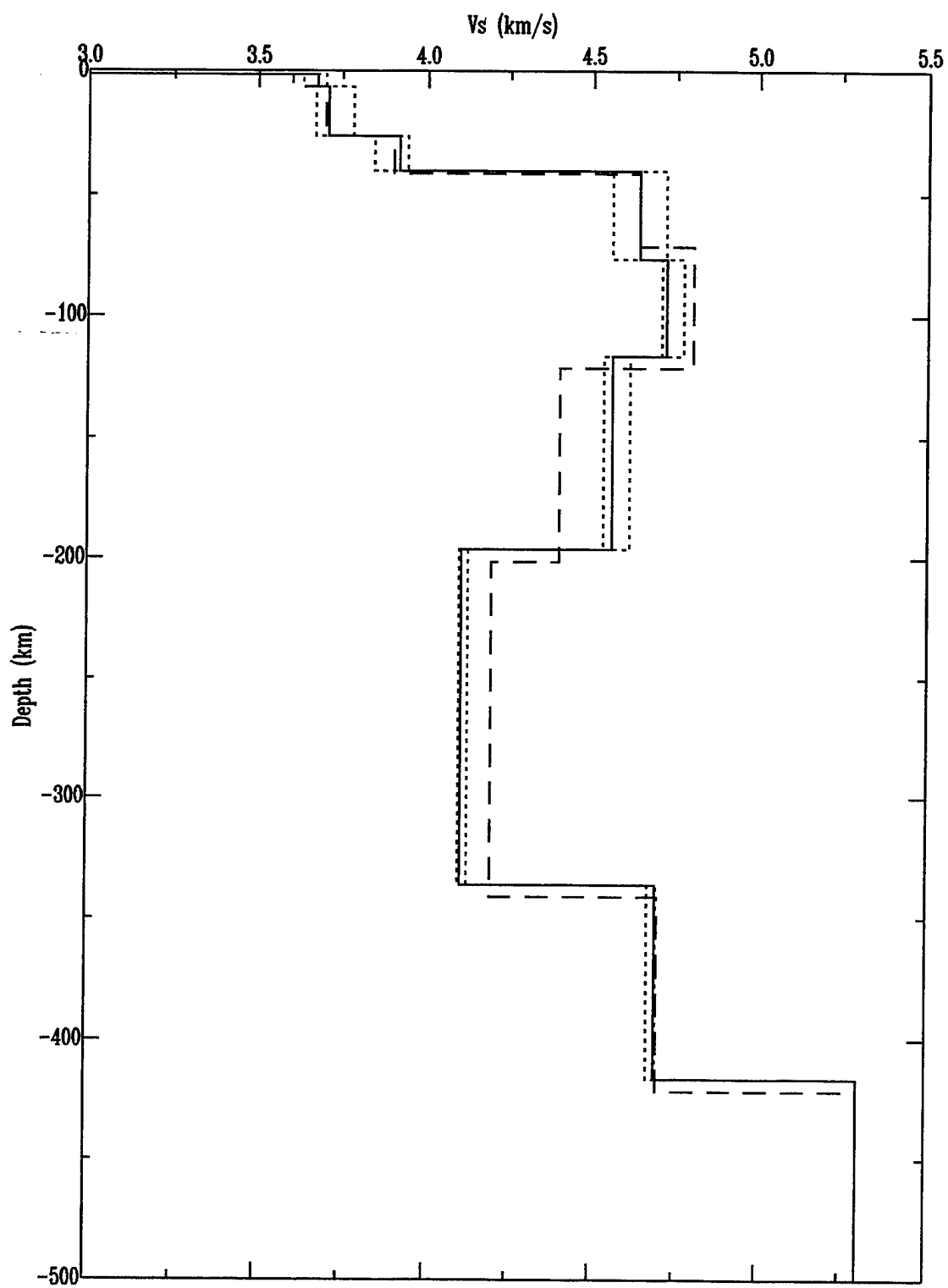


FIGURE 7b

FIGURE 7c



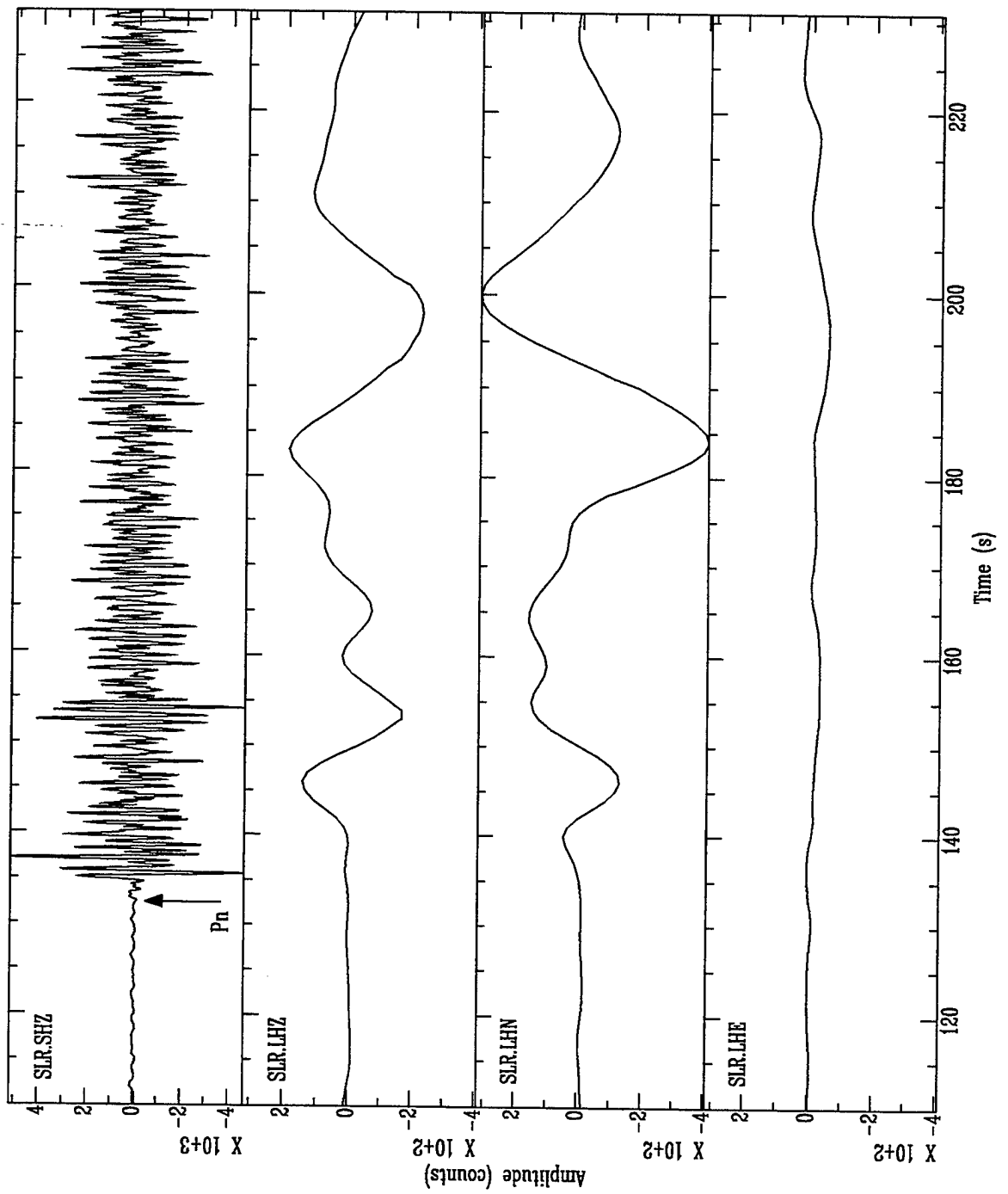


FIGURE 8

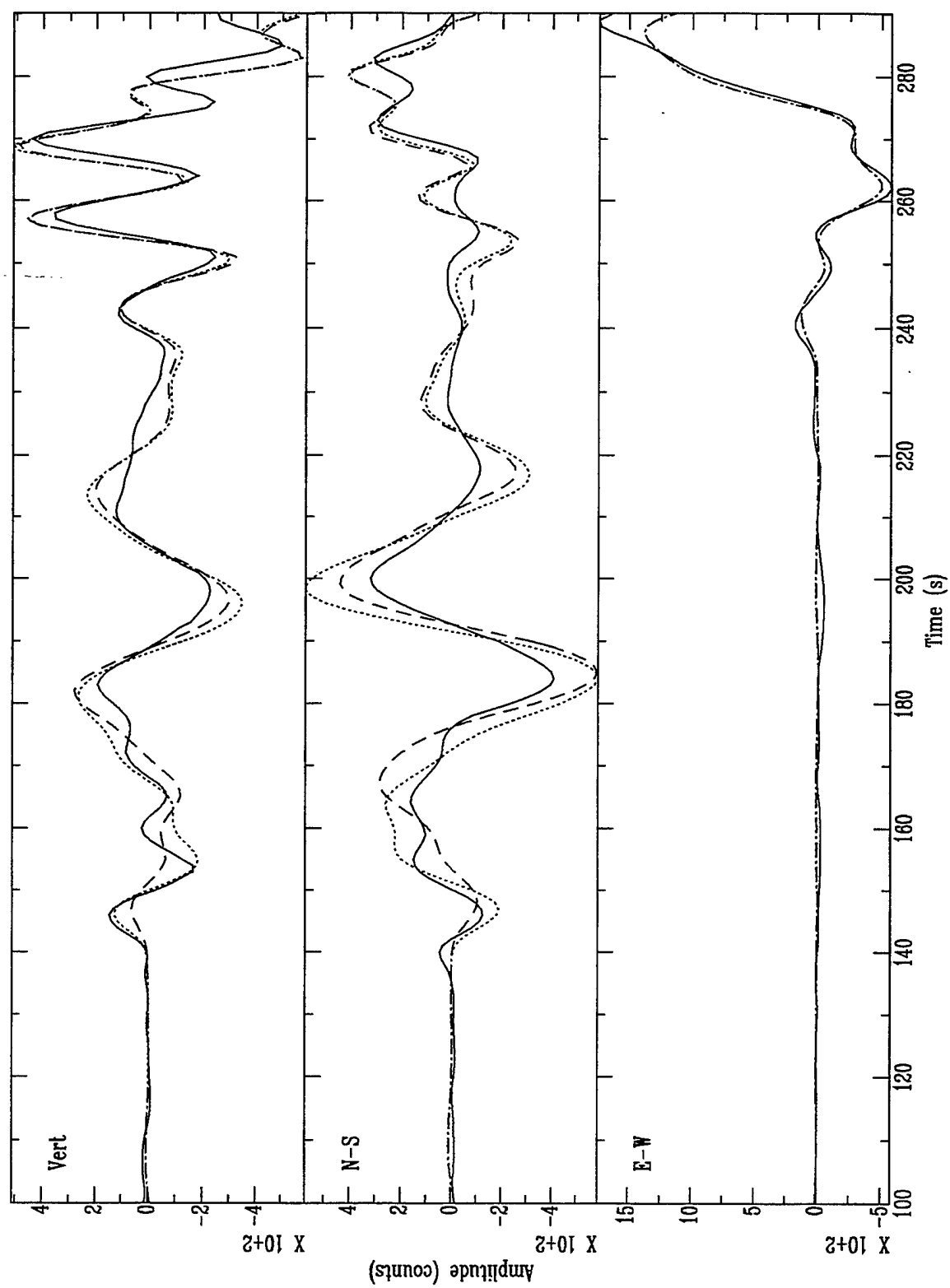


FIGURE 9a

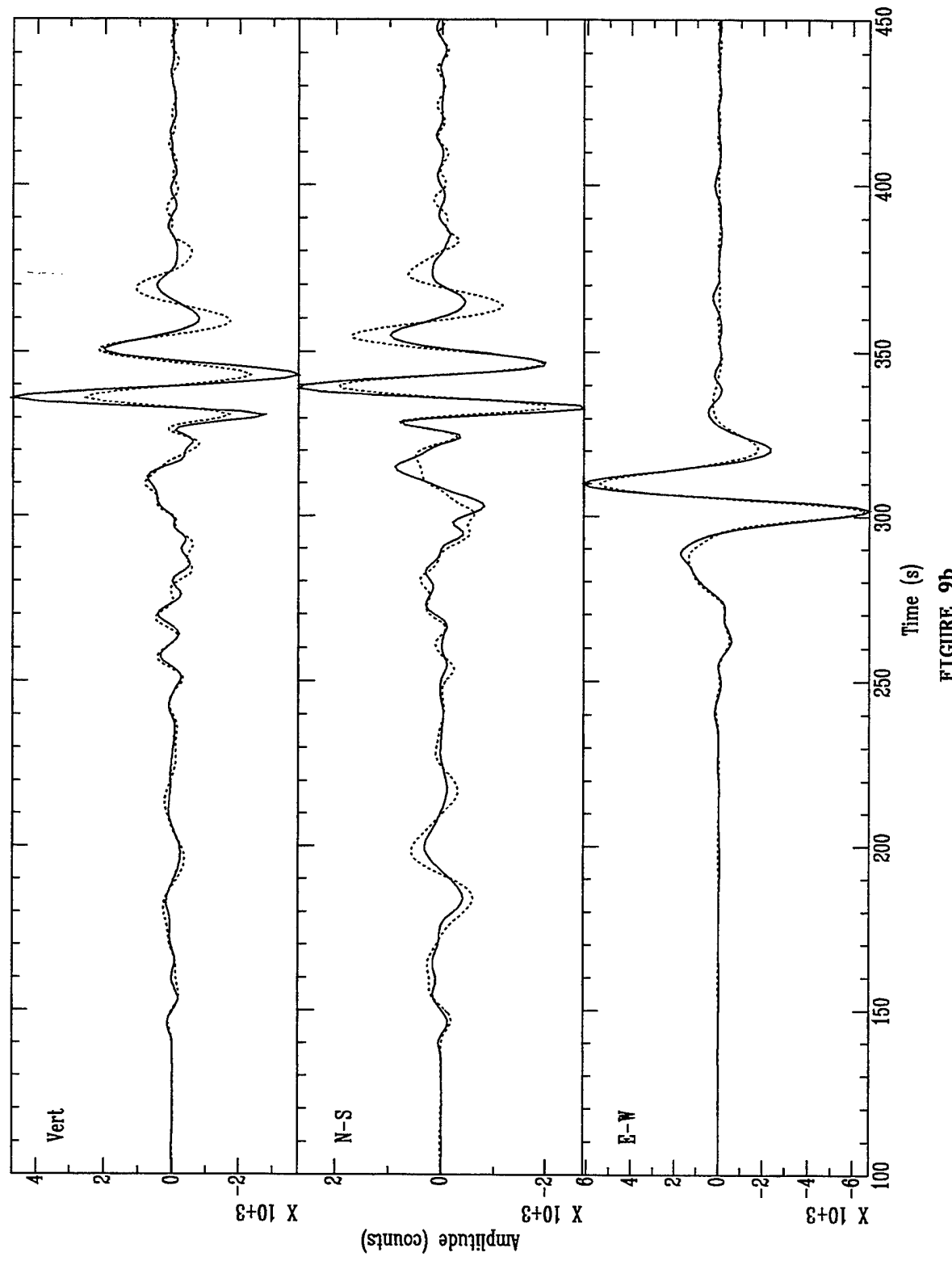
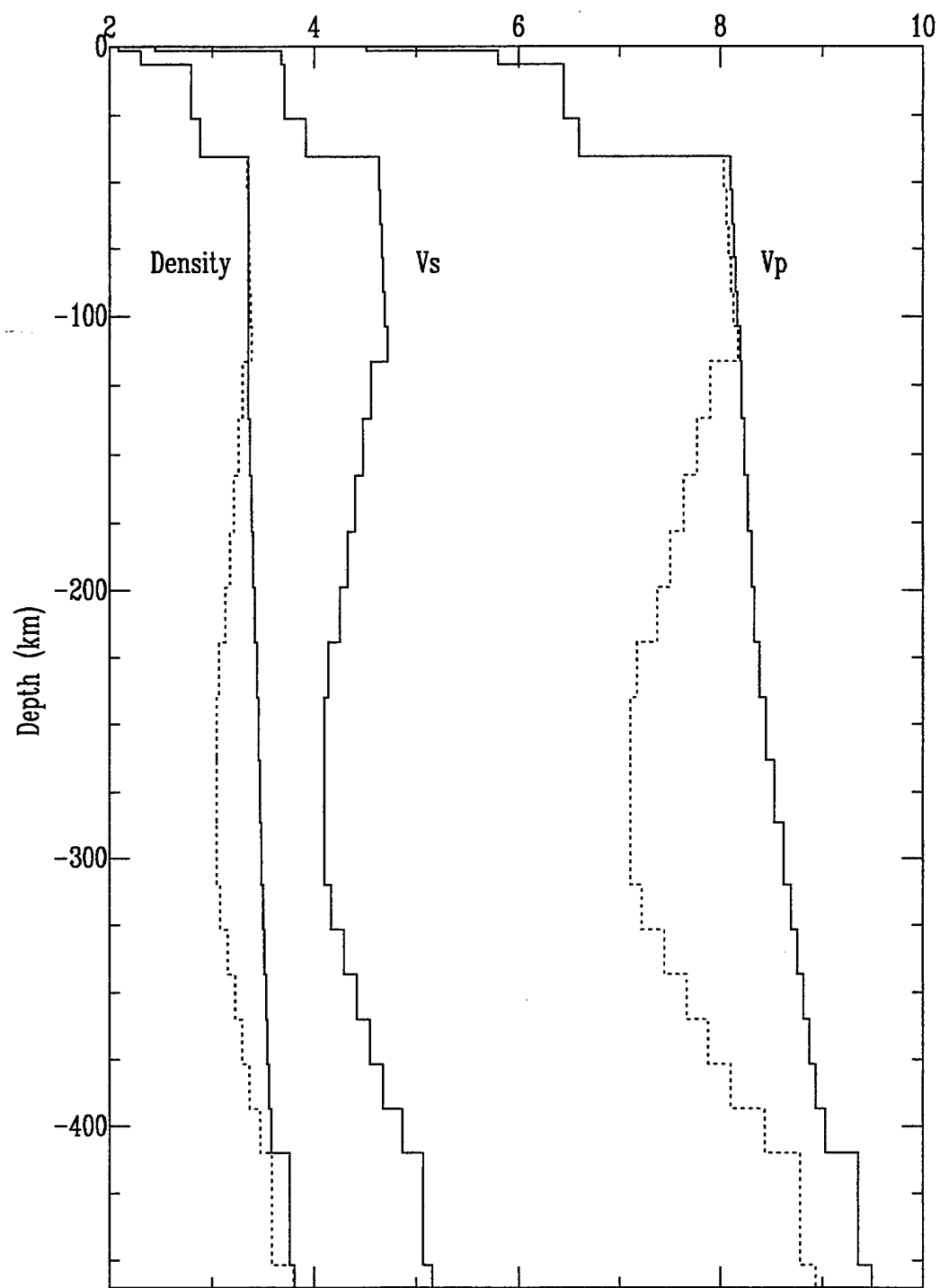


FIGURE 9b

FIGURE 9c



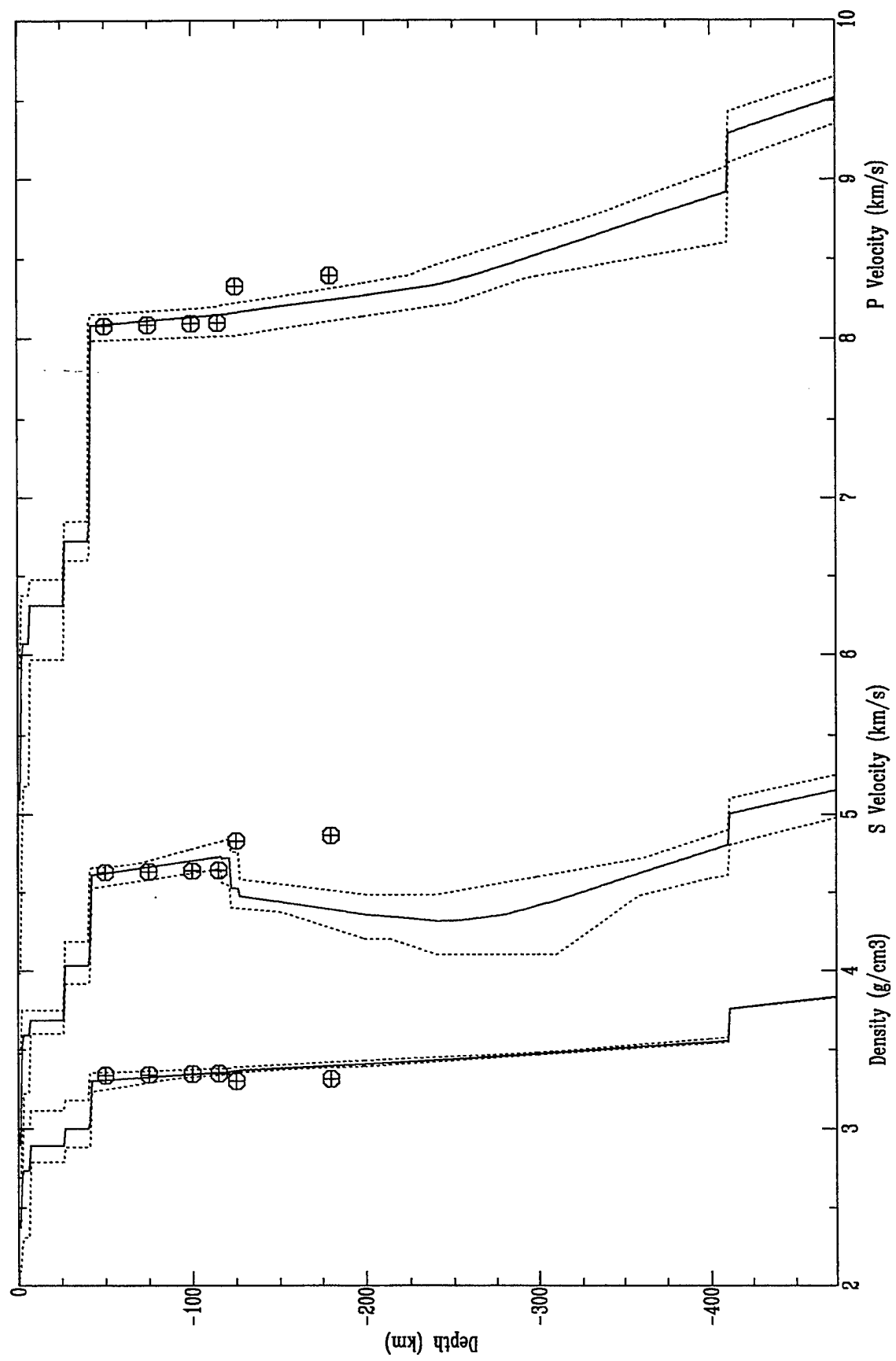


FIGURE 10

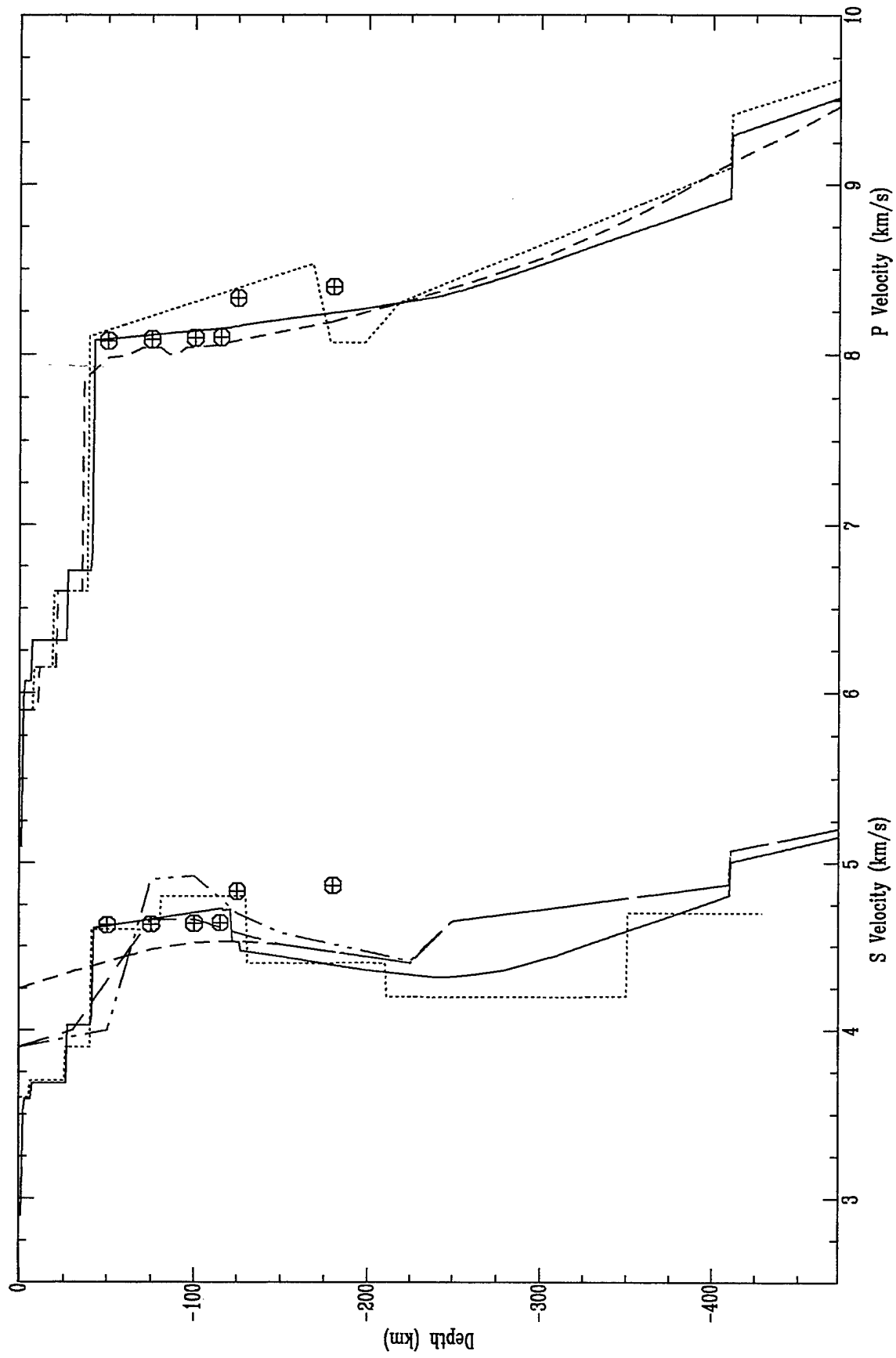
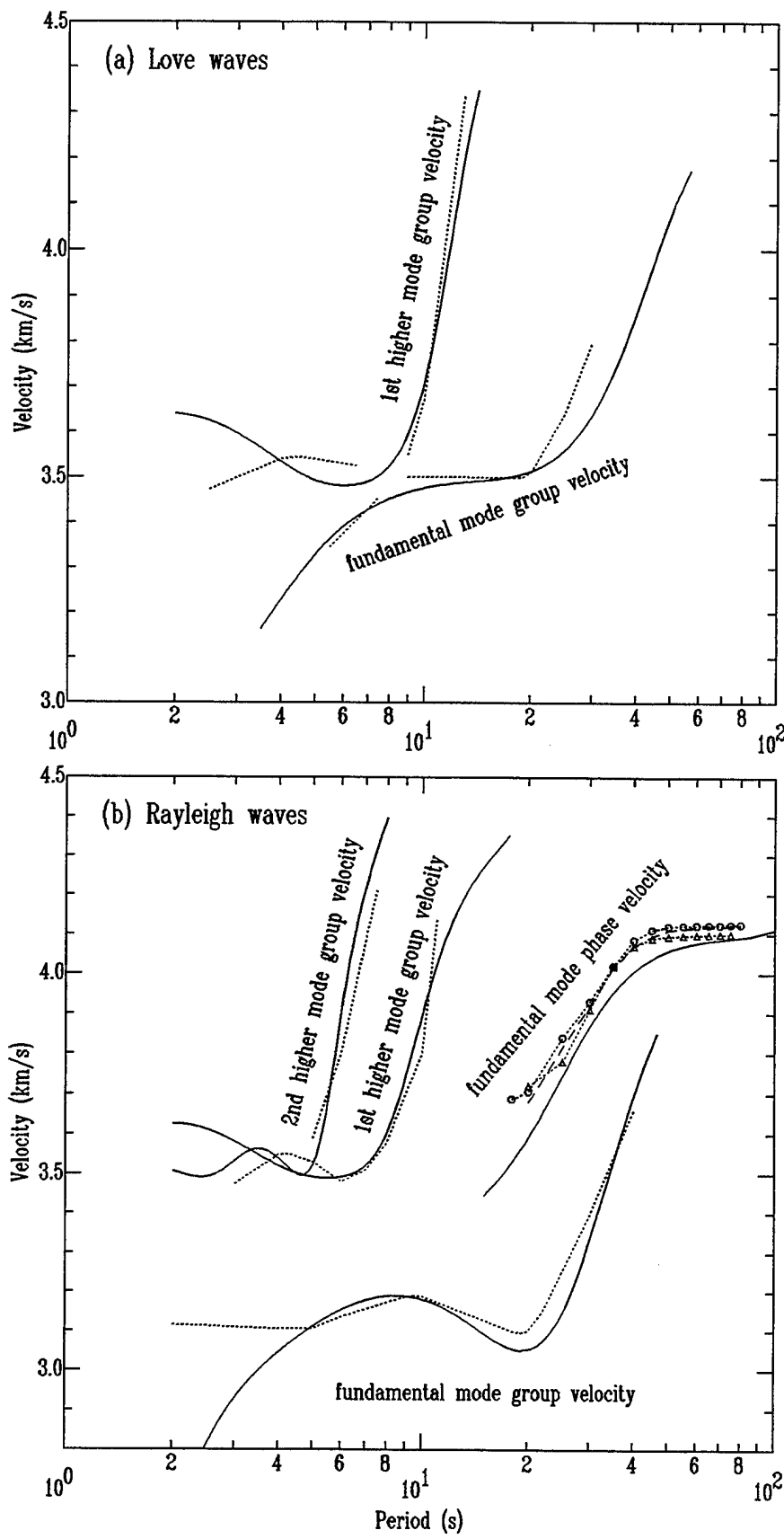


FIGURE 11

FIGURE 1.2



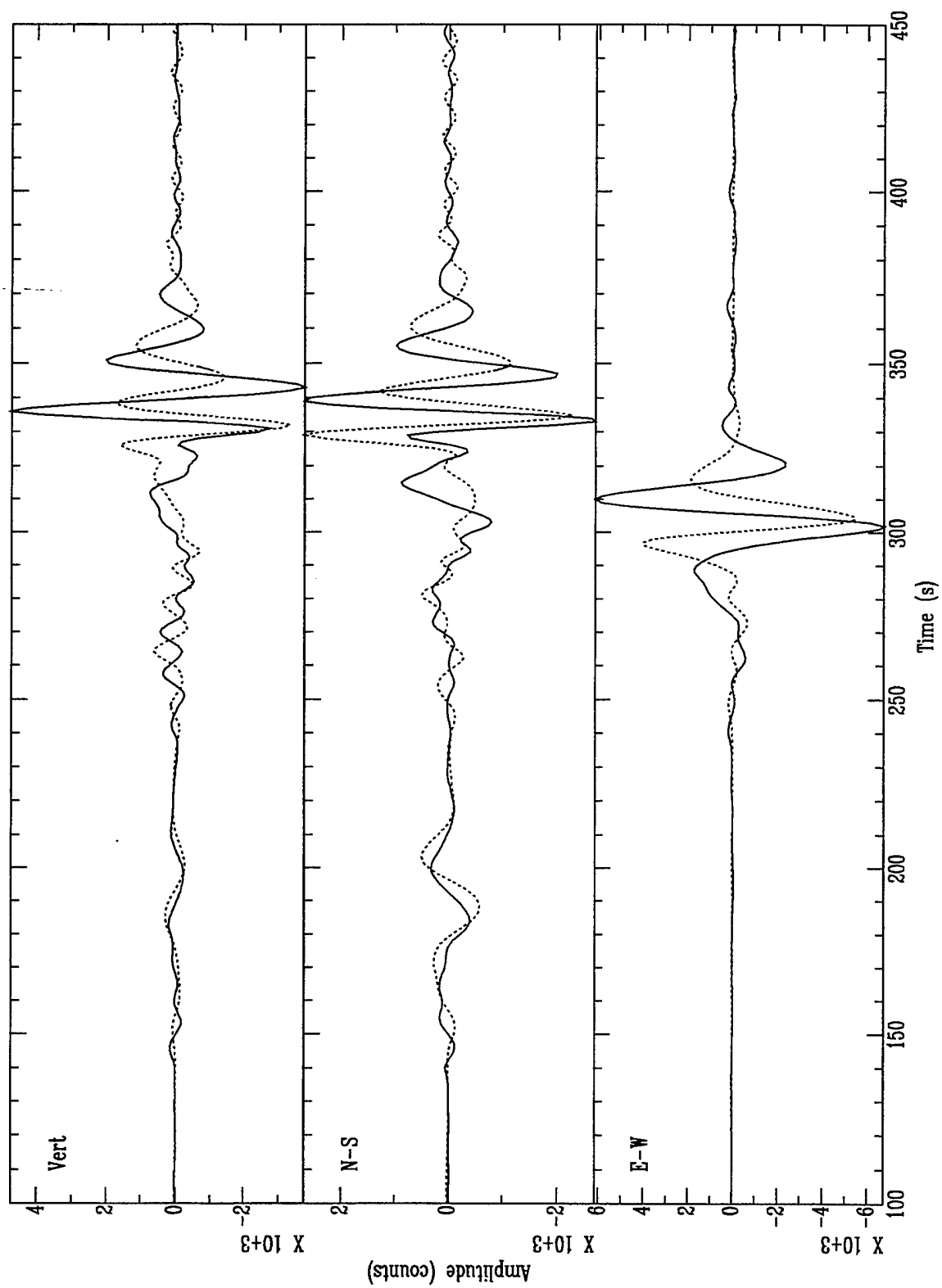


FIGURE 13

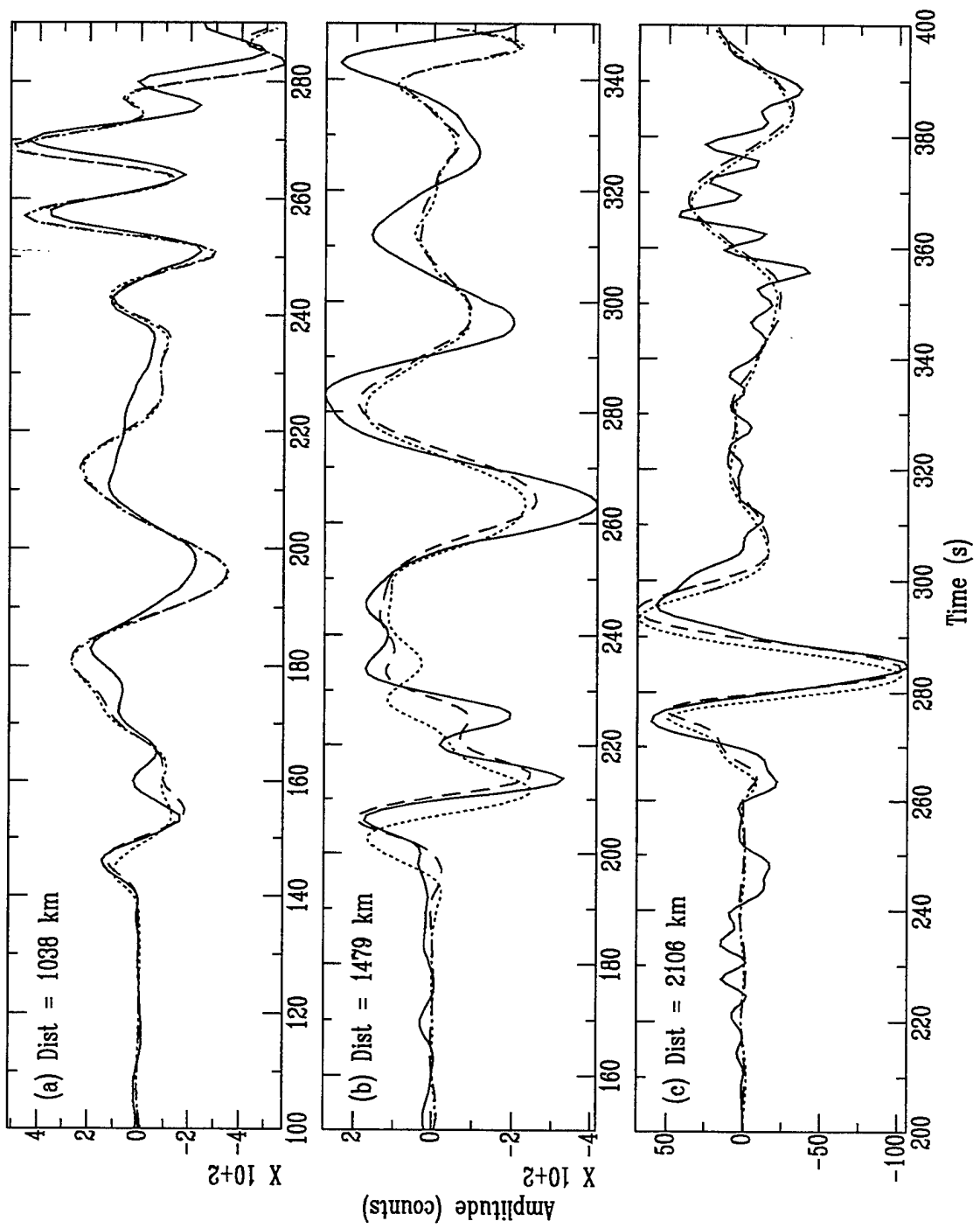


FIGURE 14

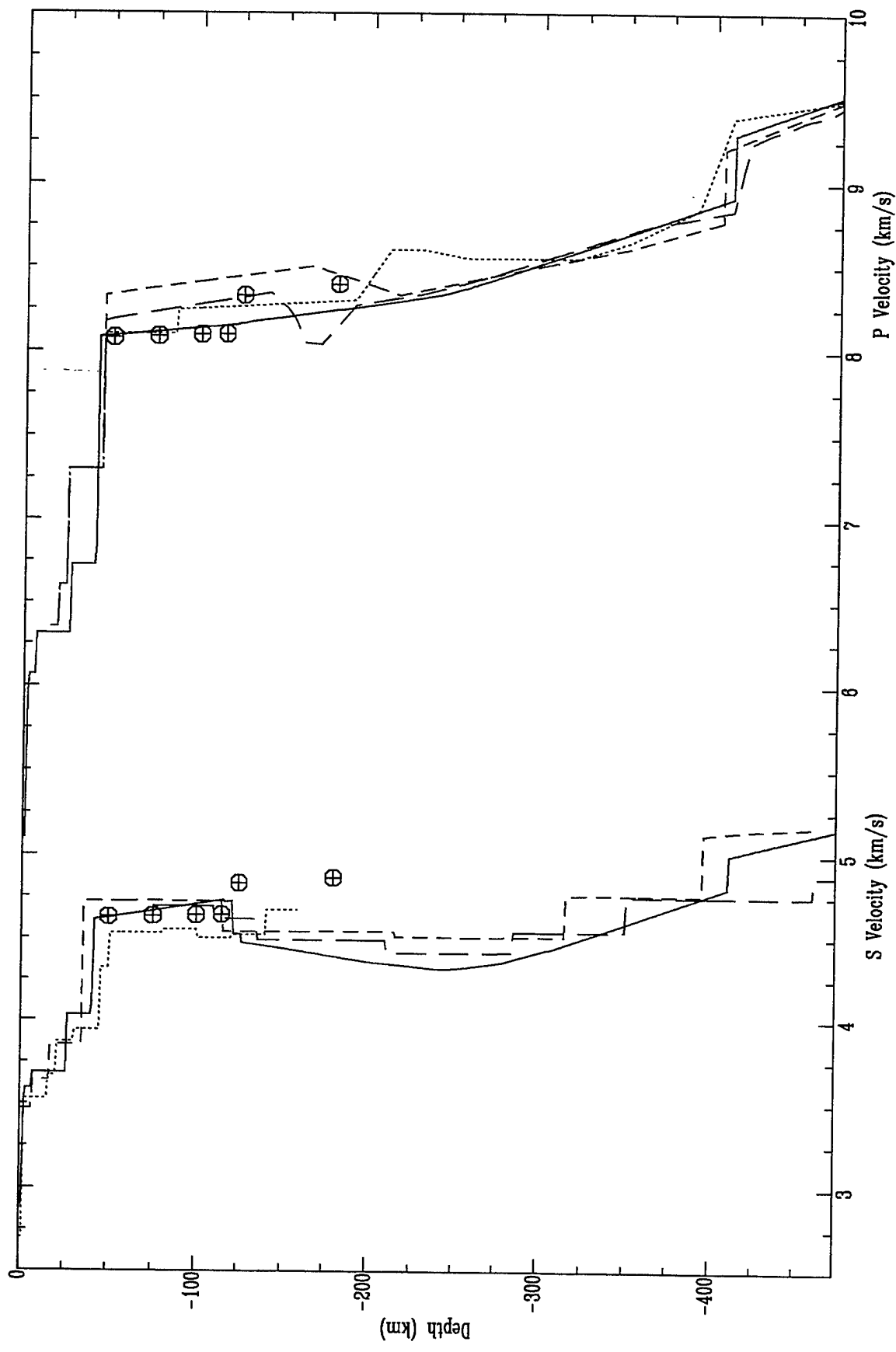


FIGURE 15

APPENDIX A Teleseismic Receiver Function Analysis

Seismograms of teleseismic P-waves contain the combined effects of the earthquake source, propagation through the Earth, and the instrument response. To use these seismic phases to determine earth structure beneath a broadband seismograph, the effects of the crust and upper mantle, and the site response or receiver function, must be isolated from these other factors. We have computed radial and tangential receiver functions by computing the spectral ratio of the radial or tangential component spectrum and the vertical component spectrum (Langston, 1979; Ammon, 1991). The deconvolution is stabilized by specifying a minimum spectral trough fill c for the vertical spectrum to avoid noise generated by dividing by small values. The resulting receiver function is smoothed by a Gaussian, a , which limits the high frequency content. All deconvolutions in this study were computed for $c = 0.001$ and $a = 1.0$ which were found to produce the most stable set of deconvolutions for the whole P-wave data set. This Gaussian limits the frequency content of the receiver functions to frequencies below about 0.4 Hz, resulting in reduced resolution of crustal velocity features. However, these low frequency receiver functions are able to resolve the main crustal features for comparison with the seismic refraction results where they exist, and provide a gross crustal structure estimate where seismic refraction results do not exist. The spectral ratio is then transformed back into the time domain giving a time display of the P-to-S conversions caused by the velocity impedance contrast beneath the site.

Figure A1 shows single event and stacked receiver functions for BOSA. The individual radial receiver functions are dominated by a large amplitude arrival 4 s after direct P. There are two smaller amplitude arrivals in each of the individual radial receiver functions; a positive arrival ~ 14 seconds after direct P and a negative arrival ~ 18 seconds after direct P. We have stacked individual receiver functions for events occurring over a small range of ray parameter and azimuth and computed the one-standard deviation bounds. The 4, 14, and 18 second arrivals in the stacked radial receiver function are large compared with the amplitude of the stacked tangential receiver function at the same times. However there are coherent tangential arrivals at 6 and 19 seconds which may possibly interfere with these arrivals. If we interpret the 4 second phase as a P-to-S conversion at the Moho (Ps) and assume an average crustal P-wave velocity of 6.4 km s^{-1} and a Poisson's ratio of 0.25, the time of this arrival suggests a 35 km thick crust beneath BOSA.

The stacked radial receiver function was first forward modeled using a simple single layer crust over a half-space model based on the seismic refraction derived P-wave crustal model of Durrheim & Green (1992) with shear wave velocities assuming a Poisson's ratio of 0.25, and densities assuming the relationship $\rho = 0.77 + 0.32V_p$. Once the major features of the receiver function were matched by this simple modeling, the stacked radial receiver function was inverted using a time domain, linearized inversion procedure (Ammon *et al.*, 1990) using a more complex starting earth model based the Durrheim & Green (1992) model. The starting model was parameterized as a stack of 1 to 3 km thick layers to a depth of 70 km. This model was randomly perturbed into 24 different starting models and the radial receiver function inverted for a 1-D velocity model of the receiver structure by minimizing the difference between the observed radial receiver function and a synthetic predicted for the structure. This pseudo-Monte Carlo approach enabled us to reduce the dependence of the convergence of the inversion model on the form of the starting model. Once the depths of the significant seismic impedance contrast were identified, the initial model was reparameterized with thicker layers and the radial receiver function re-inverted. Using this approach we have determined a crustal model beneath each station with the minimum number of layers which give a satisfactory fit to the data. Since the receiver function consists of few events, we concentrated on fitting the early part of the data and did not emphasize fitting later arrivals. The results for BOSA are shown in Figure 3 and discussed in the main text. Discussion of the receiver function analysis for the other sites is found in the

captions to Figures A2–5. The format for these figures is the same as that of Figure 3.

We would like to re-emphasize that the purpose of analyzing the receiver function data was not to produce definitive models of the crustal velocity structure beneath the four stations but to provide some control on the gross crustal structure (average velocity and Moho depth) to use in the modeling of the regional waveforms.

APPENDIX A – FIGURE CAPTIONS

Figure A1. Teleseismic receiver functions for BOSA from four deep earthquakes in South America ($\Delta = 79^\circ \pm 3^\circ$, backazimuth = $244^\circ \pm 5^\circ$). The four upper panels are individual receiver functions and the two bottom panels are the stacked radial and transverse receiver functions. For the individual receiver functions the solid line denotes the radial and the dotted line denotes the transverse; for the stack receiver function the solid line denotes the receiver function and the dotted line denotes the $\pm 1\sigma$ bounds.

Figure A2. This figure and Figures A3–5 are all in the same format as Figure 3. The LBTB receiver function consists of a stack of two events from the Hindu Kush region ($\Delta = 75^\circ \pm 1^\circ$, backazimuth = $37^\circ \pm 1^\circ$). The Psm arrival at LBTB follows the direct arrival by almost 5 seconds, about a second longer than the Ps – P time at BOSA. Assuming the same crustal velocities in this part of the craton, the LBTB Ps – P time difference implies a crust ~ 8 – 10 km thicker beneath LBTB than beneath BOSA. However there is a significant arrival at 6 seconds on the tangential, indicating an off–azimuth arrival. This may cause distortion in the Ps arrival. There is a second negative arrival at about 22 seconds which could be interpreted as the PpSms + PsPms phase. The inversion result shows a relatively high shear velocity in the surface layer and a nearly uniform 3.77 km s^{-1} crust between 4 and 34 km depth. The velocity increases to 3.95 km s^{-1} at 34 km depth and there is a sharp crust – mantle transition at 44 km depth where the velocity increases from 4.13 to 4.53 km s^{-1} . The synthetic receiver function for this velocity model fits the timing of the main features of the observed receiver function but the amplitudes are not well fit. The coherency is poor for PpPls and PpPms which may partially result from interference from off–azimuth energy arriving at the same time as indicated by the large coherent arrival on the tangential component between 12 and 18 seconds. The amplitude of this tangential arrival is much larger than the synthetic radial arrival at about the same time. The timing of the PpSms + PsPms synthetic and observed arrival agrees but there is a large discrepancy in amplitude. While the correlation between the observed and synthetic receiver function is not as good as we would like, the Ps–P time difference does suggest that the crust beneath this part of the craton is thicker than to the south beneath BOSA.

Figure A3. The SUR receiver function stack consists of three events from South America ($\Delta = 75^\circ \pm 6^\circ$, backazimuth = $253^\circ \pm 6^\circ$). The Psm arrival follows direct P by nearly 6 seconds indicating either a thicker crust or lower velocity crust compared to the region to the NE. There are no other clear phases in the radial receiver function. The velocity model deduced from this data consists of a nearly uniform crust below ~ 5 km depth, with a gradual velocity increase starting at about 35 km depth to mantle velocities below 51 km depth. The synthetic receiver function for this model provides a reasonably good fit to the main features of the observed data.

Figure A4. This SUR receiver function consists of a stack of two events from the South Sandwich Islands ($\Delta = 40^\circ \pm 1^\circ$, backazimuth = $219^\circ \pm 1^\circ$). The radial receiver function for this azimuth shows an oscillatory behavior which persists for 10 seconds following Ps. This is a common feature of both of the single event receiver functions comprising the stack but it is

not clear how these oscillations arise. Except for the coherent arrival at 8 seconds, there is little indication of off-azimuth arrivals which may contaminate the radial receiver function. The inversion results for the receiver function from this azimuth are similar to those from the South American azimuth at SUR except that the Moho in this model is at 53 km depth.

Figure A5. The receiver function for LSZ consists of a single event from South America($\Delta = 85^\circ$, backazimuth = 244°). The Psm arrival follows the direct arrival by 4 seconds. Later large arrivals on the radial component are questionable because of the large amplitude arrivals seen on the tangential component starting at about 7 seconds. The inversion result shows a crust with a strong gradient in the shallow crust, a uniform 3.63 km s^{-1} upper crust extending from 4 to 25 km depth, and a gradational lower crust with velocities increasing from 3.87 km s^{-1} at 25 km depth to 4.2 km s^{-1} at 40 km depth. The transition from lower crust to mantle velocities occurs over a 2 km transition. The synthetic Ps phase underestimates the amplitude of the observed Ps phase.

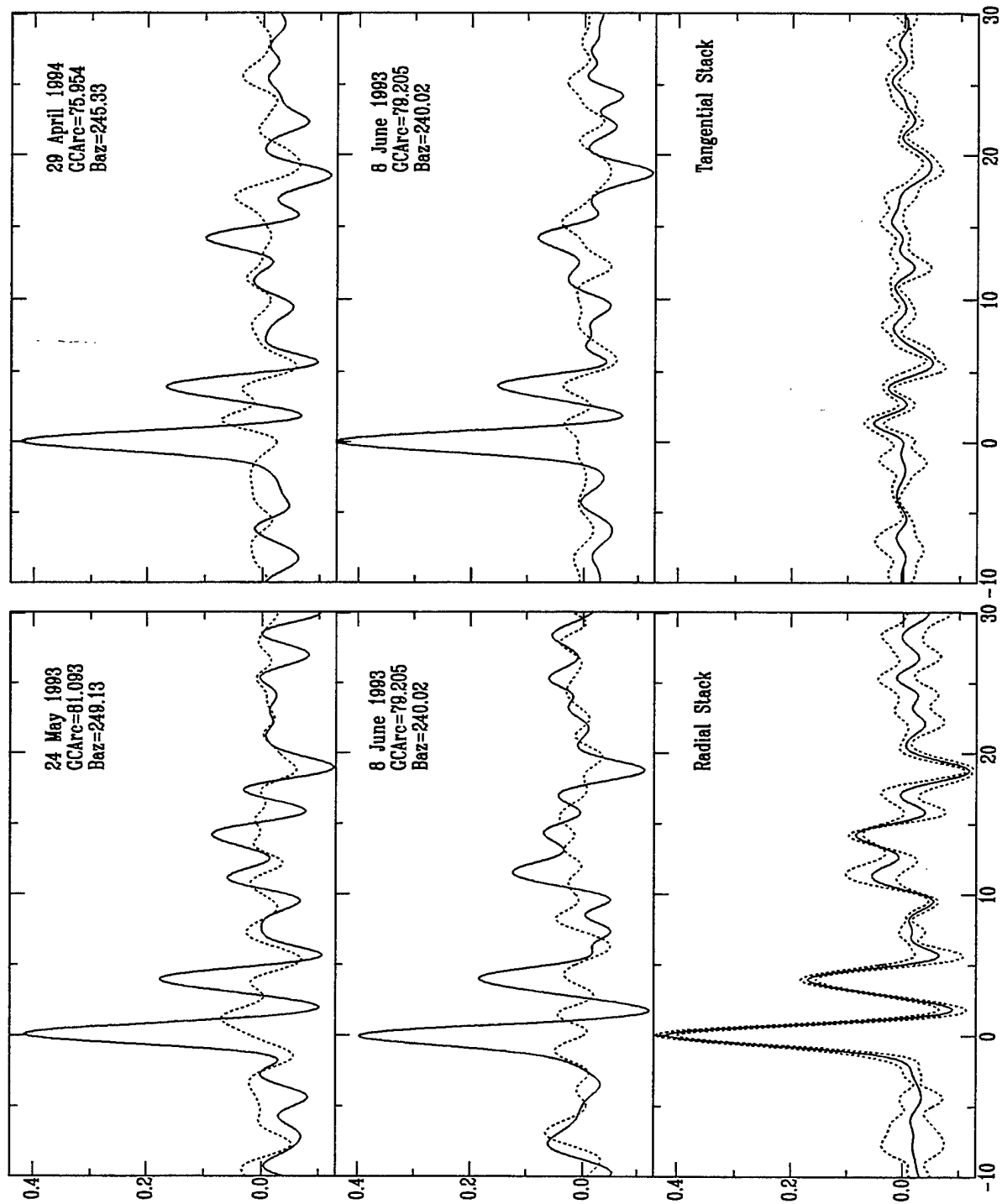


FIGURE A1

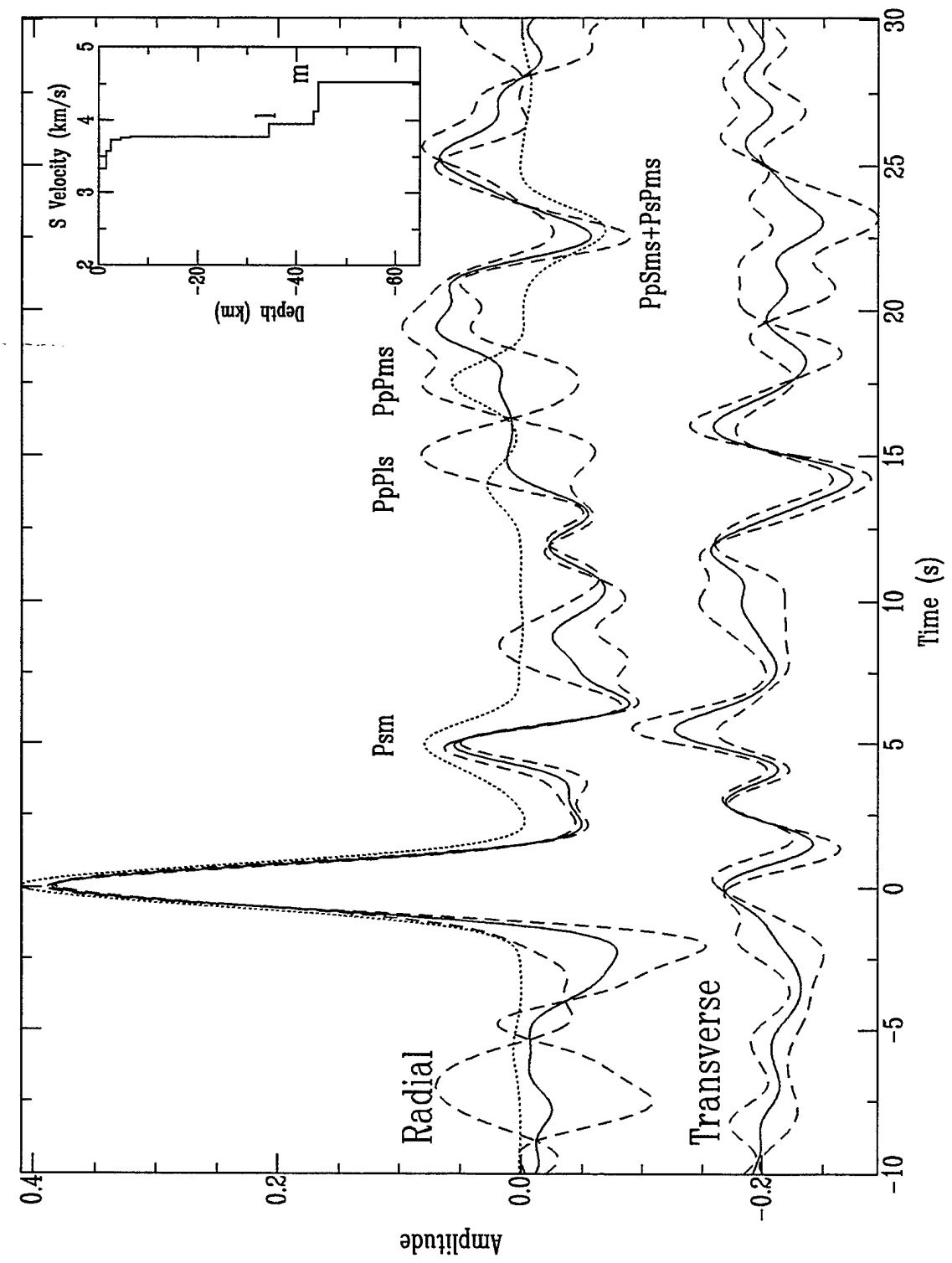


FIGURE A2

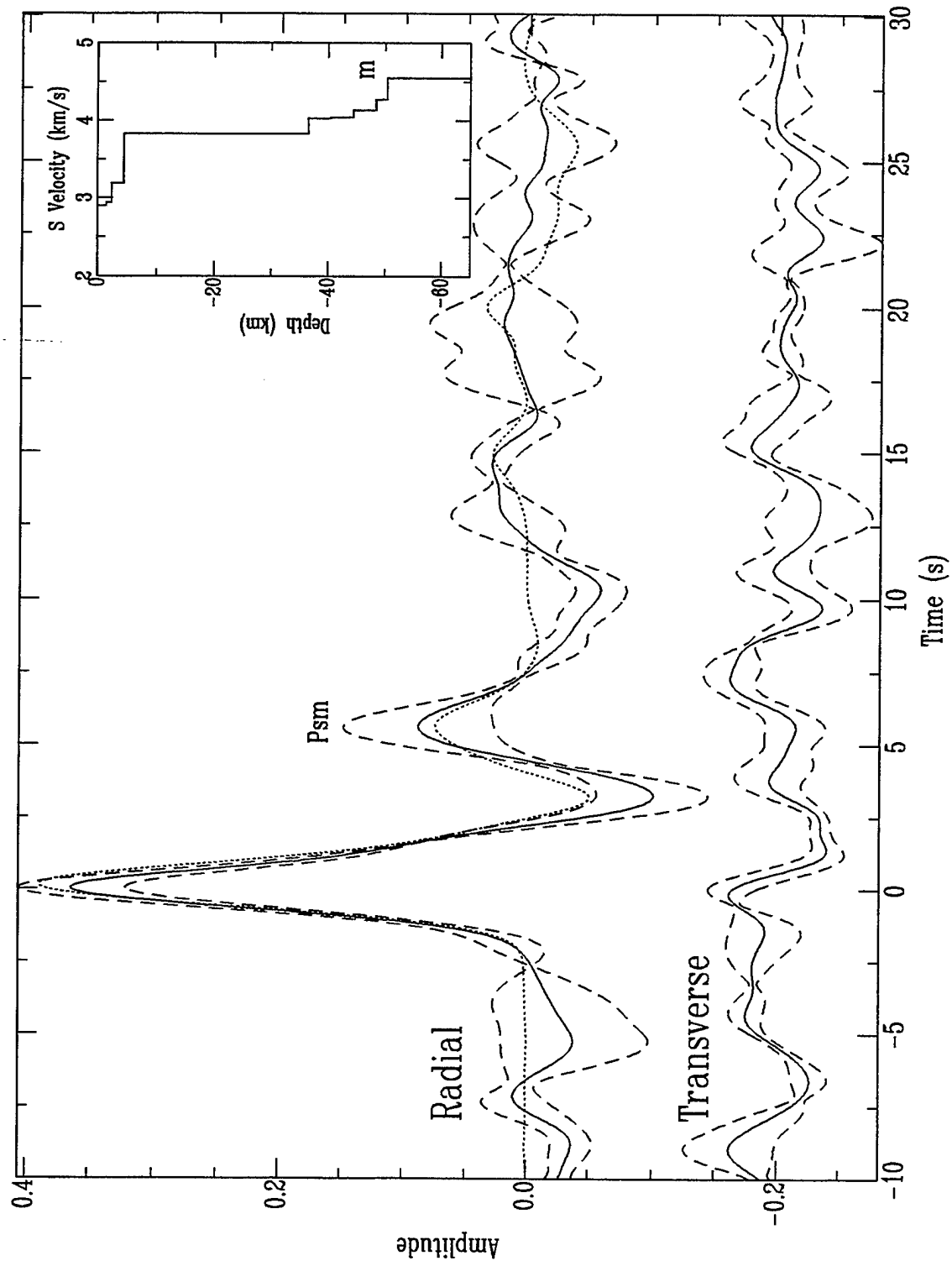


FIGURE A3

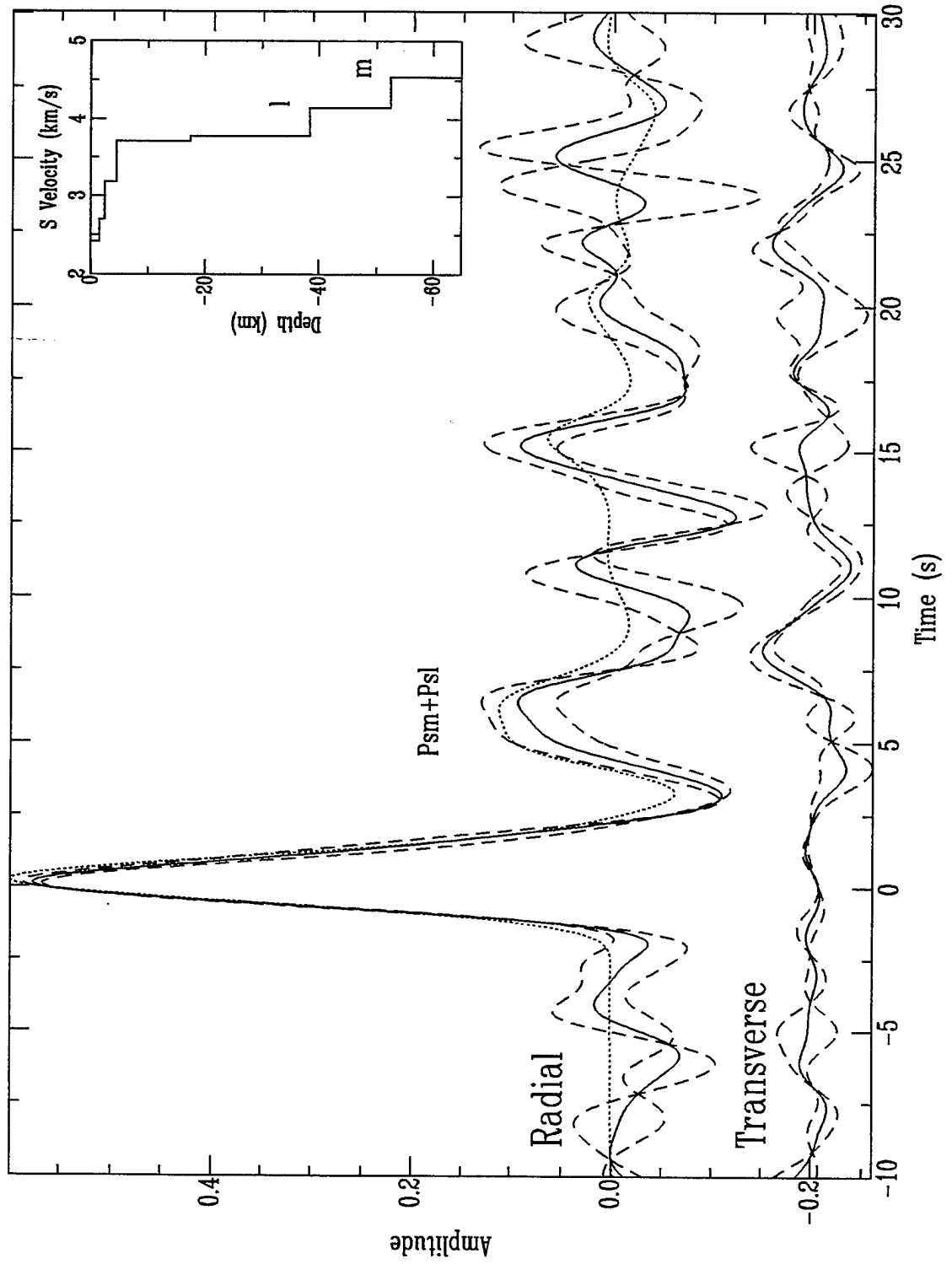


FIGURE A4

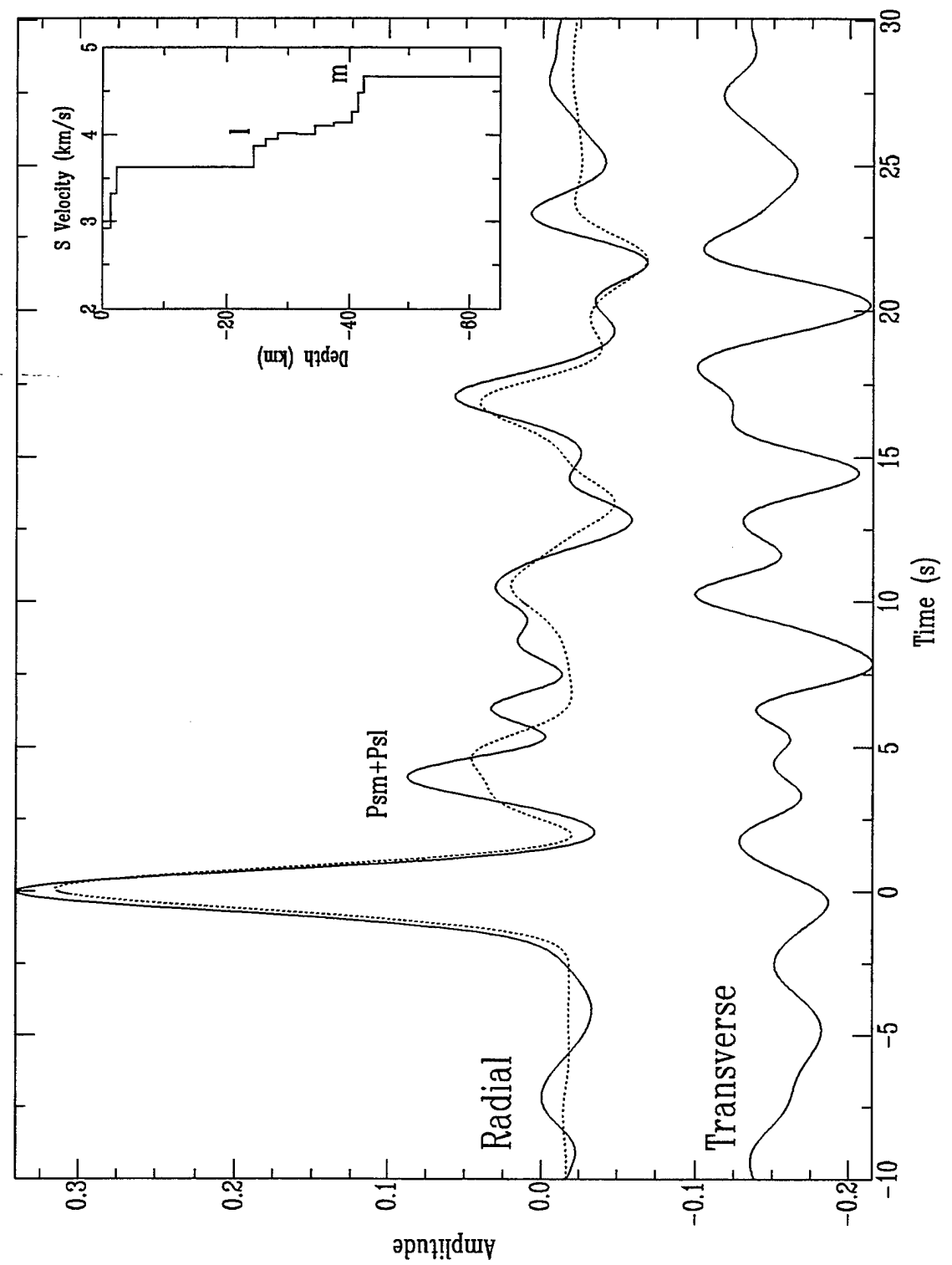


FIGURE A5

APPENDIX B Regional Waveform Analysis

This appendix discusses in more detail the determination of path-average velocity and density structure from the regional seismic waveforms of the eight earthquakes listed in Table 1. We give additional details of the analysis procedure we have followed using the July 18, 1986 event as an example, and then summarize the results for the other events.

The seismograms of the July 18, 1986 earthquake recorded at SLR have been described above. The earthquake occurred within the Irumide mobile belt north of the Zimbabwe Craton and the propagation path was largely confined to the Archaean core. The epicenter was almost due north of SLR so the recorded seismograms are close to normally rotated (E-W tangential, N-S radial). We first compare the observed waveform with synthetic waveforms (Fig 7a) computed using the CMT mechanism and an earth model consisting of the average crustal model determined above (section 3.2) overlying the mantle shear wave velocity structure determined by Bloch *et al.* (1969) from surface wave dispersion analysis. This earth model is parameterized in terms of flat-lying layers of constant V_s ; V_p is related to V_s by assuming a Poisson's ratio σ of 0.25 and the density is related to V_p by $\rho = 0.77 + 0.32 V_p$. The compressional and shear wave Q's were assumed to be 1000 and 500, respectively, for the crust (Clouser & Langston, 1990) and 700 and 300, respectively, for the mantle. We then altered the source mechanism by $\pm 10^\circ$ in strike, dip, and slip, and the hypocenter by ± 10 km in depth and distance to verify that the observed misfit was not the result of errors in the hypocenter or source mechanism. We could not improve the synthetic fit to the observed waveform in this way.

To invert the waveform data for earth structure we first parameterized the starting model in terms of a large number of thin, homogeneous layers. We constrain the inversion using bounds on the crustal structure from the seismic refraction and teleseismic receiver function studies (Fig. 4) and bounds on the velocity of the upper portions of the mantle lid from the P_n and S_n traveltimes (Fig. 5). We then inverted the three-components seismograms using the differential seismogram inversion technique of Gomberg & Masters (1988). Once the main character of the model boundaries became apparent from the initial inversions, the number of layers was reduced by grouping layers with similar parameters thus fixing the main boundaries; the final velocities and density of these thicker layer units were determined by reinverting the waveforms. We have tested the effects of varying the mantle Q structure and find that the velocity models resulting from the waveform inversion are relatively insensitive to reasonable variations in the Q structure. Gomberg & Masters (1988) found a similar result.

We next tried to assess the effects of errors in our data and assumptions on the inversion results. We initially assumed the CMT source mechanism and the ISC or PDE location for the events in inverting the regional waveforms but found that in several cases these did not produce good synthetic fits to the observed seismograms. Good fits could be obtained after slightly altering the CMT source mechanism and/or ISC or PDE depth. Both the CMT source mechanism and the final mechanisms and depths used in the inversion are given in Table 2. Errors in the source mechanism and depth will map into the earth structure. To assess the effect of these potential errors we have performed a series of tests in which we held all but one of the source parameters fixed at the values of the final mechanism in Table 2, varied the value of the remaining parameter by a reasonable amount and reinverted the seismic waveform giving a new earth model. We have varied the strike, slip, and dip of the source mechanism by $\pm 10^\circ$ and the distance and depth by ± 10 km. The effects of depth variations are so pronounced that the inversion could not converge when the depth varied by this amount and we conclude from this that the regional surface waveforms provide strong constraints on the focal depth. Of the remaining parameters, the largest effects are for variations in distance and dip. The bounds shown in Figure 7c represent the largest changes in the inversion earth model for the July 18, 1986 event, resulting from these tests. The effect of these variations is dependent on the epicentral distance but the results of

these tests suggest that for the magnitude of the errors in distance, strike, dip, and slip possible for the southern African events we have used, errors in velocities could be as large as $\pm 0.1 \text{ km s}^{-1}$ and errors in density could be as large as $\pm 0.05 \text{ g cm}^{-3}$.

We have assumed that lateral variations in earth structure along the propagation path are negligible and that the material is isotropic. The resulting earth model could be biased if either of these assumptions are wrong. Both assumptions are difficult to test with the data available and at this point we cannot make a quantitative statement of their influence on our result. We have shown above that the crust of southern Africa is of variable thickness but in general is 41 ± 6 km thick. The regional surface waveforms are well fit with a crust of almost uniform thickness of 41 km over southern Africa. The major variation in the crustal structure results from variations in the seismic velocities in the shallow (< 10 km) crust. The nucleus of southern Africa consists of the Archaean Zimbabwe and Kaapvaal Cratons which are dated at about 2.6 Ga, and the intervening Limpopo mobile belt of similar or slightly younger age. The long period of tectonic stability of the region might suggest that lateral variations in the mantle velocity structure of southern Africa are also relatively minor. However Ballard & Pollack (1987) suggest the observed heat flow variations in southern Africa can be explained by a thicker lithospheric root beneath the cratons than beneath the mobile belts. Some global models show thick roots under the cratonic regions including southern Africa but there is no consensus on this issue. A somewhat thicker lithospheric root beneath the cratons is also suggested by the distribution of diamond-bearing kimberlites. The pressure and temperature from the kimberlite nodules also suggest that the lithospheric thickness varies from 185 km beneath the Kaapvaal Craton to 163 km thick beneath the mobile belts (Finnerty & Boyd, 1987; McKenzie, 1989). Most of the propagation paths discussed in this study are largely confined to the Archaean core but they do extend across portions of the surrounding mobile belts and some of the events occur in the southern rift (Fig. 2). While lateral variations in the lithospheric and upper mantle structure undoubtedly occur, the similarity of the individual path-average earth models suggest to us that these effects are small in southern Africa.

Strong anisotropy in the lithosphere or upper mantle could also bias our results. The low frequency surface wave observations of Nataf *et al.* (1984) show the upper mantle beneath southern Africa is isotropic. Vinnik *et al.* (1995) measured shear wave splitting from SKS and similar phases at seven sites on the Kaapvaal Craton and found an average delay of 0.9 ± 0.5 sec. They conclude from thermal and mineralogical arguments that the anisotropy is localized between 150 and 400 km depth requiring 2% S-wave anisotropy. We assume that the lithosphere and upper mantle are isotropic and simultaneously inverted both the Love and Rayleigh waves to determine the path-average earth model. For the frequency range of our data we found no evidence of anisotropy in the Love and Rayleigh waves. Thus, while we cannot make quantitative statements about the effects of lateral variations in structure or anisotropy, there is nothing apparent in our data to indicate that these effects have strongly biased our inversion results.

We have next determined the upper mantle compressional wave velocity structure by forward modeling the P_{nl} waveform using reflectivity synthetics (Fuchs & Müller, 1971). We first converted the "blocky" earth model determined from the locked-mode inversion into a smoother earth model by increasing the number of layers and changing some of the velocity steps in the coarse earth model into gradients. We then checked to see that these smoothed models produced essentially the same locked-mode synthetic seismograms as the original coarse models. As discussed above, we used generalized ray synthetic seismograms to gain some insight into the rays composing the initial P-wave. We computed reflectivity synthetic seismograms for the smoothed earth model and found that the amplitude of the synthetic P-wave first arrival was too small compared to the observed amplitude, suggesting that there was insufficient energy in the synthetic mantle turning wave. We replaced the upper mantle P-wave velocity structure of our model obtained by inversion with that of model SACM06c of Clouser & Langston (1990)

and found that this produced first arrival amplitudes which were in better agreement with the observed P_{nl} waveform while preserving the fit of the surface waves. The epicentral distance of the July 18, 1986 event to SLR is similar to the largest epicentral distances of events in the Clouser & Langston (1990) study. When we modeled events at larger epicentral distances the synthetic waveform fits were not as good. Through a trial-and-error procedure illustrated in Figures B1–3, we finally concluded that the best fit over the entire distance range of our data was achieved for an upper mantle compressional wave velocity model with a positive gradient throughout the upper mantle, but smaller than the gradient in model SACM06c.

As pointed out by Clouser & Langston (1990), our choice of upper mantle Q_p and Q_s values affects the amplitudes of the synthetic waveforms. If we had chosen higher Q values then a smaller velocity gradient would be required to fit the P-wave amplitude, but this smaller velocity gradient would result in a degradation of the travel time match. It does not seem likely that a reasonable change in the Q structure would remove the effects of a LVZ in the data.

The absence of a P-wave LVZ leads to a question of the resolution of the S-wave LVZ by the regional surface wave data. We performed a number of tests to ascertain the sensitivity of the regional waveform data to the details of the upper mantle structure. The V_{S_n} of the model in Figure B4a is constrained by the S_n observations in Figure 5 and has the LVZ replaced by a positive gradient. This generates synthetic seismograms which have larger higher mode amplitudes than those seen in the data, suggesting too much energy in the synthetic seismogram. This also leads to a slight mismatch in phase resulting in the higher mode and the low frequency fundamental mode in the synthetic leading the observed phases. We found it impossible to find S-wave velocity models which fit the S_n travel times from Figure 5 but which did not contain a S-wave LVZ.

Stronger evidence for the existence and shape of the S-wave LVZ comes from tests on more distant events. Figure B4b compares observed seismograms for the July 24, 1991 earthquake (Event 10, Table 1) recorded at SUR and reflectivity synthetics computed for a model without a S-wave LVZ. The S_a phase, the long period arrival at about 470 sec and primarily seen on the vertical component, arises from the coupling of energy turning in the upper mantle lid and in the positive gradient at the base of the LVZ near 400 km depth (Priestley *et al.*, 1980). The S_a phase in the synthetic seismogram for the case of no S-wave LVZ is both weaker in amplitude and advanced in travel time compared with the observed S_a phase. On the other hand, Figure B4c shows that for a somewhat stronger S-wave LVZ, the S_a phase has both a greater amplitude and delayed travel time compared to the observed S_a phase.

Finally we tested the sensitivity of our data to the lid thickness by comparing the observed seismograms to synthetic seismograms computed for models with the thickness of the lid varying from 50 to 110 km thickness. Figure B5a shows a comparison of the observed waveforms with synthetics computed for an earth model with a S-wave LVZ starting at 90 km depth. The higher mode amplitude is less than that of the observed waveform, suggesting that there is insufficient S-wave energy turning from the upper mantle lid. In addition, both the higher mode and the low frequency fundamental mode are delayed with respect to the corresponding observed phases. Figure B5b shows the similar comparison for a lid thickness of 110 km, that is, the S-wave LVZ starting at a depth of 150 km. These show the opposite effect – larger higher mode amplitudes and advanced travel time compared to the observed data. Tests for smaller changes in the lid thickness produced changes in the synthetic waveforms which were difficult to distinguish from the observed waveform and we therefore feel that these represent maximum bounds on the thickness of the S-wave lid.

The remaining figures of this appendix (Figs. B6–B16) show the models and the fit of the synthetic and observed seismograms for the remaining eleven, three-component seismograms which we analyzed. The path average model for each are given in Tables B1 to B11. The quality of the data and the synthetic – observed waveform fits are discussed in the captions to these figures.

Table B1 Earth Model for July 7, 1983 – SLR

Depth km	Thick. km	V_P km s^{-1}	V_S km s^{-1}	ρ g cm^{-3}	Depth km	Thick. km	V_P km s^{-1}	V_S km s^{-1}	ρ g cm^{-3}
0	1	4.20	2.45	2.10	200	30	8.32	4.20	3.40
1	5	6.20	3.59	2.80	230	30	8.35	4.20	3.42
6	20	6.36	3.71	2.82	260	25	8.41	4.23	3.44
26	15	6.78	3.98	2.90	285	25	8.48	4.30	3.46
41	20	8.12	4.64	3.30	310	25	8.55	4.37	3.48
61	20	8.14	4.66	3.31	335	25	8.62	4.44	3.50
81	20	8.16	4.67	3.33	360	25	8.69	4.51	3.52
101	20	8.20	4.71	3.35	385	25	8.80	4.62	3.55
121	26	8.20	4.48	3.36	410	42	9.10	4.80	3.76
147	26	8.24	4.39	3.37	452	8	9.27	4.92	3.81
174	26	8.28	4.25	0.00					

Table B2 Earth Model for April 16, 1988 – SLR

Depth km	Thick. km	V_P km s^{-1}	V_S km s^{-1}	ρ g cm^{-3}	Depth km	Thick. km	V_P km s^{-1}	V_S km s^{-1}	ρ g cm^{-3}
0	1	3.98	2.41	2.20	200	30	8.32	4.30	3.40
1	5	6.12	3.57	2.79	230	30	8.35	4.30	3.42
6	20	6.35	3.70	2.82	260	25	8.41	4.33	3.44
26	15	6.76	3.98	2.92	285	25	8.48	4.38	3.46
41	20	8.10	4.66	3.30	310	25	8.55	4.43	3.48
61	20	8.12	4.67	3.32	335	25	8.62	4.48	3.50
81	20	8.15	4.68	3.33	360	25	8.69	4.53	3.52
101	20	8.20	4.71	3.35	385	25	8.80	4.61	3.55
121	26	8.20	4.48	3.36	410	42	9.10	4.80	3.76
147	26	8.24	4.42	3.37	452	8	9.27	4.92	3.81
174	26	8.28	4.33	0.00					

Table B3 Earth Model for March 9, 1989 – SLR

Depth km	Thick. km	V_P km s^{-1}	V_S km s^{-1}	ρ g cm^{-3}	Depth km	Thick. km	V_P km s^{-1}	V_S km s^{-1}	ρ g cm^{-3}
0	1	4.51	2.65	2.29	183	17	8.14	4.39	3.40
1	5	6.38	3.56	2.76	200	17	8.16	4.36	3.41
6	20	6.48	3.68	2.94	217	17	8.19	4.34	3.42
26	15	6.73	4.03	3.08	233	17	8.21	4.31	3.43
41	21	8.00	4.56	3.28	250	27	8.27	4.35	3.44
63	21	8.01	4.60	3.30	277	27	8.36	4.45	3.46
84	21	8.01	4.63	3.32	303	27	8.46	4.55	3.49
105	21	8.02	4.69	3.35	330	27	8.56	4.65	3.51
126	8	8.02	4.47	3.37	357	27	8.65	4.75	3.53
134	8	8.04	4.46	3.37	383	27	8.80	4.90	3.57
142	8	8.07	4.45	3.38	410	31	9.20	5.10	3.76
150	17	8.09	4.44	3.38	441	19	9.32	5.17	3.79
167	17	8.11	4.41	0.00					

Table B4 Earth Model for March 10, 1989 – SLR

Depth km	Thick. km	V_P km s^{-1}	V_S km s^{-1}	ρ g cm^{-3}	Depth km	Thick. km	V_P km s^{-1}	V_S km s^{-1}	ρ g cm^{-3}
0	1	4.51	2.66	2.30	183	17	8.13	4.39	3.40
1	5	6.34	3.58	2.77	200	17	8.15	4.36	3.41
6	20	6.42	3.68	2.95	217	17	8.18	4.34	3.42
26	15	6.71	4.03	3.07	233	17	8.21	4.31	3.43
41	21	7.99	4.52	3.27	250	27	8.27	4.35	3.44
63	21	7.99	4.56	3.29	277	27	8.36	4.45	3.46
84	21	8.00	4.60	3.31	303	27	8.46	4.55	3.49
105	21	8.02	4.67	3.35	330	27	8.56	4.65	3.51
126	8	8.02	4.47	3.37	357	27	8.65	4.75	3.53
134	8	8.03	4.46	3.37	383	27	8.80	4.90	3.57
142	8	8.05	4.45	3.38	410	31	9.20	5.10	3.76
150	17	8.07	4.44	3.38	441	19	9.32	5.17	3.79
167	17	8.10	4.41	0.00					

Table B5 Earth Model for November 3, 1990 – SLR

Depth km	Thick. km	V_P km s^{-1}	V_S km s^{-1}	ρ g cm^{-3}	Depth km	Thick. km	V_P km s^{-1}	V_S km s^{-1}	ρ g cm^{-3}
0	1	4.49	2.70	2.09	200	20	8.32	4.43	3.43
1	5	5.18	3.22	2.43	220	20	8.39	4.41	3.44
6	20	6.35	3.60	3.11	240	13	8.43	4.41	3.45
26	15	6.65	4.00	3.18	253	13	8.48	4.43	3.46
41	16	8.05	4.65	3.35	267	13	8.53	4.45	3.46
57	16	8.07	4.66	3.35	280	22	8.59	4.49	3.47
73	16	8.09	4.67	3.36	302	22	8.67	4.56	3.49
89	16	8.10	4.68	3.37	323	22	8.75	4.63	3.50
105	16	8.14	4.69	3.38	345	22	8.83	4.70	3.51
121	20	8.15	4.50	3.38	367	22	8.91	4.77	3.53
141	20	8.19	4.48	3.40	388	22	9.03	4.87	3.55
161	20	8.23	4.47	3.41	410	42	9.36	5.07	3.76
181	20	8.28	4.45	3.42	452	8	9.50	5.16	3.81

Table B6 Earth Model for July 24, 1991 – SLR

Depth km	Thick. km	V_P km s^{-1}	V_S km s^{-1}	ρ g cm^{-3}	Depth km	Thick. km	V_P km s^{-1}	V_S km s^{-1}	ρ g cm^{-3}
0	1	5.00	3.05	2.50	200	20	8.34	4.43	3.43
1	5	6.20	3.75	3.00	220	20	8.39	4.41	3.44
6	20	6.20	3.75	3.00	240	13	8.43	4.41	3.45
26	15	6.75	4.16	3.16	253	13	8.48	4.43	3.46
41	16	8.11	4.61	3.35	267	13	8.53	4.45	3.46
57	16	8.13	4.63	3.35	280	22	8.59	4.49	3.47
73	16	8.15	4.65	3.36	302	22	8.67	4.56	3.49
89	16	8.17	4.66	3.36	323	22	8.75	4.63	3.50
105	16	8.21	4.70	3.37	345	22	8.83	4.70	3.51
121	20	8.22	4.50	3.38	367	22	8.91	4.77	3.53
141	20	8.25	4.48	3.39	388	22	9.03	4.87	3.55
161	20	8.28	4.47	3.40	410	42	9.36	5.07	3.76
181	20	8.31	4.45	3.41	452	8	9.50	5.16	3.81

Table B7 Earth Model for July 24, 1991 – SUR

Depth km	Thick. km	V_P km s^{-1}	V_S km s^{-1}	ρ g cm^{-3}	Depth km	Thick. km	V_P km s^{-1}	V_S km s^{-1}	ρ g cm^{-3}
0	6	5.81	3.47	2.69	200	20	8.33	4.48	3.40
6	20	5.97	3.70	2.79	220	20	8.41	4.48	3.42
26	15	6.66	4.11	3.00	240	28	8.51	4.51	3.44
41	21	8.07	4.65	3.32	268	28	8.60	4.57	3.46
62	21	8.09	4.68	3.33	297	28	8.70	4.62	3.48
84	21	8.12	4.70	3.34	325	28	8.79	4.68	3.50
105	21	8.16	4.76	3.35	353	28	8.89	4.73	3.52
126	25	8.19	4.59	3.36	382	28	9.03	4.81	3.55
151	25	8.22	4.55	3.37	410	42	9.36	5.01	3.76
175	25	8.27	4.50	3.39	452	8	9.50	5.10	3.81

Table B8 Earth Model for August 18, 1994 – BOSA

Depth km	Thick. km	V_P km s^{-1}	V_S km s^{-1}	ρ g cm^{-3}	Depth km	Thick. km	V_P km s^{-1}	V_S km s^{-1}	ρ g cm^{-3}
0	1	5.91	3.19	2.50	200	20	8.35	4.33	3.40
1	5	6.28	3.68	2.84	220	20	8.40	4.31	3.42
6	20	6.30	3.68	2.86	240	13	8.44	4.30	3.43
26	15	6.74	4.01	2.97	253	13	8.48	4.30	3.44
41	16	8.10	4.64	3.30	267	13	8.53	4.30	3.45
57	16	8.12	4.67	3.31	280	22	8.59	4.34	3.46
73	16	8.14	4.69	3.32	302	22	8.68	4.43	3.48
89	16	8.16	4.72	3.33	323	22	8.77	4.52	3.49
105	16	8.20	4.78	3.34	345	22	8.86	4.60	3.51
121	20	8.20	4.40	3.35	367	22	8.95	4.69	3.53
141	20	8.24	4.38	3.36	388	22	9.08	4.82	3.55
161	20	8.28	4.37	3.38	410	42	9.40	5.02	3.76
181	20	8.31	4.35	3.39	452	8	9.54	5.16	3.81

Table B9 Earth Model for August 18, 1994 – LBTB

Depth km	Thick. km	V_P km s^{-1}	V_S km s^{-1}	ρ g cm^{-3}	Depth km	Thick. km	V_P km s^{-1}	V_S km s^{-1}	ρ g cm^{-3}
0	1	5.90	3.19	2.51	200	20	8.27	4.33	3.40
1	5	6.24	3.68	2.85	220	20	8.29	4.31	3.42
6	20	6.27	3.66	2.84	240	13	8.31	4.30	3.43
26	15	6.73	4.05	2.96	253	13	8.32	4.30	3.44
41	16	8.15	4.61	3.28	267	13	8.34	4.30	3.45
57	16	8.16	4.64	3.29	280	22	8.37	4.33	3.46
73	16	8.17	4.68	3.31	302	22	8.41	4.38	3.48
89	16	8.18	4.71	3.32	323	22	8.45	4.44	3.49
105	16	8.20	4.78	3.34	345	22	8.50	4.49	3.51
121	20	8.20	4.40	3.35	367	22	8.54	4.55	3.53
141	20	8.22	4.38	3.36	388	22	8.60	4.63	3.55
161	20	8.24	4.37	3.38	410	42	9.21	4.83	3.76
181	20	8.25	4.35	3.39	452	8	9.36	4.93	3.81

Table B10 Earth Model for August 18, 1994 – LSZ

Depth km	Thick. km	V_P km s^{-1}	V_S km s^{-1}	ρ g cm^{-3}	Depth km	Thick. km	V_P km s^{-1}	V_S km s^{-1}	ρ g cm^{-3}
0	1	5.92	3.15	2.50	200	20	8.25	4.34	3.40
1	5	6.29	3.70	2.84	220	20	8.29	4.31	3.42
6	20	6.35	3.66	2.85	240	13	8.32	4.30	3.43
26	15	6.75	3.96	2.95	253	13	8.36	4.30	3.44
41	16	8.07	4.60	3.24	267	13	8.40	4.30	3.45
57	16	8.09	4.65	3.26	280	22	8.46	4.35	3.47
73	16	8.11	4.70	3.29	302	22	8.56	4.44	3.48
89	16	8.12	4.75	3.31	323	22	8.65	4.54	3.50
105	16	8.16	4.84	3.36	345	22	8.75	4.63	3.51
121	20	8.17	4.41	3.36	367	22	8.84	4.73	3.52
141	20	8.19	4.39	3.37	388	22	8.98	4.87	3.55
161	20	8.21	4.37	3.38	410	42	9.38	5.07	3.76
181	20	8.23	4.36	3.39	452	8	9.52	5.16	3.81

Table B11 Earth Model for August 18, 1994 – SUR

Depth km	Thick. km	V_P km s^{-1}	V_S km s^{-1}	ρ g cm^{-3}	Depth km	Thick. km	V_P km s^{-1}	V_S km s^{-1}	ρ g cm^{-3}
0	1	5.88	3.16	2.51	200	20	8.18	4.42	3.41
1	5	6.15	3.61	2.86	220	20	8.20	4.38	3.42
6	20	6.16	3.67	2.80	240	13	8.23	4.37	3.43
26	15	6.85	4.18	2.88	253	13	8.28	4.37	3.44
41	16	8.10	4.52	3.23	267	13	8.34	4.37	3.45
57	16	8.11	4.58	3.26	280	22	8.42	4.41	3.46
73	16	8.11	4.63	3.29	302	22	8.53	4.50	3.48
89	16	8.12	4.69	3.31	323	22	8.64	4.58	3.49
105	16	8.13	4.80	3.37	345	22	8.75	4.66	3.51
121	20	8.13	4.53	3.37	367	22	8.86	4.75	3.52
141	20	8.14	4.50	3.38	388	22	9.03	4.88	3.55
161	20	8.16	4.48	3.39	410	42	9.43	5.07	3.76
181	20	8.17	4.45	3.40	452	8	9.57	5.18	3.80

APPENDIX B – FIGURE CAPTIONS

Figure B1. The right plot shows the observed, vertical component P-wave of Event 2 recorded at SLR ($\Delta = 1038$ km) (solid line) compared with synthetic seismograms computed for the final earth model for this event from Table 4 (dashed line) and with synthetic seismograms computed for this model but with increasing depths to the top of the P-wave LVZ (dotted line). The number in the upper left hand corner of each seismogram plot denotes the depth to the top of the P-wave LVZ for the model used to compute that synthetic. The left plot shows the P-wave structure of the final earth model (solid line) and of LVZ models tested (dotted lines). V_{P_n} for the LVZ models tested is the same in each case but the mantle portion of the models is offset to the left in the velocity plot to provide a clearer comparison with our final P-wave velocity model.

Figure B2. This is a similar test of the P-wave LVZ to that in Figure B1 but for the March 9, 1989 earthquake (Event 4, Table 1) recorded at SLR ($\Delta = 1479$ km). This figure is in the same format as Figure B1.

Figure B3. This is a similar test of the P-wave LVZ to that in Figure B1 but for the July 24, 1991 earthquake (Event 10, Table 1) recorded at SUR ($\Delta = 2106$ km). This figure is in the same format as Figure B1.

Figure B4. (a) Comparison of the observed seismograms of the July 18, 1986 earthquake (Event 2, Table 1) recorded at SLR ($\Delta = 1038$ km) compared to synthetic seismograms computed for the final earth model for this event (Table 4) (dashed line) and the same earth model but with the S-wave LVZ replaced with a constant gradient of the S-wave lid. (b) Similar comparison to that in (a) but for the July 24, 1991 earthquake (Event 10, Table 1) recorded at SUR ($\Delta = 2106$ km). (c) Comparison of the observed seismograms for the same event as in (b) but for a more pronounced S-wave LVZ.

Figure B5. Comparison of the observed seismograms of the July 18, 1986 earthquake (Event 2, Table 1) recorded at SLR ($\Delta = 1038$ km) compared to synthetic seismograms computed for the final earth model for this event (Table 4) (dashed line) and for the same earth model but with the S-wave LVZ starting at (a) 90 km and (b) 150 km depth (dotted lines).

Figure B6. *July 7, 1983 – SLR* (Event 1, Table 1): This event was located in the southern part of the western rift and was recorded at SLR ($\Delta = 2038$ km). The path to SLR crosses the Damara and Irumide Mobile Belts, the Zimbabwe Craton, the Limpopo Mobile Belt, and the Kaapvaal Craton. About 50% of the propagation path is across the Archaean core. The epicenter is almost due north of SLR so the observed seismograms are nearly naturally rotated (N–S radial, E–W transverse) so the vertical, north, and east components are plotted. The top panel of the figure plots the whole seismogram (observed – solid line, synthetic – dotted line) to show the overall waveform fit; the middle panel plots the early part of the seismogram enlarged to show the details of the lower amplitude P- and S-waves; the bottom panel plots the final earth model for this path from Table B1. All of the remaining figures of this appendix have the same format.

Figure B7. *April 16, 1988 – SLR* (Event 3, Table 1): This event occurred on the northern boundary of the Damara Mobile Belt almost due north of SLR, thus the seismograms are naturally rotated to radial (N–S) and transverse (E–W) so the vertical, north, and east components are plotted. The 1722 km long path crosses the Damara and Irumide Mobile belts, the Zimbabwe Craton, the Limpopo Mobile belt, and the Kaapvaal Craton. About 50% of the propagation path is across the Archaean core. The data quality for this event is poor compared to the other seismograms used in this study. The traces are affected by low ampli-

tude, long period noise and by spiking and the N-S component has been high-pass filtered with a three pole Butterworth filter with a corner at 0.05 Hz. The N-S synthetic was filtered in an identical manner. This noise makes the body wave portion of the seismograms for this event unusable. The S-wave velocity model shown here from Table B2 is a smoothed version of the locked mode inversion model.

Figure B8. March 9, 1989 – SLR (Event 4, Table 1): This event is located in the Zambezi Mobile Belt and the 1479 km long path crosses the Zimbabwe Craton, the Limpopo Mobile belt, and the Kaapvaal Craton. About 70% of the propagation path is across the Archaean core. The vertical seismogram is well fit but there is some long period noise, especially apparent on the N-S component. The model plotted in the lower panel is from Table B3.

Figure B9. March 10, 1989 – SLR (Event 5, Table 1): This event is co-located with the March 9, 1989 event but was larger and the largest amplitude surface waves are clipped. The horizontal seismograms have been rotated into radial and transverse. The model plotted in the lower panel is from Table B4.

Figure B10. November 3, 1990 – SLR (Event 8, Table 1): This event occurred near the northeast boundary of the Kaapvaal Craton. The path length of 705 km is the shortest in this study, and was almost entirely confined to the Kaapvaal Craton. The E-W component seismogram has been high-pass filtered with a three pole Butterworth filter with a corner at 0.05 Hz. The E-W synthetic was filtered in an identical manner. Because of this filtering the horizontal seismograms have not been rotated into radial and transverse. The model plotted in the lower panel is from Table B5.

Figure B11. July 24, 1991 – SLR (Event 10, Table 1): This event is located in the Zambezi Mobile Belt 1071 km northeast of SLR. The path crosses the southern portion of the Zambezi Mobile Belt, the Limpopo Mobile belt, and the Kaapvaal Craton. About 60% of the propagation path is confined to the Archaean core. There is some noise and spiking apparent on all components. Because of this noise, the seismograms have not been rotated and the vertical, north, and east components are plotted. The model plotted in the lower panel is from Table B6.

Figure B12. July 24, 1991 – SUR (Event 10, Table 1): This is the same event as in Figure B11 except recorded at station SUR ($\Delta = 2106$ km). This propagation path is similar to that to station SLR but also crosses the Namaqua Mobile Belt. About 50% of the propagation path is confined to the Archaean core. There is some long period noise especially apparent on the horizontal components. Both the observed and synthetic seismograms have been band-pass filtered with a three pole Butterworth filter with corners at 0.01 and 0.05 Hz. The horizontal seismograms have been rotated into radial (positive away from the source) and transverse (positive clockwise from source). The model plotted in the lower panel is from Table B7.

Figure B13. August 18, 1994 – BOSA (Event 12, Table 1): This event occurred north of the Zambia Craton and crossed the length of the stable region of southern Africa. About 60% of the propagation path to BOSA ($\Delta = 2447$ km) is confined to the Archaean core. Both the observed and synthetic seismograms have been low-pass filtered with a three pole Butterworth filter with a corner at 0.05 Hz. The horizontal seismograms have been rotated into radial and transverse. The model plotted in the lower panel is from Table B8.

Figure B14. August 18, 1994 – LBTB (Event 12, Table 1): This is the same event as in Figure B13 except recorded at station LBTB ($\Delta = 2062$ km). About 50% of the propagation path is confined to the Archaean core. Both the observed and synthetic seismograms have been low-pass filtered with a three pole Butterworth filter with a corner at 0.05 Hz. The horizontal

seismograms have been rotated into radial and transverse. The model plotted in the lower panel is from Table B9.

Figure B15. *August 18, 1994 – LSZ* (Event 12, Table 1): This is the same event as in Figure B13 except recorded at station LSZ ($\Delta = 955$ km). Station LSZ is located in the Irumide Mobile Belt and the earth model derived from these data is more representative of the Zambia Craton. Both the observed and synthetic seismograms have been low-pass filtered with a three pole Butterworth filter with a corner at 0.05 Hz. The horizontal seismograms have been rotated into radial and transverse. The model plotted in the lower panel is from Table B10.

Figure B16. *August 18, 1994 – SUR* (Event 12, Table 1): This is the same event as in Figure B13 except recorded at station SUR ($\Delta = 2996$ km). This is the longest path length of this study and samples the length of the stable region of southern Africa. About 70% of the propagation path lies within the Zambia, Zimbabwe, and Kaapvaal cratons and the Limpopo Mobile Belt. Both the observed and synthetic seismograms have been low-pass filtered with a three pole Butterworth filter with a corner at 0.05 Hz. The horizontal seismograms have been rotated into radial and transverse. The model plotted in the lower panel is from Table B11.

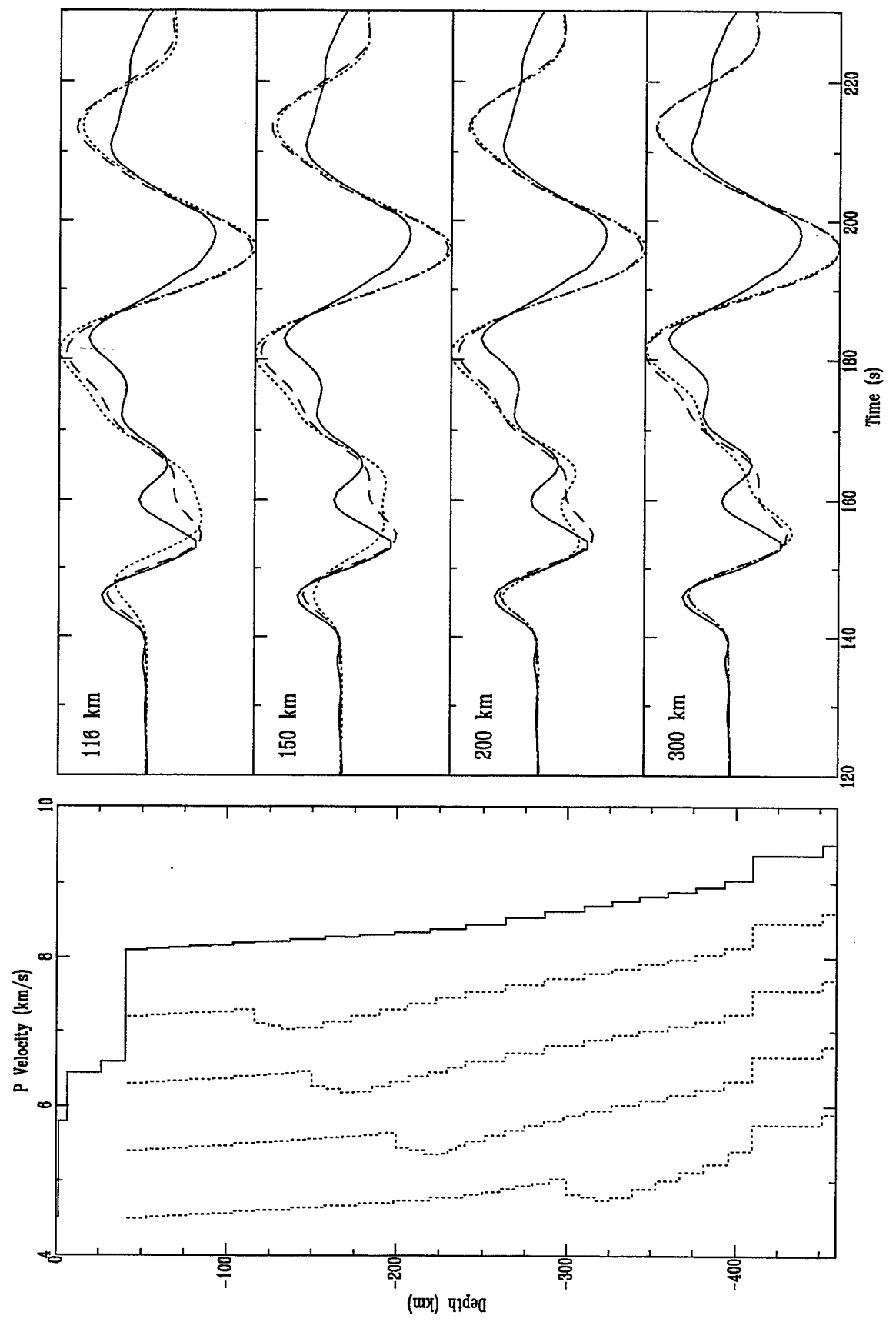


FIGURE B1

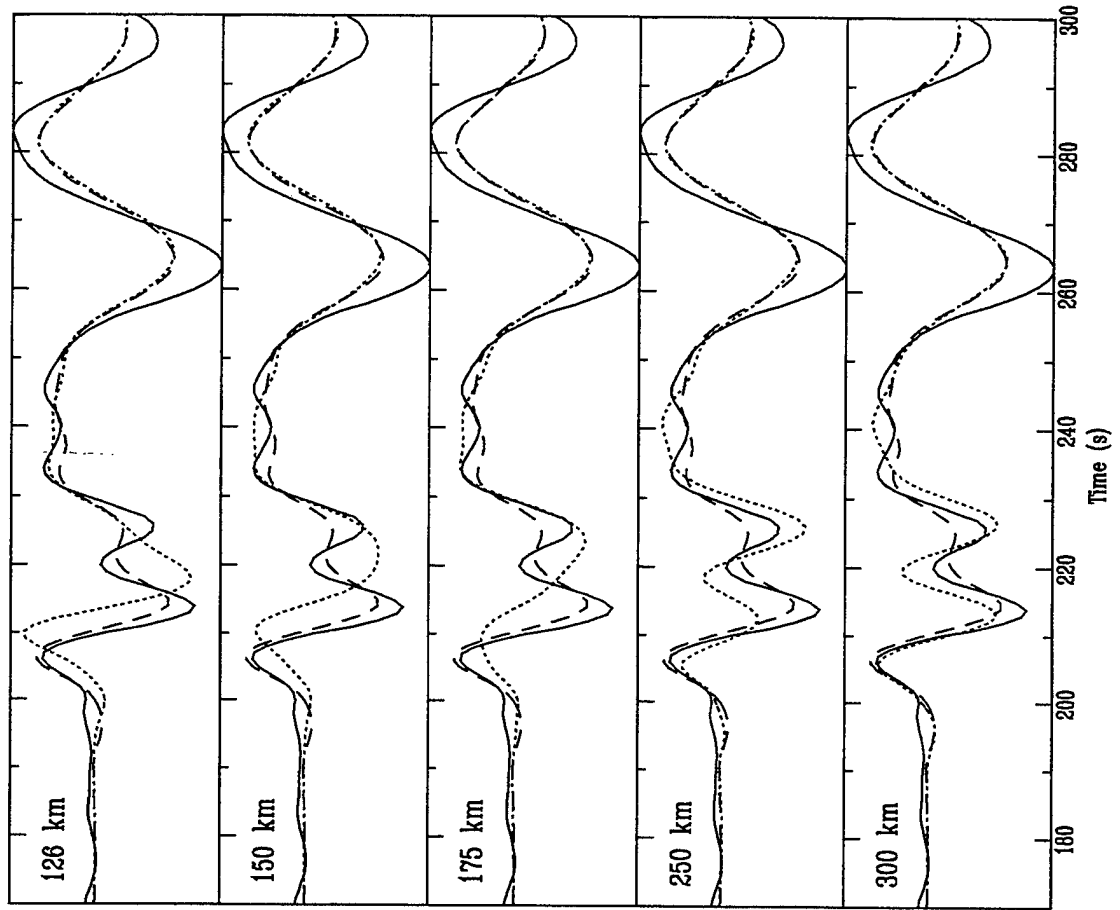
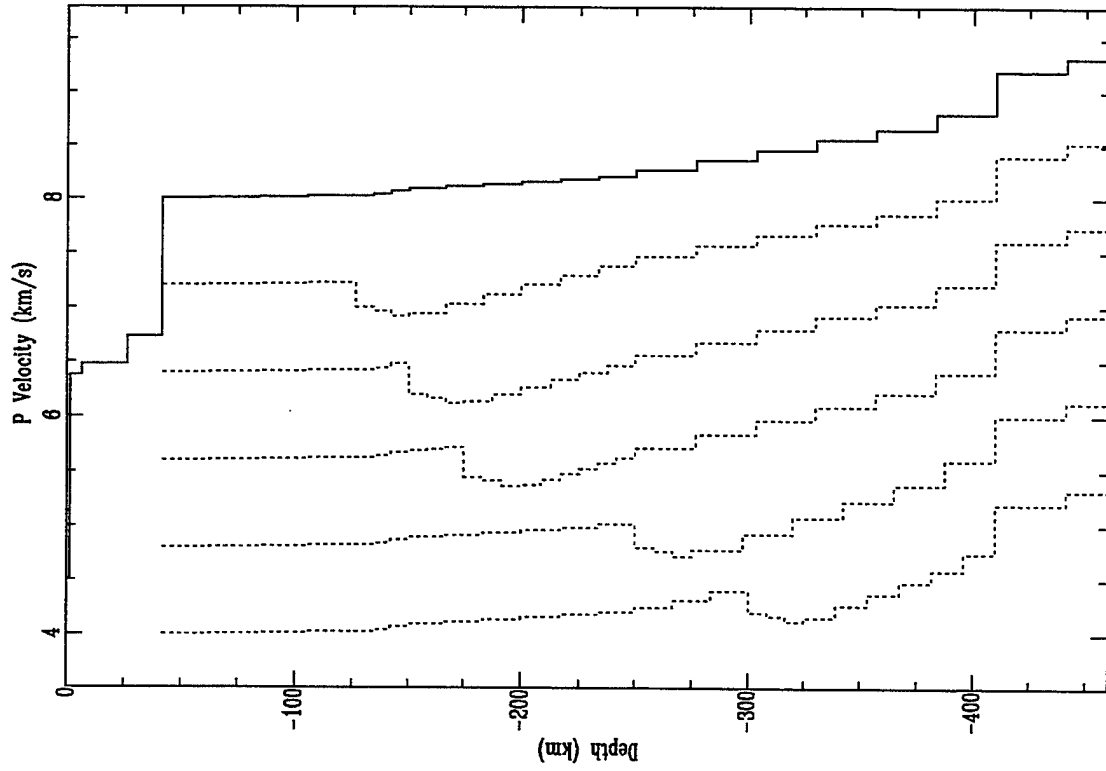


FIGURE B2



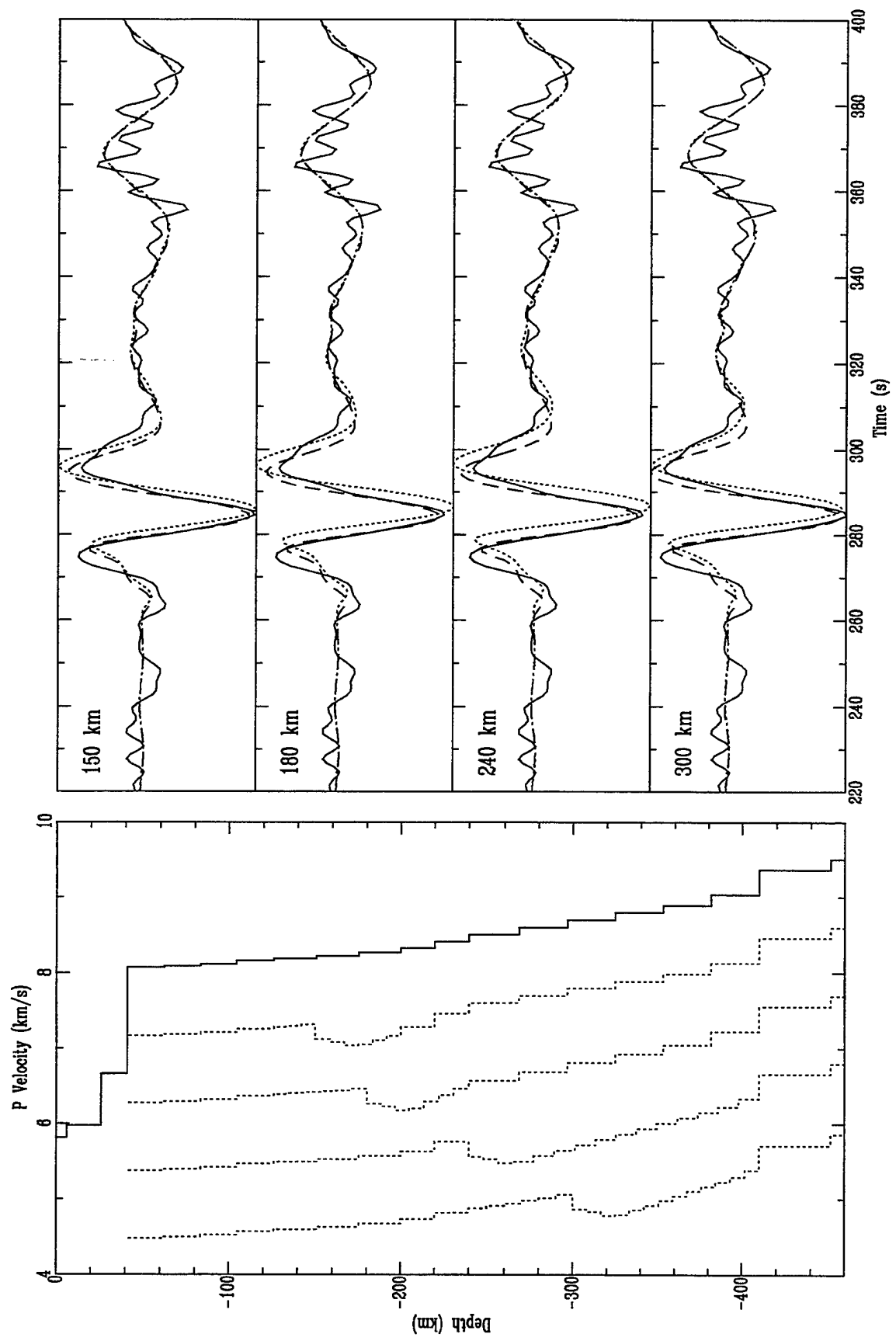


FIGURE B3

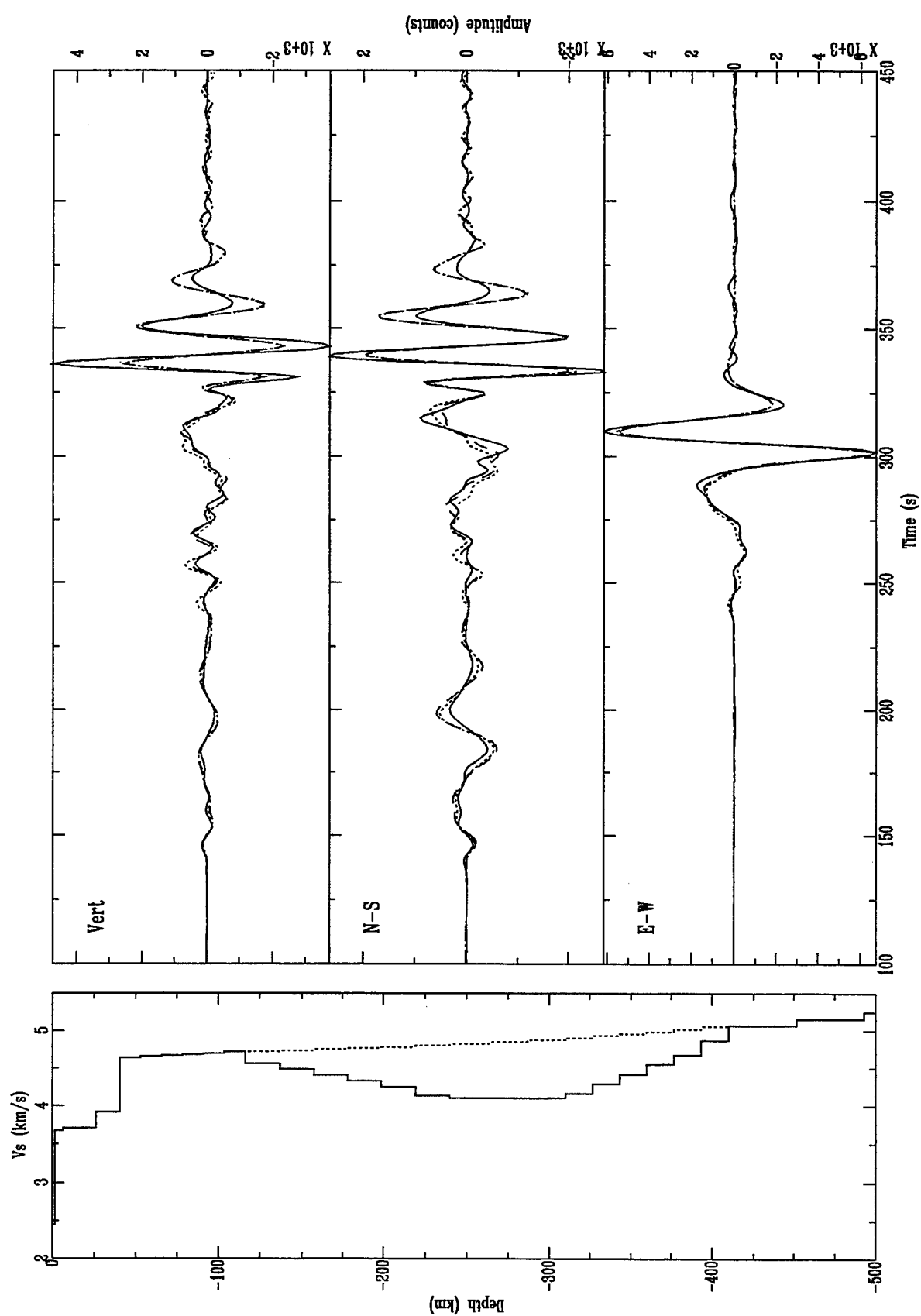


FIGURE B4a

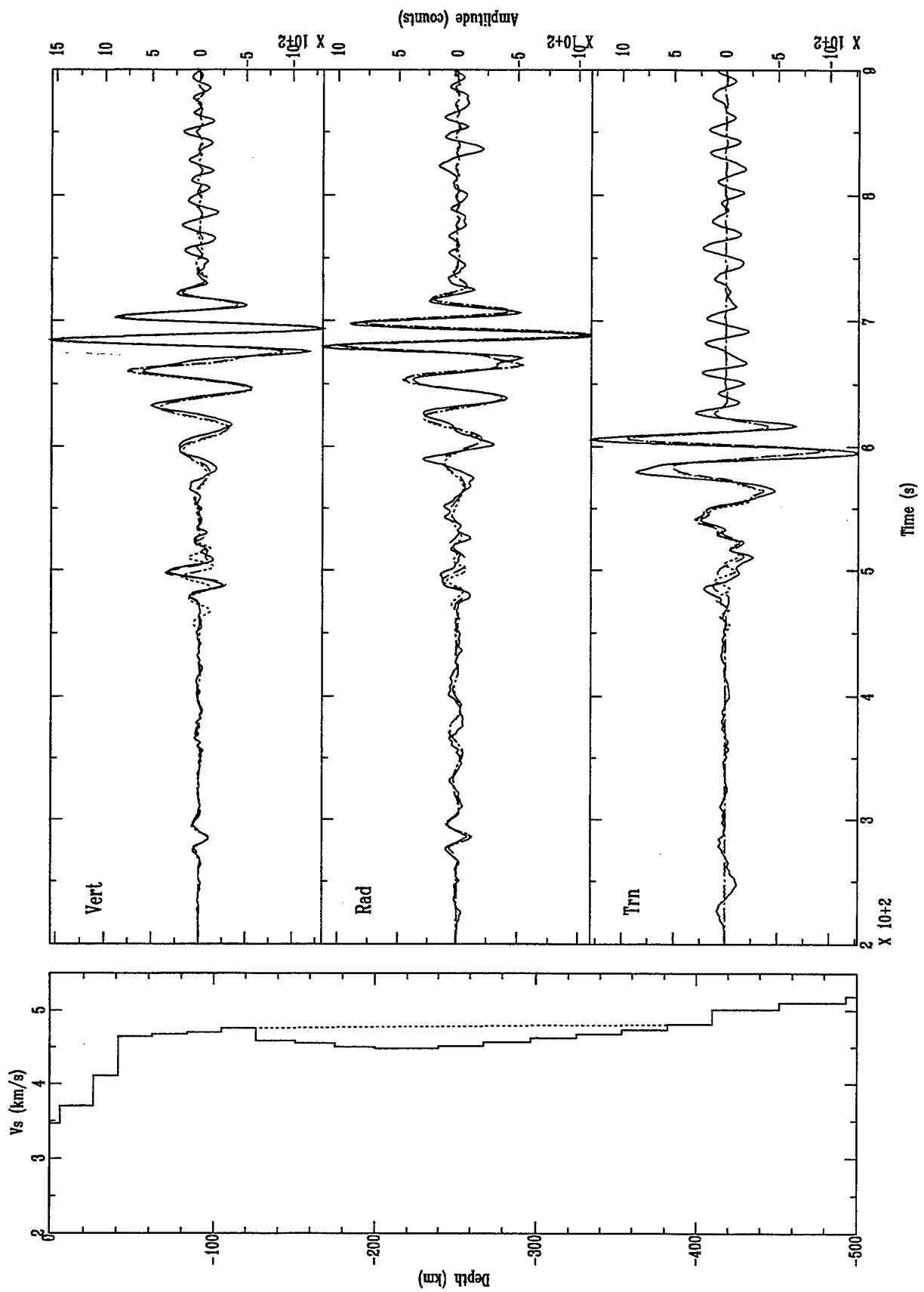


FIGURE B4b

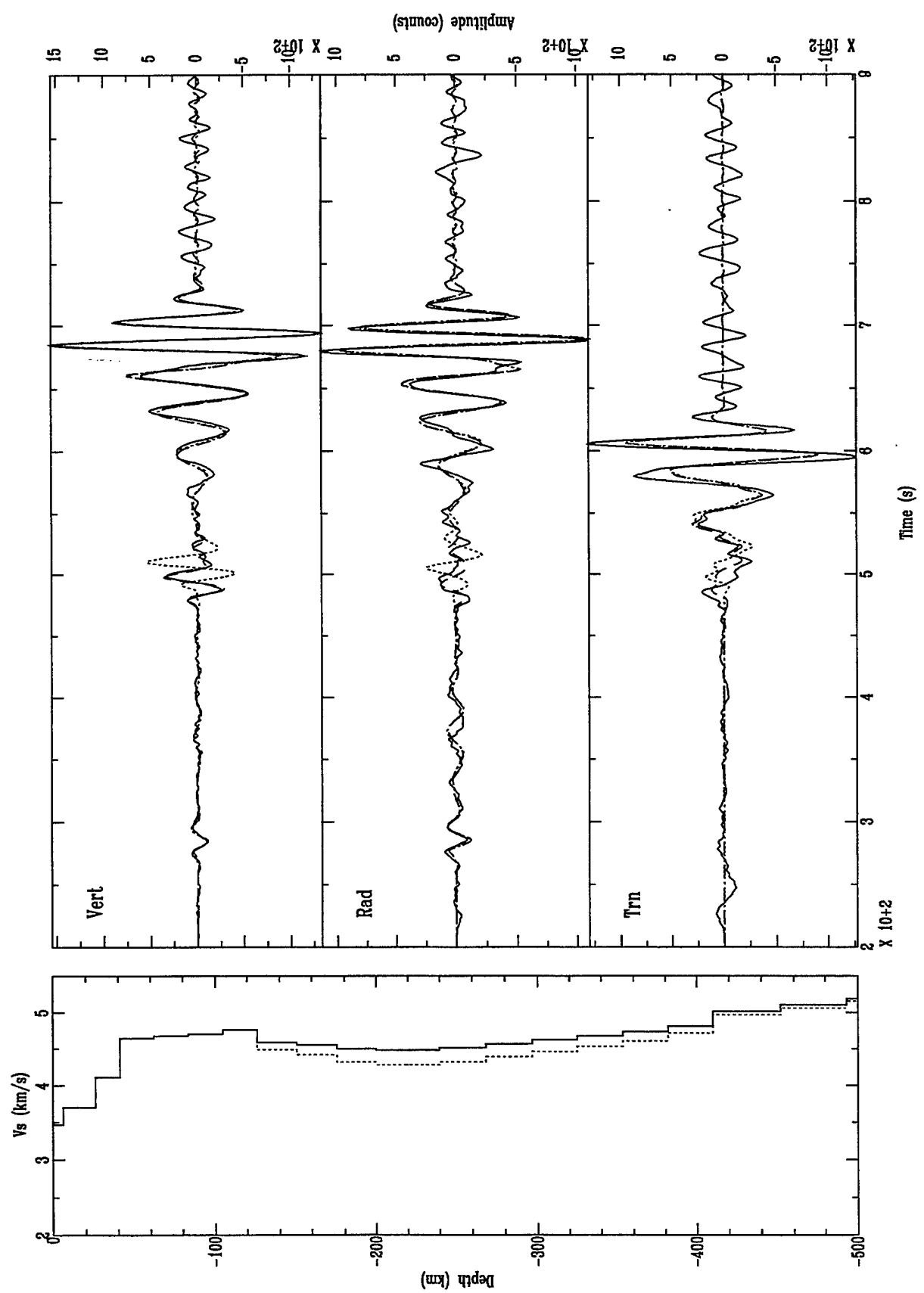


FIGURE B4c

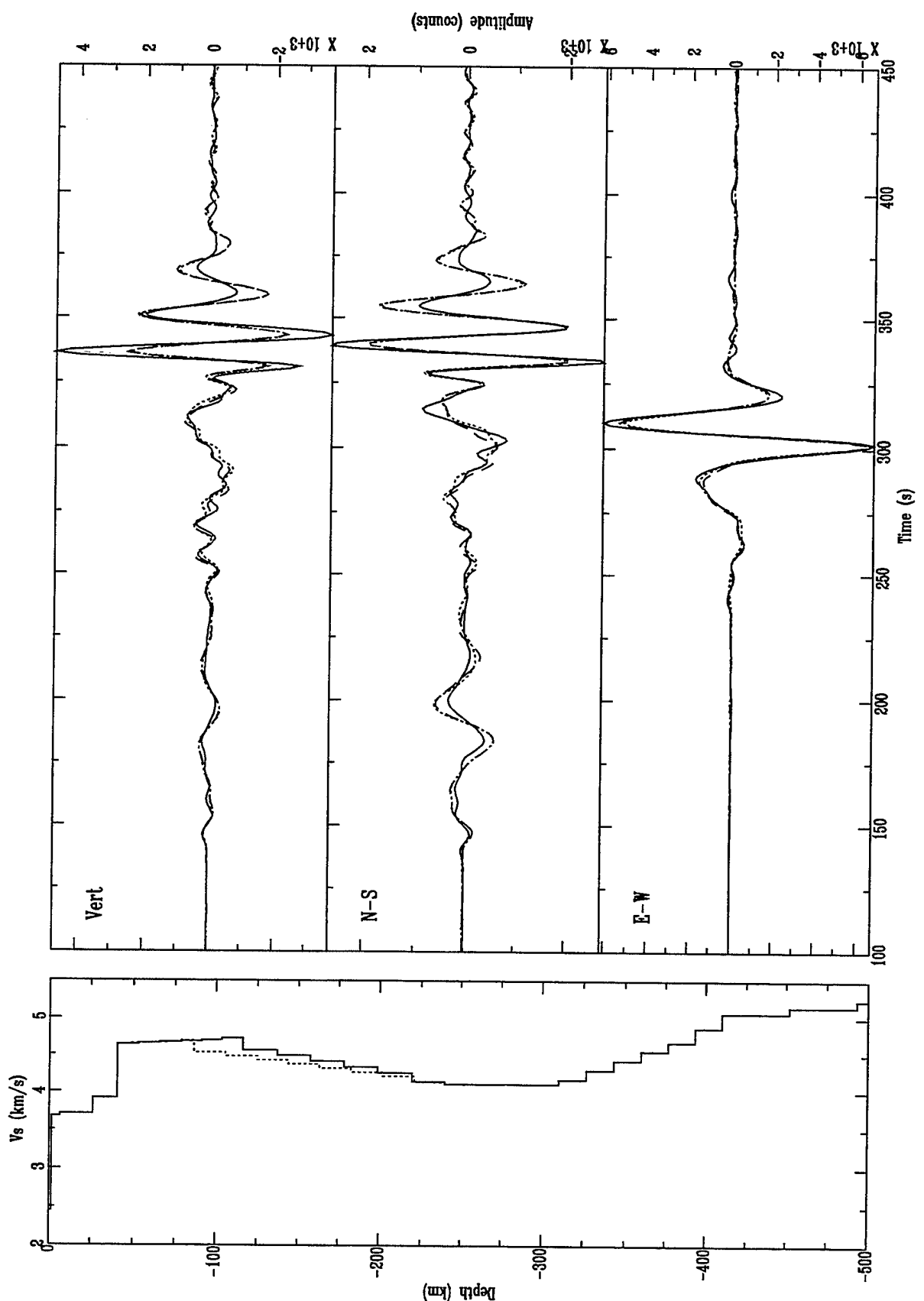


FIGURE B5a

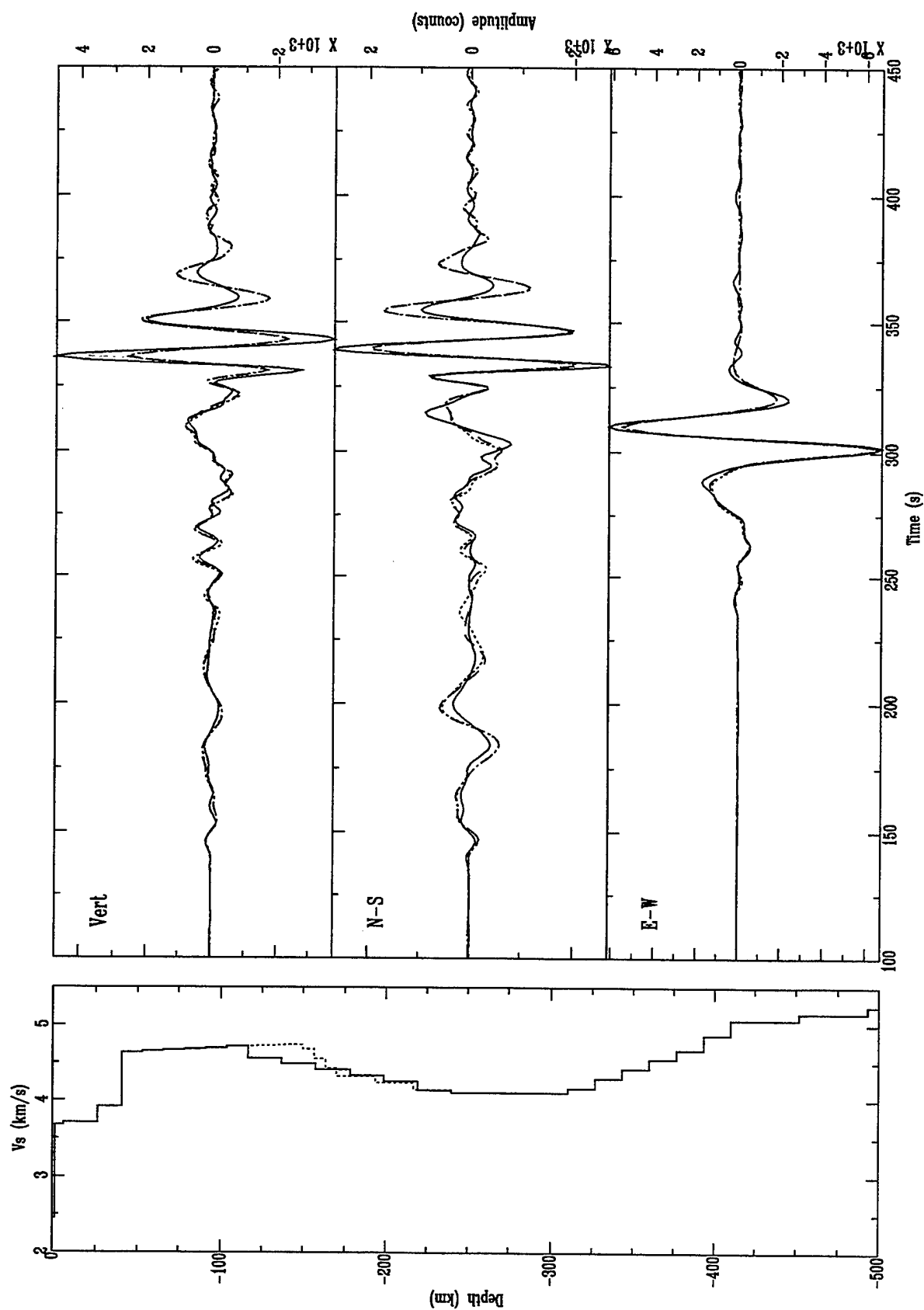


FIGURE B5b

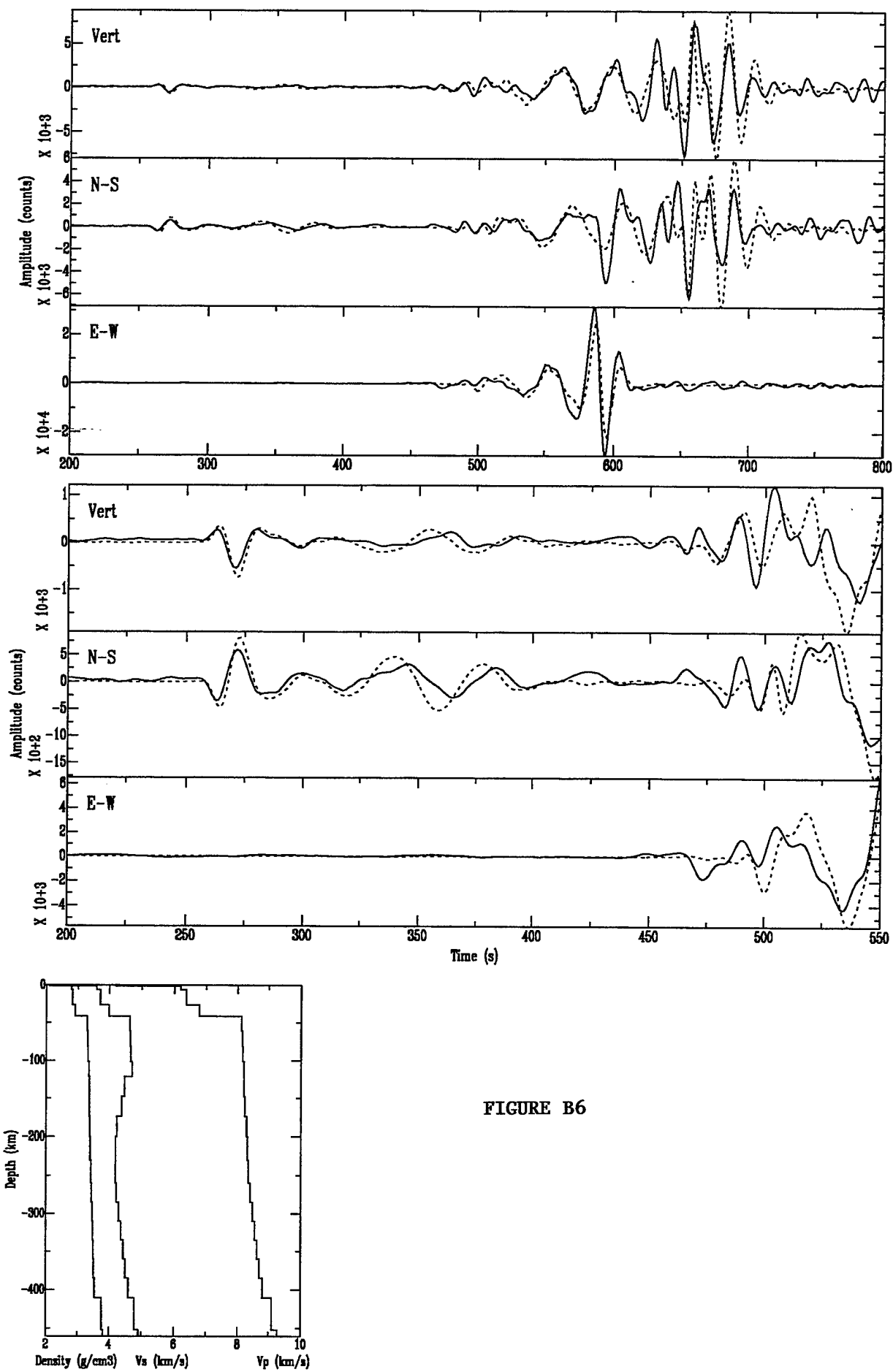


FIGURE B6

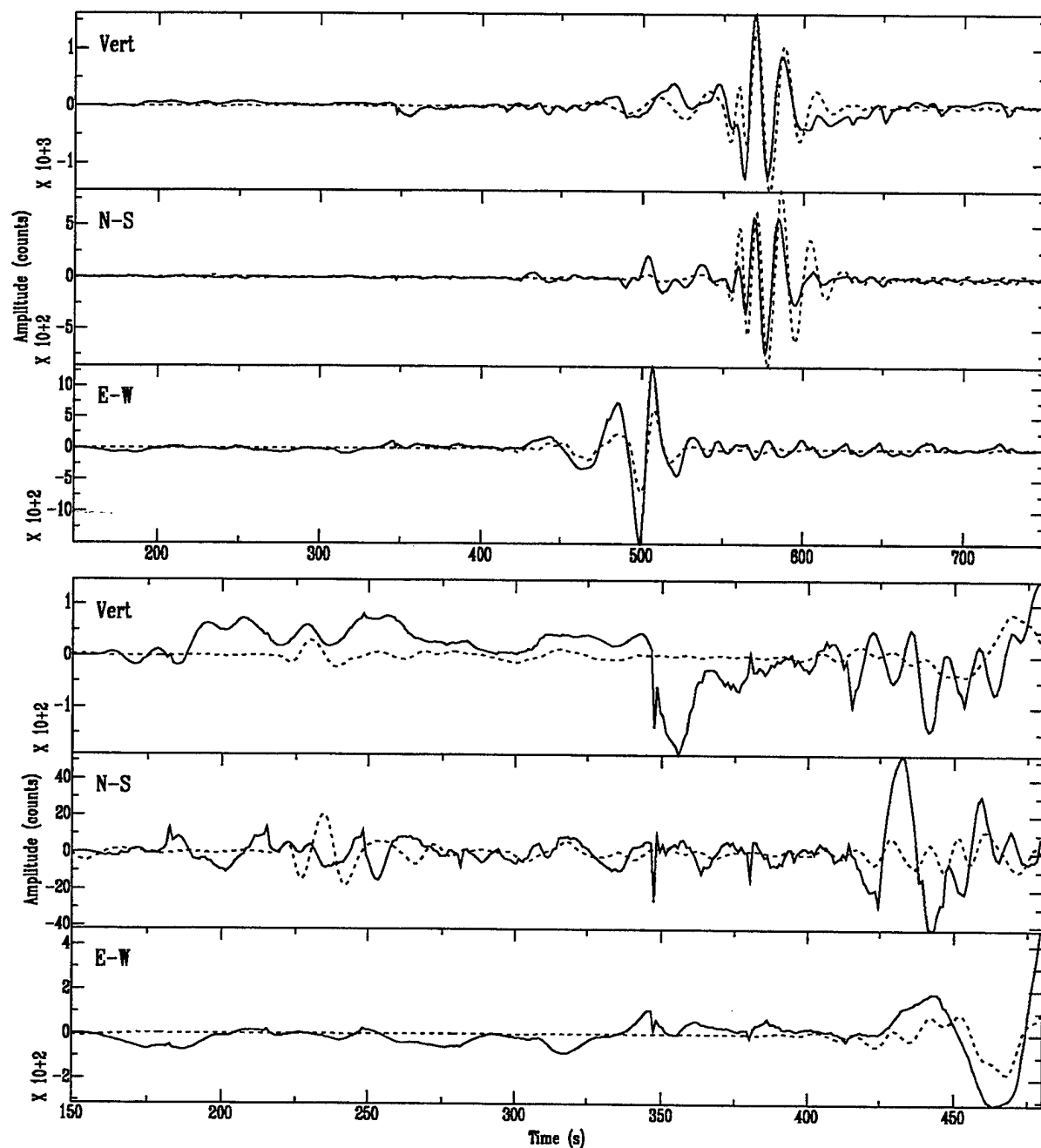
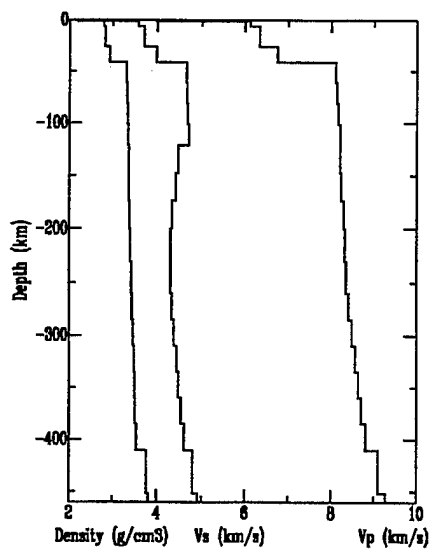


FIGURE B7



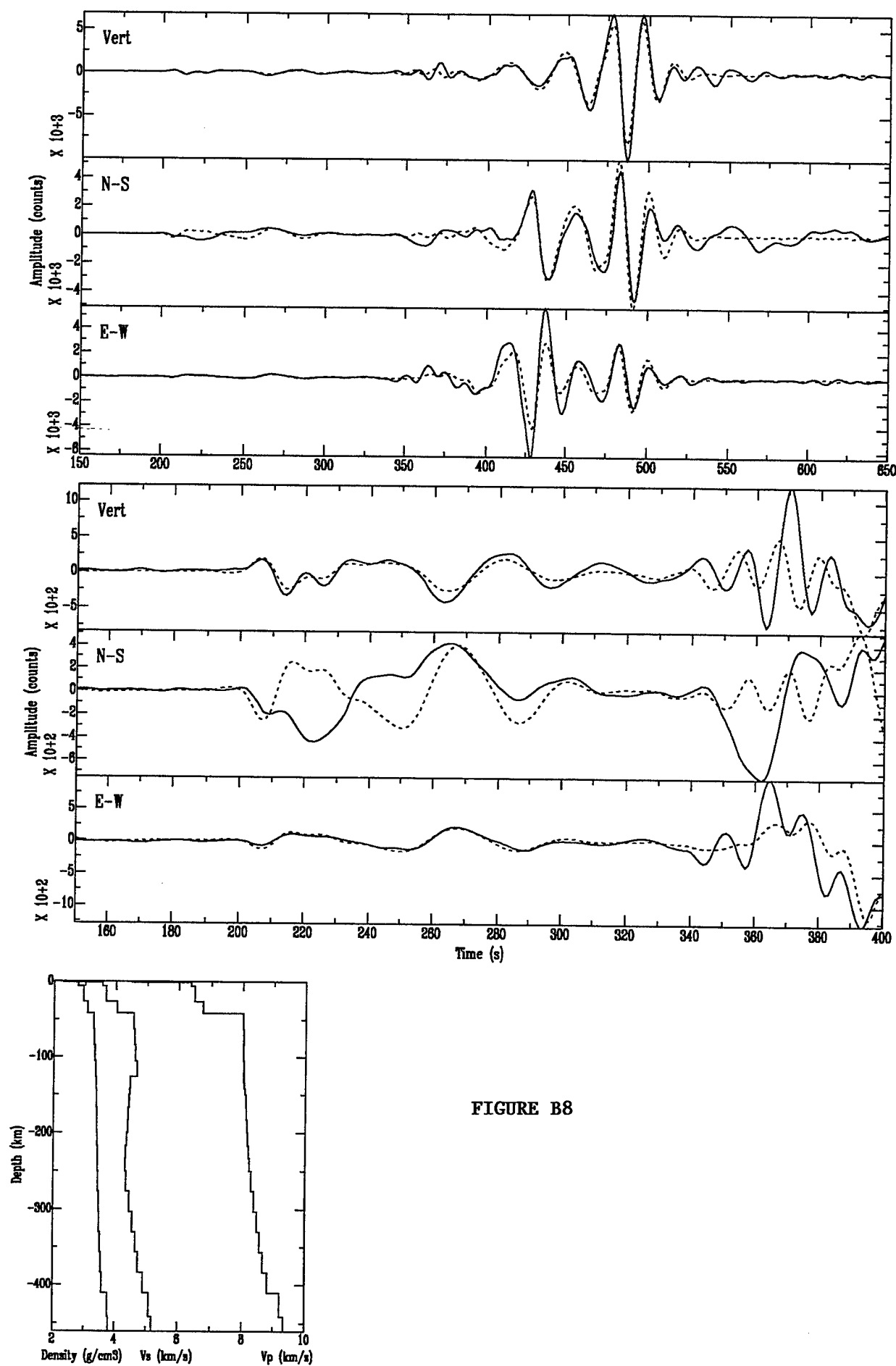


FIGURE B8

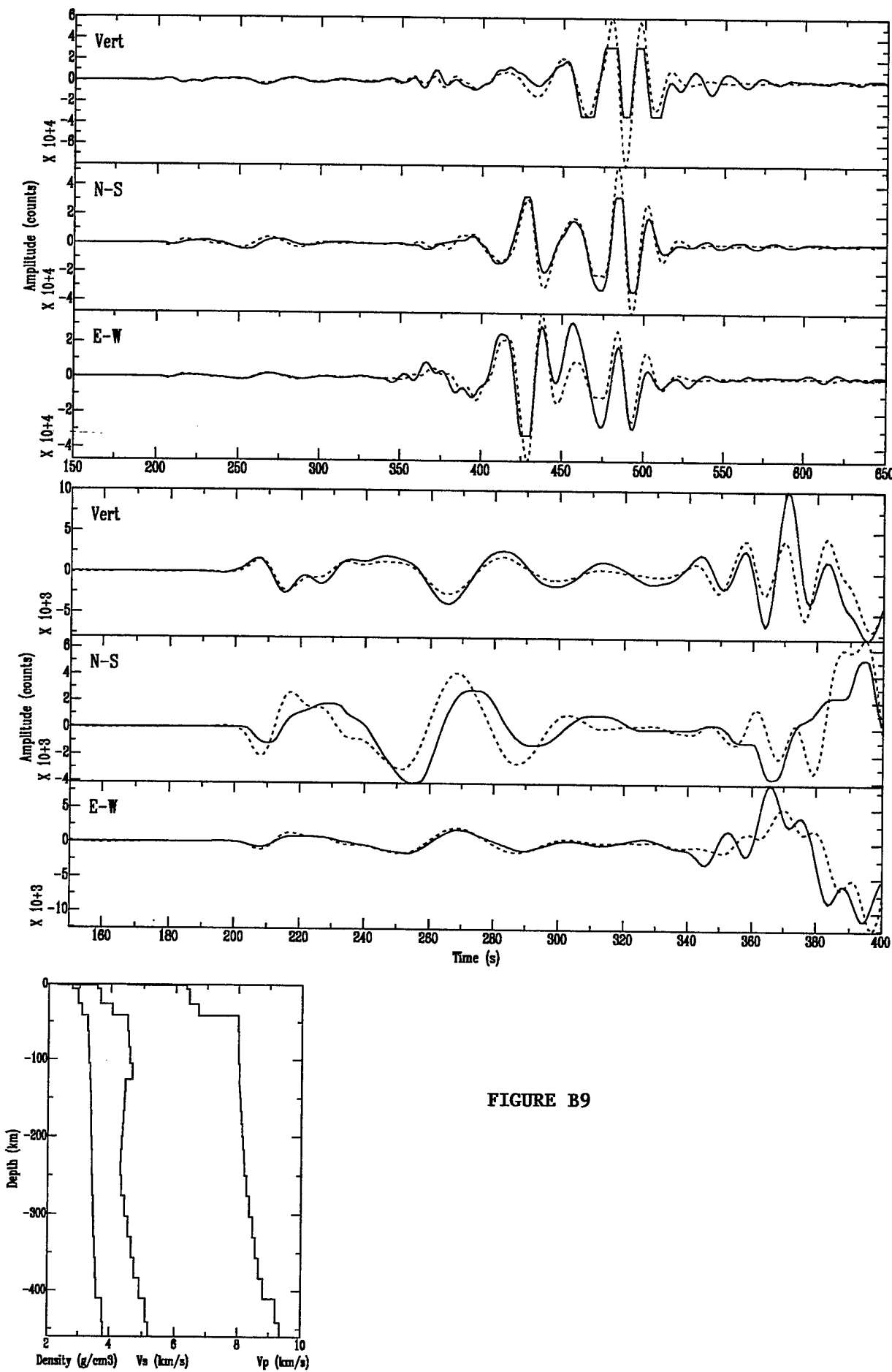


FIGURE B9

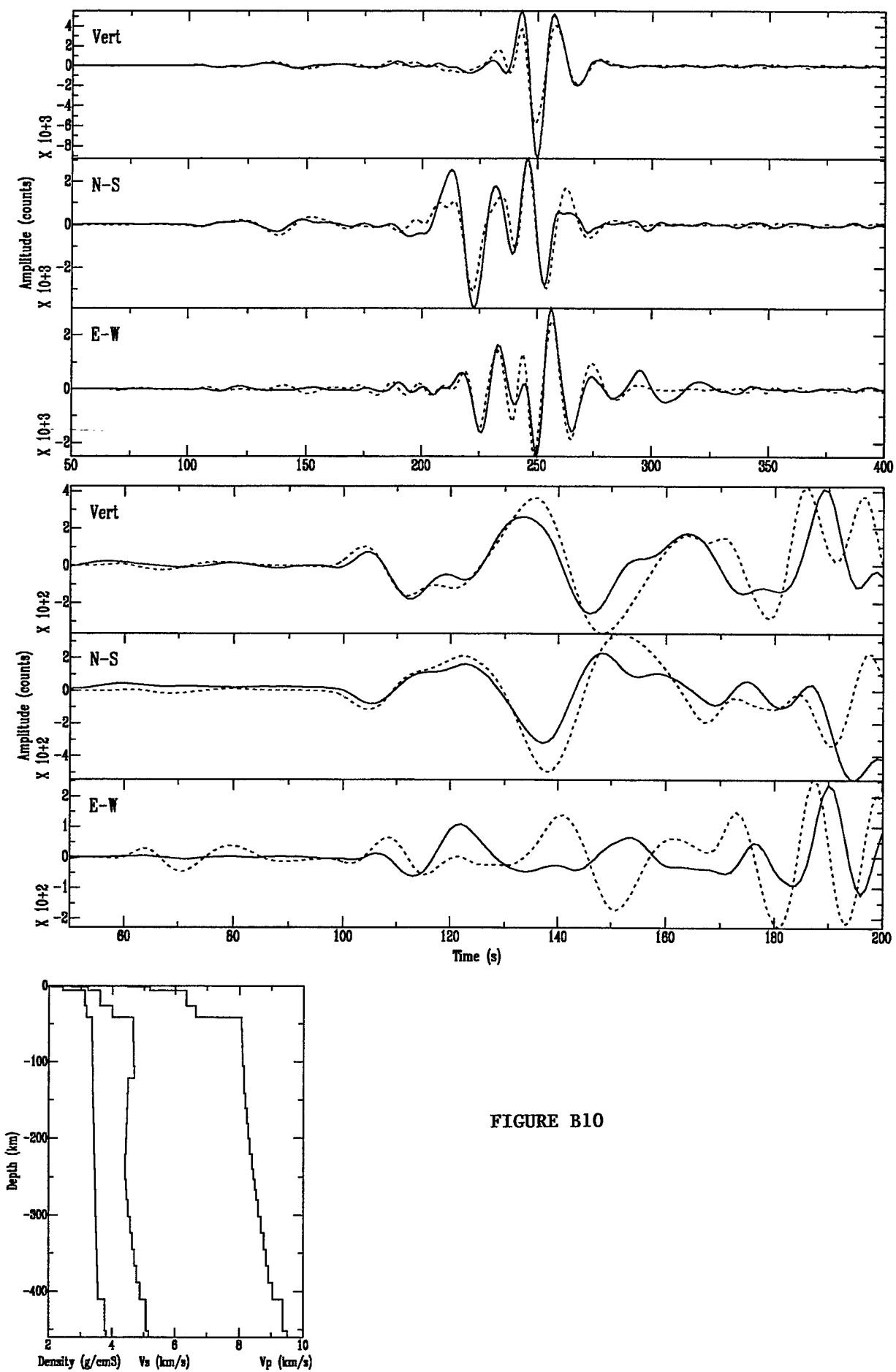


FIGURE B10

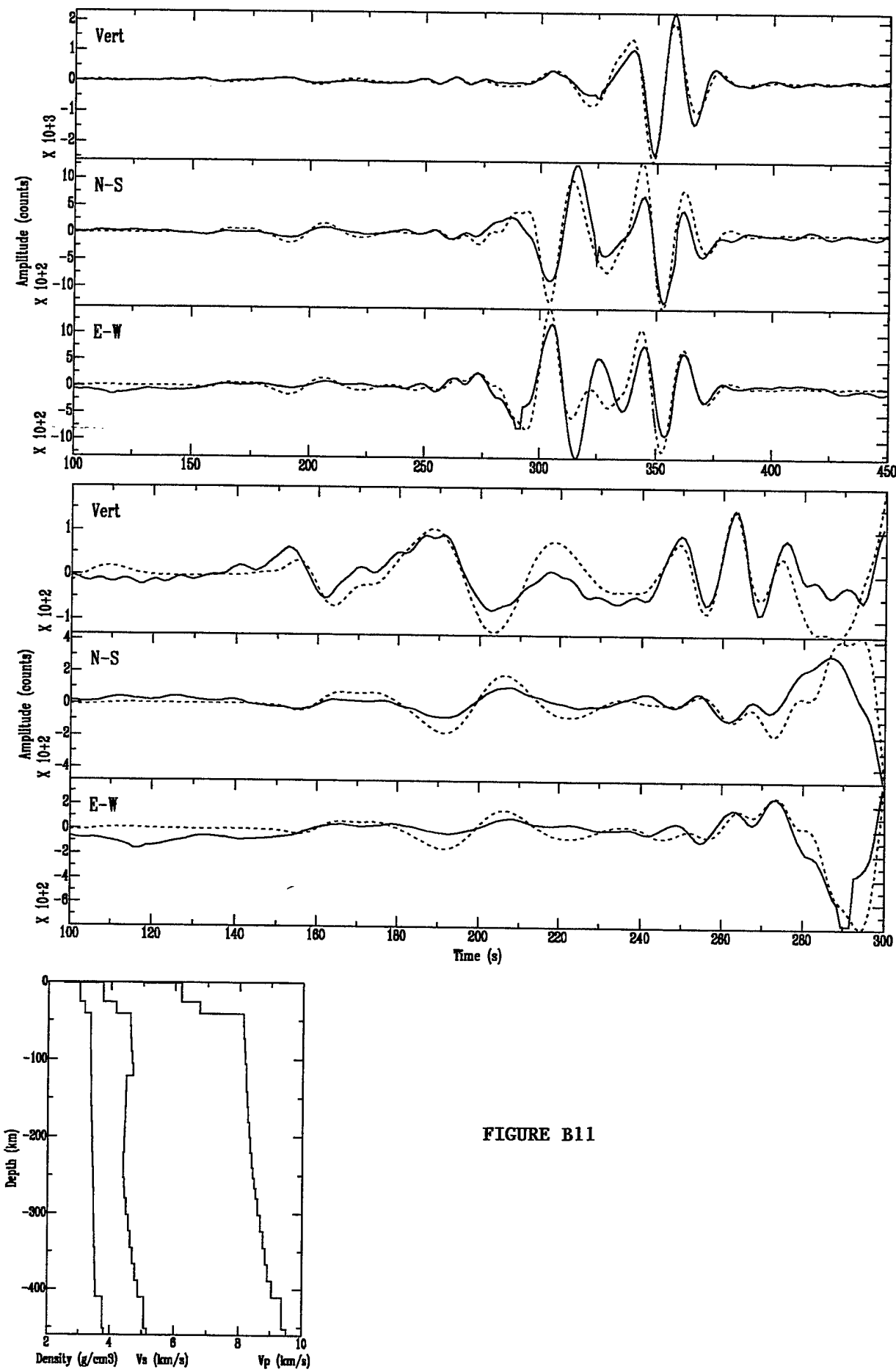
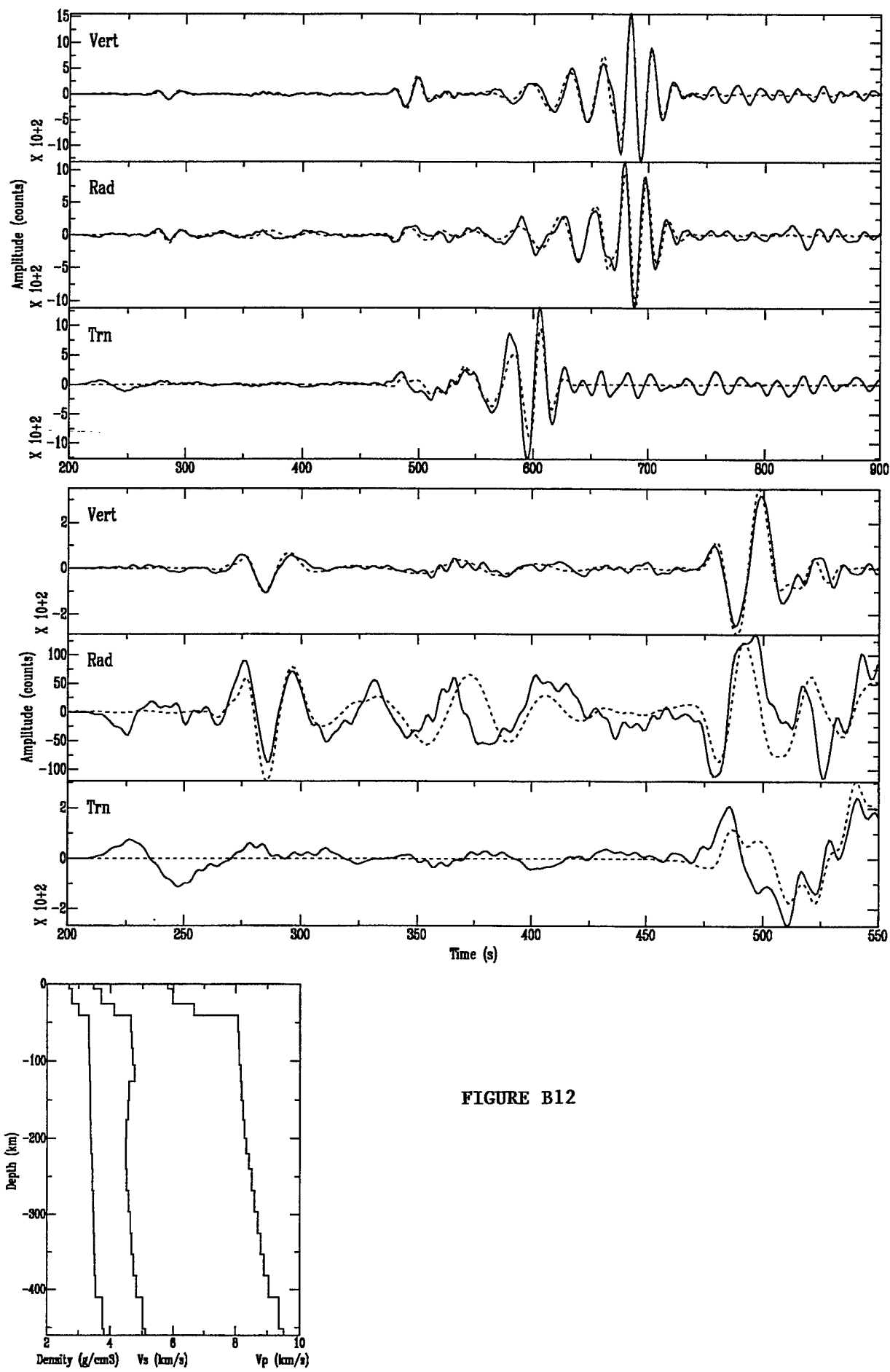


FIGURE B11



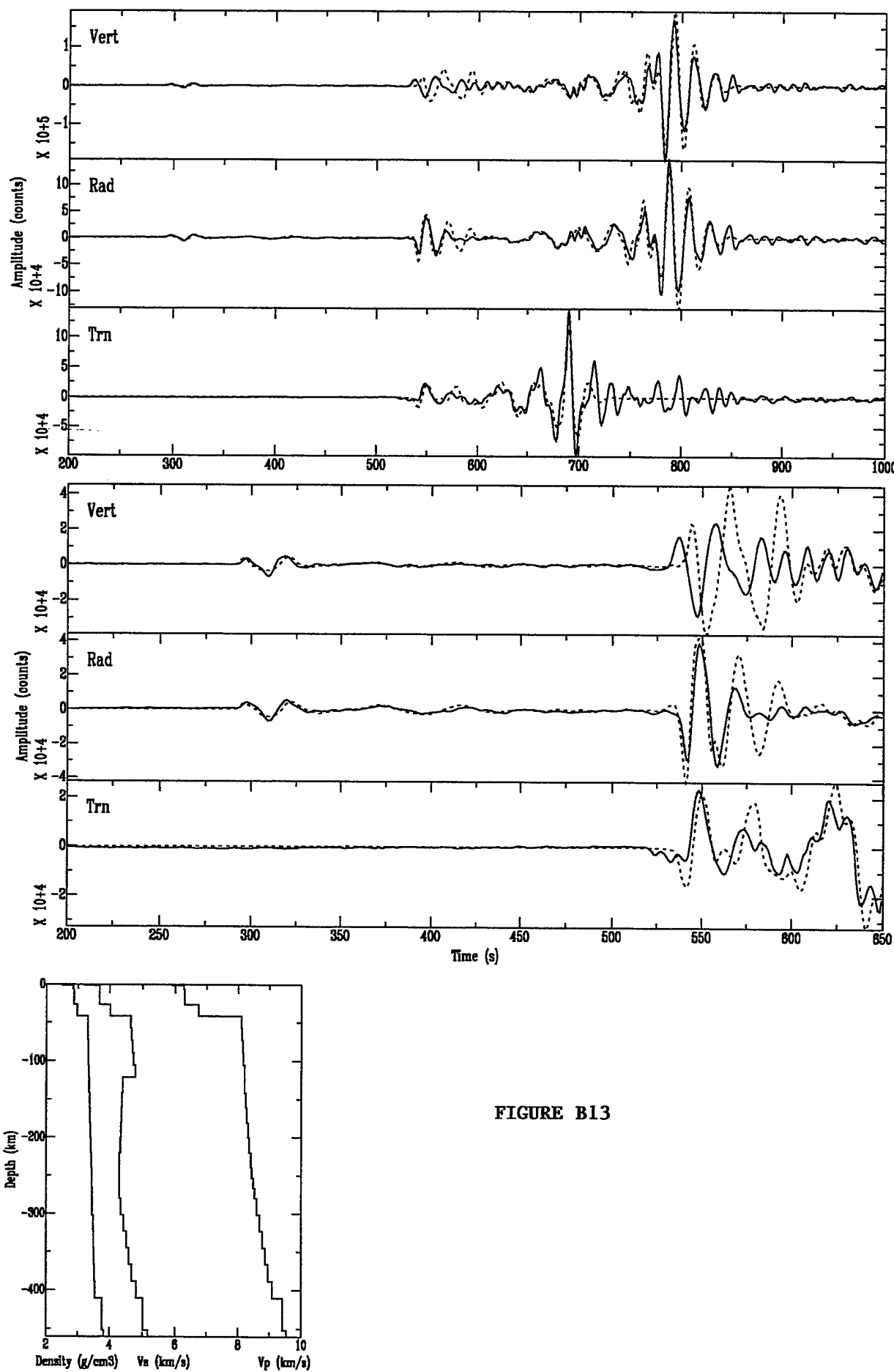


FIGURE B13

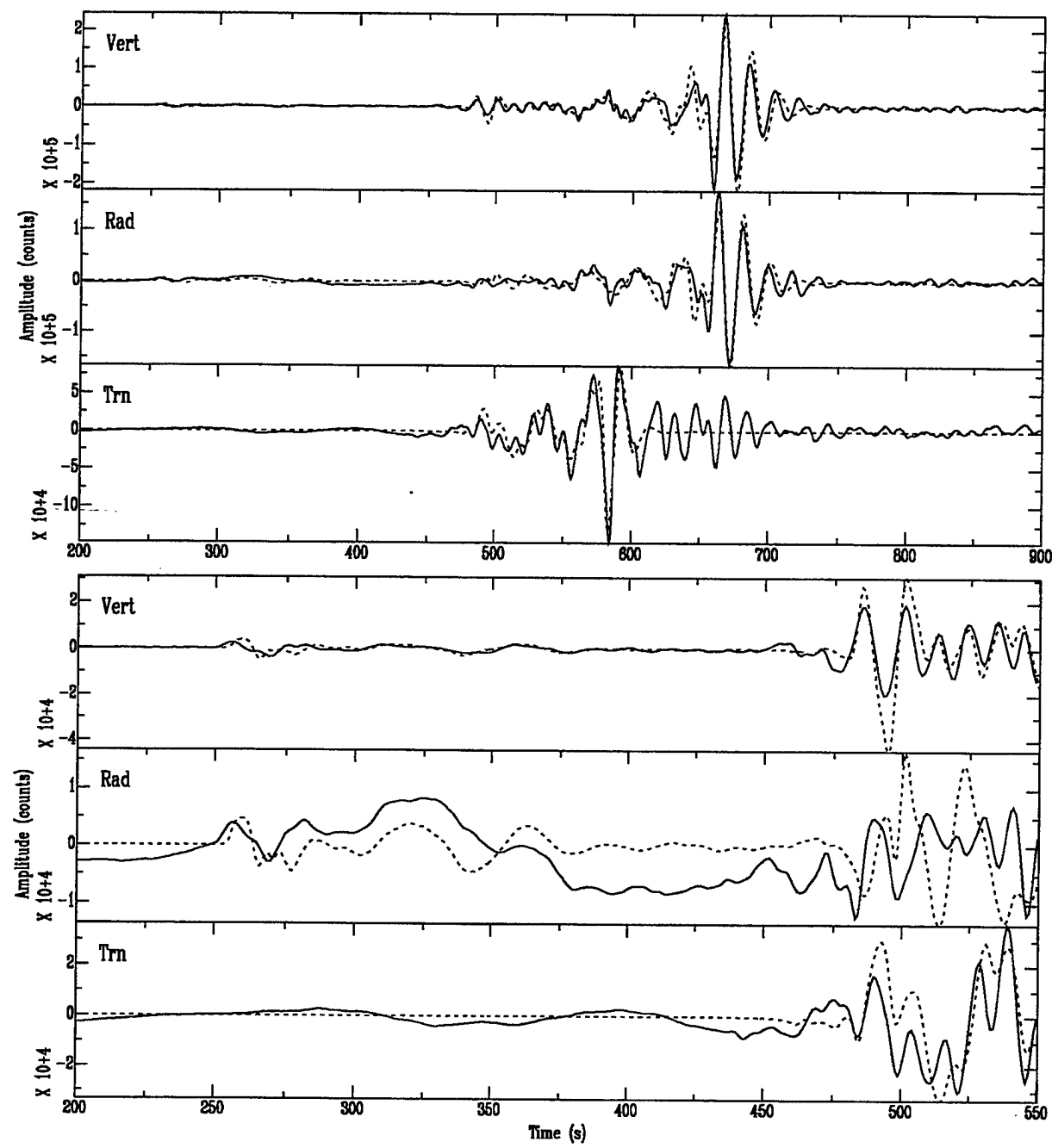
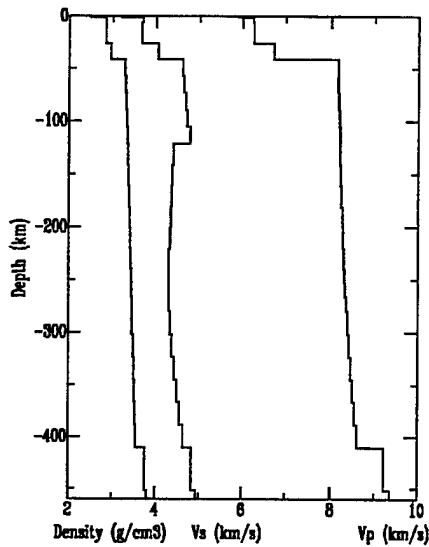


FIGURE B14



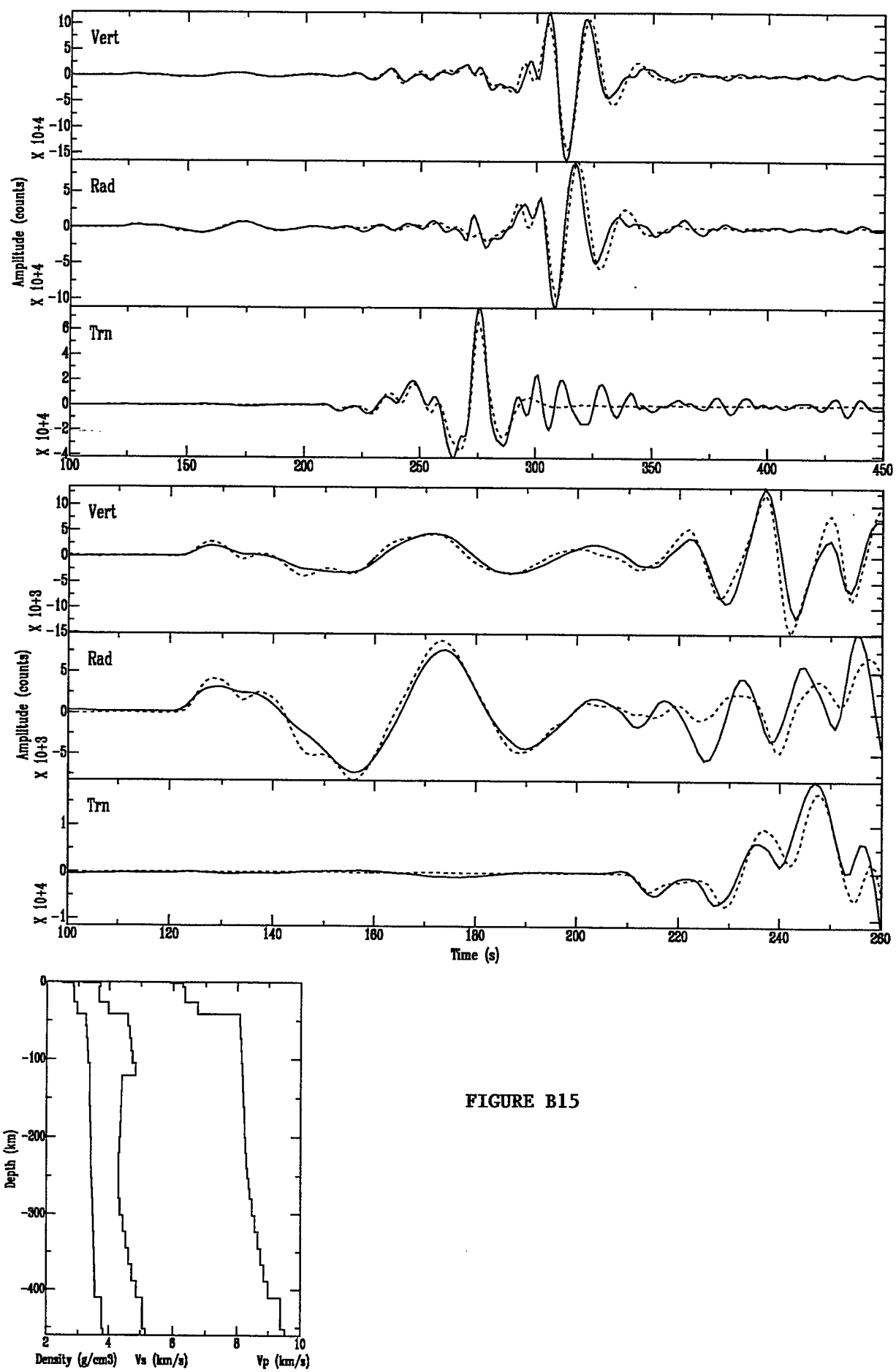
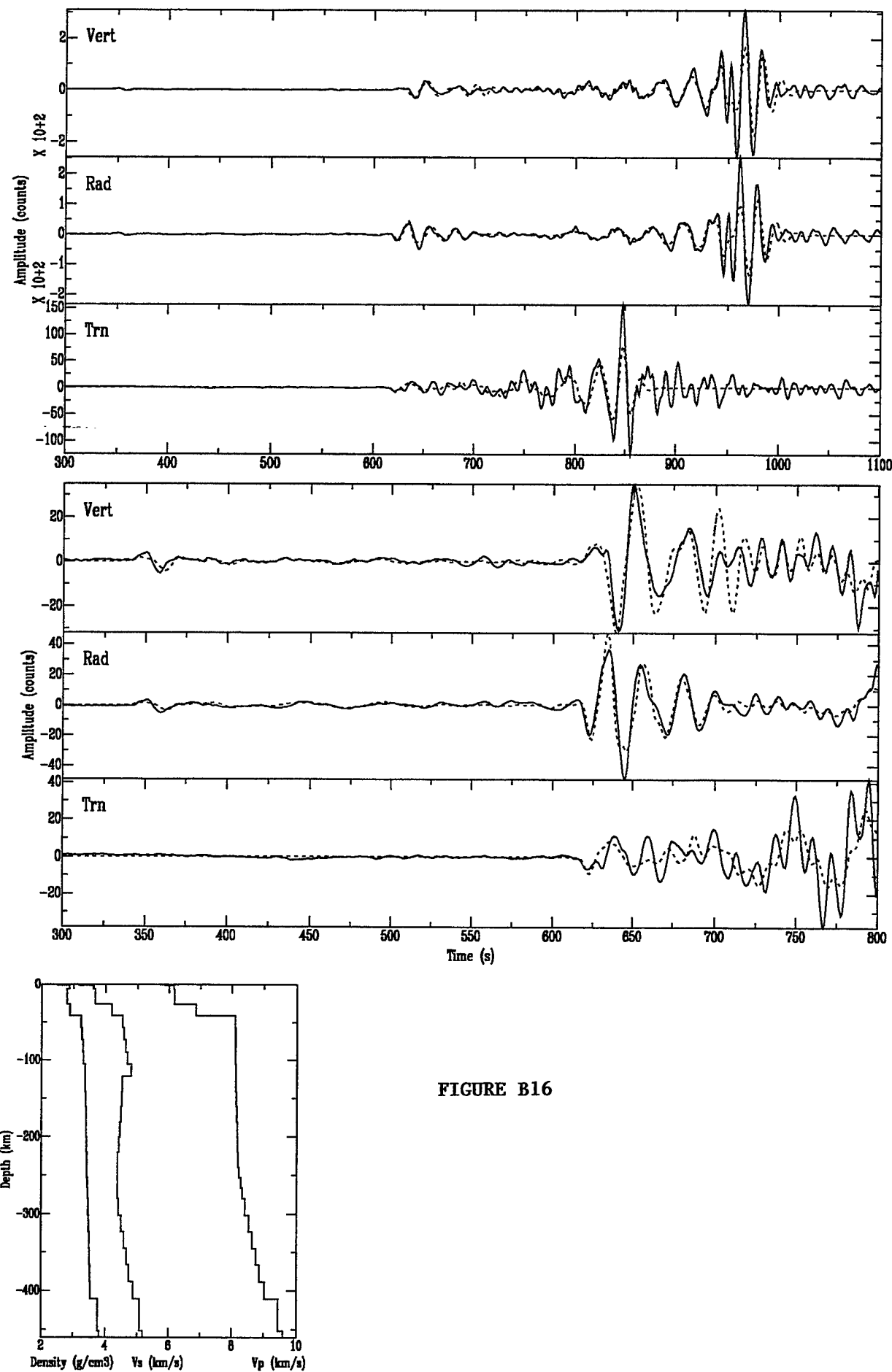


FIGURE B15



APPENDIX C Physical Properties

The proportions by weight of the end-members in the various phases were calculated from the molar concentrations, denoted by [], of the elements from the oxide proportions in Table C1. For olivine the molar concentrations of forsterite, Fo, and fayalite, Fa, were obtained from

$$Fo = \frac{[Mg]}{([Mg] + [Fe])}, \quad Fa = \frac{[Fe]}{([Mg] + [Fe])}$$

The corresponding expressions for pyroxenes are more complicated. If $[Al] > [Na]$, the proportions of jadeite, Jd, Ca-Tschermak, CaTs, and Aegirine, Ag, are first obtained from

$$Jd = [Na], \quad CaTs = ([Al] - [Na])/2, \quad Ag = 0$$

and the molar concentration of Ca reduced accordingly

$$[Ca] = [Ca] - CaTs$$

If $[Na] > [Al]$

$$Jd = [Al], \quad Ag = [Na] - [Al], \quad CaTs = 0$$

and the molar concentration of Fe is

$$[Fe] = [Fe] - Ag$$

The iron and magnesium are distributed between Hd & Fs, and Di & En by defining

$$F = \frac{[Mg]}{([Mg] + [Fe])}$$

then

$$Di = F[Ca], \quad En = ([Mg] - Di)/2$$

$$Hd = (1 - F)[Ca], \quad Fs = ([Fe] - Hd)/2$$

The expressions for Feldspar were obtained using

$$An = [Ca], \quad Al = [Na], \quad Or = [K]$$

The expressions for the spinels depend on whether all the Mg can be accommodated in Sp and Mc. If $[Mg] > ([Al] + [Cr])/2$ then

$$Sp = [Al]/2, \quad Mc = [Cr]/2$$

$$Mf = [Mg] - (Sp + Mc), \quad Mg = ([Fe] - Mf)/3$$

$$Hc = Cr = 0$$

If, however, this condition is not satisfied, but $[Mg] > [Cr]/2$, then

$$Mc = [Cr]/2, \quad Sp = [Mg] - Mc$$

$$Hc = [Al]/2 - Sp, \quad Mg = ([Fe] - Hc)/3$$

$$Mf = Cr = 0$$

Otherwise

$$Mc = [Mg], \quad Hc = [Al]/2$$

$$\text{Cr} = [\text{Cr}]/2 - \text{Mc}, \quad \text{Mg} = ([\text{Fe}] - \text{Hc} - \text{Cr})/3$$

$$\text{Sp} = \text{Mf} = 0$$

The expressions for garnet are less complicated. If F is defined by

$$F = \frac{[\text{Al}]}{([\text{Al}] + [\text{Cr}])}$$

then

$$\text{Py} = F[\text{Mg}], \quad \text{Al} = F[\text{Fe}], \quad \text{Gr} = F[\text{Ca}]$$

$$\text{Kn} = (1 - F)[\text{Mg}], \quad \text{Fc} = (1 - F)[\text{Fe}], \quad \text{Uv} = (1 - F)[\text{Ca}]$$

Once the molecular proportions of the end members had been obtained, their proportions by weight were calculated using the molecular weights in Table C1.

The densities of the end members are first corrected for the effect of temperature using

$$\rho(T) = \rho \left(1 - \alpha_1(T - 25) - \alpha_2(T - 25)^2 \right)$$

where $\alpha_2 = 0$ except for olivine, and T is the temperature in °C. Then the density and seismic velocities were calculated in two stages. First that for each individual phase was obtained from the proportions of the end members. That of the rock as a whole was then calculated from the proportions of each phase. The expressions are the same for each calculation

$$1/\bar{\rho} = \sum_{i=1}^N f_i/\rho_i, \quad V^V = \sum_{i=1}^N V_i f_i / \rho_i$$

$$1/V^R = \sum_{i=1}^N f_i/\rho_i V_i, \quad V^{VRH} = (V^V + V^R)/2$$

where f_i are the fractions by weight of the end members or of the mineral phases, and V_i is either the P or the S wave velocity. V^V is the Voigt, V^R the Reuss, and V^{VRH} the Voigt–Reuss–Hill average. The velocities for each mineral were corrected for the effect of temperature and pressure using

$$V(P, T) = V \left(1 + \frac{1}{V} \left(\frac{\partial V}{\partial T} \right) (T - 25) + \frac{1}{V} \left(\frac{\partial V}{\partial P} \right) P \right)$$

where P is the pressure in GPa. When the final P and S wave velocities of the rock had been obtained, the rock density was corrected for the effect of pressure using the bulk modulus calculated from the seismic velocities

$$\rho(T, P) = \rho(T, 0) \left(1 + P / \left(V_P^2 - \frac{4}{3} V_S^2 \right) \right)$$

The density and velocities calculated using these expressions are probably not accurate to better than 1–2%, and differences in density and velocity caused by differences in mineralogy to better than about 10%.

Table C1. Mineral Composition

	SiO ₂	TiO ₂	Al ₂ O ₃	Cr ₂ O ₃	FeO	MnO	MgO	CaO	Na ₂ O	K ₂ O	NiO	P ₂ O ₅
olivine	40.84	0.02	0.04	0.04	8.72	0.50	49.53	0.06	0.00	0.00	0.24	0.00
orthopyroxene	57.32	0.11	0.89	0.30	5.35	35.03	0.12	0.69	0.17	0.00	0.01	0.00
clinopyroxene	54.76	0.21	2.59	1.63	2.96	0.10	17.36	18.34	2.04	0.01	0.00	0.00
plagioclase	44.79	0.00	34.81	0.00	0.27	0.00	0.03	19.47	0.64	0.00	0.00	0.00
Al – spinel	0.00	0.13	65.55	0.00	11.94	0.10	22.28	0.00	0.00	0.00	0.00	0.00
Cr – spinel	0.12	0.14	10.28	59.40	17.06	0.14	12.62	0.14	0.00	0.00	0.00	0.00
garnet	41.74	0.43	20.21	3.99	7.68	0.37	20.40	5.11	0.05	0.00	0.00	0.00
amphibole	40.81	5.25	14.45	0.03	11.12	0.13	12.95	10.69	2.77	1.81	0.00	0.00
phlogopite	42.79	0.80	15.25	1.26	3.55	0.07	25.90	0.08	0.70	9.49	0.13	0.00
apatite	0.00	0.00	0.00	0.00	0.00	0.07	0.10	55.84	0.00	0.00	0.00	42.05

Calculated modal mineralogy of nodule suites

	mg#	ol	opx	cpx	gar	phl	Cr – sp
PKP	93.1	82.0	7.77	0.82	0.36	8.68	0.19
Depleted	92.8	78.2	15.3	1.67	3.65	0.64	0.46
GP & GPP	91.4	64.7	23.3	3.51	6.70	0.91	0.75
Fertile	90.5	62.5	20.2	7.08	9.49	0.41	0.25

Olivine

$$\frac{1}{V} \left(\frac{\partial V}{\partial T} \right) = -6.4 \times 10^{-5} \text{ } ^\circ\text{C}^{-1} \quad \frac{1}{V} \left(\frac{\partial V}{\partial P} \right) = 13 \times 10^{-3} \text{ GPa}^{-1}$$

	Forsterite Mg ₂ SiO ₄	Fayalite Fe ₂ SiO ₄
Fo	Fo	Fa
Mol. wt.	140.70	203.78
ρ Mg m ⁻³	3.225	4.392
α_1 °C ⁻¹	2.84×10^{-5}	2.76×10^{-5}
α_2 °C ⁻²	9.8×10^{-9}	5.1×10^{-9}
V_P km s ⁻¹	8.57	6.75
V_S km s ⁻¹	5.02	3.41

Pyroxene

$$\frac{1}{V} \left(\frac{\partial V}{\partial T} \right) = -8.2 \times 10^{-5} \text{ } ^\circ\text{C}^{-1} \quad \frac{1}{V} \left(\frac{\partial V}{\partial P} \right) = 26 \times 10^{-3} \text{ GPa}^{-1}$$

	Enstatite Mg ₂ Si ₂ O ₆ En	Ferrosilite Fe ₂ Si ₂ O ₆ Fs	Diopside CaMgSi ₂ O ₆ Di	Hedenbergite CaFeSi ₂ O ₆ Hd	Jadeite NaAlSi ₂ O ₆ Jd	Aegirine NaFeSi ₂ O ₆ Ag	Ca – Tschermak CaAl ₂ SiO ₆ CaTs
Mol. wt.	200.79	263.86	216.56	248.10	220.14	284.97	218.12
ρ Mg m ⁻³	3.194	3.998	3.277	3.632	3.347	3.576	3.43
α °C ⁻¹	2.9×10^{-5}	2.9×10^{-5}	3.2×10^{-5}	3.2×10^{-5}	3.0×10^{-5}	2.5×10^{-5}	2.6×10^{-5}
V_P km s ⁻¹	8.36	6.90	8.06	7.22	8.78	7.32	7.3
V_S km s ⁻¹	4.99	3.72	4.77	4.18	4.82	4.09	4.1

Feldspar

$$\frac{1}{V} \left(\frac{\partial V}{\partial T} \right) = -2.4 \times 10^{-5} \text{ } ^\circ\text{C}^{-1} \quad \frac{1}{V} \left(\frac{\partial V}{\partial P} \right) = 20 \times 10^{-3} \text{ GPa}^{-1}$$

	Anorthite CaAl ₂ Si ₂ O ₈ An	Albite NaAlSi ₃ O ₈ Al	Orthoclase KAlSi ₃ O ₈ Or
Mol. wt.	278.2	262.25	278.25
ρ Mg m ⁻³	2.762	2.611	2.56
α °C ⁻¹	5.9×10^{-5}	5.7×10^{-5}	9.4×10^{-6}
V_P km s ⁻¹	7.29	6.07	5.91
V_S km s ⁻¹	3.85	3.40	3.25

Spinel

$$\frac{1}{V} \left(\frac{\partial V}{\partial T} \right) = -20 \times 10^{-5} \text{ } ^\circ\text{C}^{-1} \quad \frac{1}{V} \left(\frac{\partial V}{\partial P} \right) = 16 \times 10^{-3} \text{ GPa}^{-1}$$

	Spinel MgAl ₂ O ₄ Sp	Magnesiochromite MgCr ₂ O ₄ Mc	Magnesioferrite MgFe ₂ O ₄ Mf	Hercynite FeAl ₂ O ₄ Hc	Chromite FeCr ₂ O ₄ Cr	Magnetite FeFe ₂ O ₄ Mg
Mol. wt.	142.27	192.29	199.99	173.81	223.84	231.54
ρ Mg m ⁻³	3.55	4.43	4.52	4.40	5.09	5.20
α °C ⁻¹	2.7×10^{-5}	2.2×10^{-5}	2.2×10^{-5}	2.4×10^{-5}	1.8×10^{-5}	4.2×10^{-5}
V_P km s ⁻¹	9.25	9.25	9.25	9.25	9.25	9.25
V_S km s ⁻¹	5.01	5.01	5.01	5.01	5.01	5.01

Garnet

$$\frac{1}{V} \left(\frac{\partial V}{\partial T} \right) = -4.8 \times 10^{-5} \text{ } ^\circ\text{C}^{-1} \quad \frac{1}{V} \left(\frac{\partial V}{\partial P} \right) = 8.5 \times 10^{-3} \text{ GPa}^{-1}$$

	Pyrope $\text{Mg}_3\text{Al}_2\text{Si}_3\text{O}_{12}$	Almandine $\text{Fe}_3\text{Al}_2\text{Si}_3\text{O}_{12}$	Grossular $\text{Ca}_3\text{Al}_2\text{Si}_3\text{O}_{12}$	Knorringleite $\text{Mg}_3\text{Cr}_2\text{Si}_3\text{O}_{12}$	-	Uvarovite $\text{Ca}_3\text{Cr}_2\text{Si}_3\text{O}_{12}$
	Py Py	Al Al	Gr Gr	Kn Kn	Fc Fc	Uv Uv
Mol. wt.	403.15	497.76	450.45	453.13	547.78	500.48
$\rho \text{ Mg m}^{-3}$	3.582	4.318	3.594	3.852	4.578	3.848
$\alpha \text{ } ^\circ\text{C}^{-1}$	2.6×10^{-5}	2.6×10^{-5}	2.3×10^{-5}	2.3×10^{-5}	2.0×10^{-5}	2.5×10^{-5}
$V_P \text{ km s}^{-1}$	8.96	8.42	9.31	8.50	7.99	8.88
$V_S \text{ km s}^{-1}$	5.05	4.68	5.43	4.79	4.44	5.18

	Amphibole	Phlogopite	Apatite
$\rho \text{ Mg m}^{-3}$	3.05	3.2	3.2
$\alpha \text{ } ^\circ\text{C}^{-1}$	4×10^{-5}	4×10^{-5}	4×10^{-5}
$V_P \text{ km s}^{-1}$	7.04	5.55	7.94
$V_S \text{ km s}^{-1}$	3.81	2.88	4.81

$$\frac{1}{V} \left(\frac{\partial V}{\partial T} \right) = -9 \times 10^{-5} \text{ } ^\circ\text{C}^{-1} \quad \frac{1}{V} \left(\frac{\partial V}{\partial P} \right) = 30 \times 10^{-3} \text{ GPa}^{-1}$$

THOMAS AHRENS
SEISMOLOGICAL LABORATORY 252-21
CALIFORNIA INSTITUTE OF TECHNOLOGY
PASADENA, CA 91125

RALPH ALEWINE
NTPO
1901 N. MOORE STREET, SUITE 609
ARLINGTON, VA 22209

SHELTON ALEXANDER
PENNSYLVANIA STATE UNIVERSITY
DEPARTMENT OF GEOSCIENCES
537 DEIKE BUILDING
UNIVERSITY PARK, PA 16801

MUAWIA BARAZANGI
INSTITUTE FOR THE STUDY OF THE CONTINENTS
3126 SNEE HALL
CORNELL UNIVERSITY
ITHACA, NY 14853

RICHARD BARDZELL
ACIS
DCI/ACIS
WASHINGTON, DC 20505

T.G. BARKER
MAXWELL TECHNOLOGIES
P.O. BOX 23558
SAN DIEGO, CA 92123

DOUGLAS BAUMGÄRTT
ENSCO INC.
5400 PORT ROYAL ROAD
SPRINGFIELD, VA 22151

HERON J. BENNETT
MAXWELL TECHNOLOGIES
11800 SUNRISE VALLEY DRIVE SUITE 1212
RESTON, VA 22091

WILLIAM BENSON
NAS/COS
ROOM HA372
2001 WISCONSIN AVE. NW
WASHINGTON, DC 20007

JONATHAN BERGER
UNIVERSITY OF CA, SAN DIEGO
SCRIPPS INSTITUTION OF OCEANOGRAPHY IGPP, 0225
9500 GILMAN DRIVE
LA JOLLA, CA 92093-0225

ROBERT BLANDFORD
AFTAC
1300 N. 17TH STREET
SUITE 1450
ARLINGTON, VA 22209-2308

STEVEN BRATT
NTPO
1901 N. MOORE STREET, SUITE 609
ARLINGTON, VA 22209

RHETT BUTLER
IRIS
1616 N. FORT MEYER DRIVE
SUITE 1050
ARLINGTON, VA 22209

LESLIE A. CASEY
DOE
1000 INDEPENDENCE AVE. SW
NN-40
WASHINGTON, DC 20585-0420

CATHERINE DE GROOT-HEDLIN
SCRIPPS INSTITUTION OF OCEANOGRAPHY
UNIVERSITY OF CALIFORNIA, SAN DIEGO
INSTITUTE OF GEOPHYSICS AND PLANETARY PHYSICS
LA JOLLA, CA 92093

STANLEY DICKINSON
AFOSR
110 DUNCAN AVENUE, SUITE B115
BOLLING AFB
WASHINGTON, D.C. 20332-001

SEAN DORAN
ACIS
DCI/ACIS
WASHINGTON , DC 20505

DIANE I. DOSER
DEPARTMENT OF GEOLOGICAL SCIENCES
THE UNIVERSITY OF TEXAS AT EL PASO
EL PASO, TX 79968

RICHARD J. FANTEL
BUREAU OF MINES
DEPT OF INTERIOR, BLDG 20
DENVER FEDERAL CENTER
DENVER, CO 80225

JOHN FILSON
ACIS/TMG/NTT
ROOM 6T11 NHB
WASHINGTON, DC 20505

MARK D. FISK
MISSION RESEARCH CORPORATION
735 STATE STREET
P.O. DRAWER 719
SANTA BARBARA, CA 93102-0719

LORI GRANT
MULTIMAX, INC.
311C FOREST AVE. SUITE 3
PACIFIC GROVE, CA 93950

I. N. GUPTA
MULTIMAX, INC.
1441 MCCORMICK DRIVE
LARGO, MD 20774

JAMES HAYES
NSF
4201 WILSON BLVD., ROOM 785
ARLINGTON, VA 22230

MICHAEL HEDLIN
UNIVERSITY OF CALIFORNIA, SAN DIEGO
SCRIPPS INSTITUTION OF OCEANOGRAPHY IGPP, 0225
9500 GILMAN DRIVE
LA JOLLA, CA 92093-0225

EUGENE HERRIN
SOUTHERN METHODIST UNIVERSITY
DEPARTMENT OF GEOLOGICAL SCIENCES
DALLAS, TX 75275-0395

VINDELL HSU
HQ/AFTAC/TTR
1030 S. HIGHWAY A1A
PATRICK AFB, FL 32925-3002

RONG-SONG JIH
PHILLIPS LABORATORY
EARTH SCIENCES DIVISION
29 RANDOLPH ROAD
HANSOM AFB, MA 01731-3010

LAWRENCE LIVERMORE NATIONAL LABORATORY
ATTN: TECHNICAL STAFF (PLS ROUTE)
PO BOX 808, MS L-200
LIVERMORE, CA 94551

LAWRENCE LIVERMORE NATIONAL LABORATORY
ATTN: TECHNICAL STAFF (PLS ROUTE)
PO BOX 808, MS L-221
LIVERMORE, CA 94551

ROBERT GEIL
DOE
PALAIS DES NATIONS, RM D615
GENEVA 10, SWITZERLAND

HENRY GRAY
SMU STATISTICS DEPARTMENT
P.O. BOX 750302
DALLAS, TX 75275-0302

DAVID HARKRIDER
PHILLIPS LABORATORY
EARTH SCIENCES DIVISION
29 RANDOLPH ROAD
HANSOM AFB, MA 01731-3010

THOMAS HEARN
NEW MEXICO STATE UNIVERSITY
DEPARTMENT OF PHYSICS
LAS CRUCES, NM 88003

DONALD HELMBERGER
CALIFORNIA INSTITUTE OF TECHNOLOGY
DIVISION OF GEOLOGICAL & PLANETARY SCIENCES
SEISMOLOGICAL LABORATORY
PASADENA, CA 91125

ROBERT HERRMANN
ST. LOUIS UNIVERSITY
DEPARTMENT OF EARTH & ATMOSPHERIC SCIENCES
3507 LACLEDE AVENUE
ST. LOUIS, MO 63103

ANTHONY IANNACCHIONE
BUREAU OF MINES
COCHRANE MILL ROAD
PO BOX 18070
PITTSBURGH, PA 15236-9986

THOMAS JORDAN
MASSACHUSETTS INSTITUTE OF TECHNOLOGY
EARTH, ATMOSPHERIC & PLANETARY SCIENCES
77 MASSACHUSETTS AVENUE, 54-918
CAMBRIDGE, MA 02139

LAWRENCE LIVERMORE NATIONAL LABORATORY
ATTN: TECHNICAL STAFF (PLS ROUTE)
PO BOX 808, MS L-207
LIVERMORE, CA 94551

LAWRENCE LIVERMORE NATIONAL LABORATORY
ATTN: TECHNICAL STAFF (PLS ROUTE)
LLNL
PO BOX 808, MS L-175
LIVERMORE, CA 94551

LAWRENCE LIVERMORE NATIONAL LABORATORY
ATTN: TECHNICAL STAFF (PLS ROUTE)
PO BOX 808, MS L-208
LIVERMORE, CA 94551

LAWRENCE LIVERMORE NATIONAL LABORATORY
ATTN: TECHNICAL STAFF (PLS ROUTE)
PO BOX 808, MS L-202
LIVERMORE, CA 94551

LAWRENCE LIVERMORE NATIONAL LABORATORY
ATTN: TECHNICAL STAFF (PLS ROUTE)
PO BOX 808, MS L-195
LIVERMORE, CA 94551

LAWRENCE LIVERMORE NATIONAL LABORATORY
ATTN: TECHNICAL STAFF (PLS ROUTE)
PO BOX 808, MS L-205
LIVERMORE, CA 94551

THORNE LAY
UNIVERSITY OF CALIFORNIA, SANTA CRUZ
EARTH SCIENCES DEPARTMENT
EARTH & MARINE SCIENCE BUILDING
SANTA CRUZ, CA 95064

ANATOLI L. LEVSHIN
DEPARTMENT OF PHYSICS
UNIVERSITY OF COLORADO
CAMPUS BOX 390
BOULDER, CO 80309-0309

DONALD A. LINGER
DNA
6801 TELEGRAPH ROAD
ALEXANDRIA, VA 22310

LOS ALAMOS NATIONAL LABORATORY
ATTN: TECHNICAL STAFF (PLS ROUTE)
PO BOX 1663, MS F659
LOS ALAMOS, NM 87545

LOS ALAMOS NATIONAL LABORATORY
ATTN: TECHNICAL STAFF (PLS ROUTE)
PO BOX 1663, MS F665
LOS ALAMOS, NM 87545

LOS ALAMOS NATIONAL LABORATORY
ATTN: TECHNICAL STAFF (PLS ROUTE)
PO BOX 1663, MS D460
LOS ALAMOS, NM 87545

LOS ALAMOS NATIONAL LABORATORY
ATTN: TECHNICAL STAFF (PLS ROUTE)
PO BOX 1663, MS C335
LOS ALAMOS, NM 87545

GARY MCCARTOR
SOUTHERN METHODIST UNIVERSITY
DEPARTMENT OF PHYSICS
DALLAS, TX 75275-0395

KEITH MC LAUGHLIN
MAXWELL TECHNOLOGIES
P.O. BOX 23558
SAN DIEGO, CA 92123

BRIAN MITCHELL
DEPARTMENT OF EARTH & ATMOSPHERIC SCIENCES
ST. LOUIS UNIVERSITY
3507 LACLEDE AVENUE
ST. LOUIS, MO 63103

RICHARD MORROW
USACDA/TVI
320 21ST STREET, N.W.
WASHINGTON, DC 20451

JOHN MURPHY
MAXWELL TECHNOLOGIES
11800 SUNRISE VALLEY DRIVE SUITE 1212
RESTON, VA 22091

JAMES NI
NEW MEXICO STATE UNIVERSITY
DEPARTMENT OF PHYSICS
LAS CRUCES, NM 88003

CHARLES ODDENINO
BUREAU OF MINES
810 7TH ST. NW
WASHINGTON, DC 20241

JOHN ORCUTT
INSTITUTE OF GEOPHYSICS AND PLANETARY PHYSICS
UNIVERSITY OF CALIFORNIA, SAN DIEGO
LA JOLLA, CA 92093

PACIFIC NORTHWEST NATIONAL LABORATORY
ATTN: TECHNICAL STAFF (PLS ROUTE)
PO BOX 999, MS K6-48
RICHLAND, WA 99352

PACIFIC NORTHWEST NATIONAL LABORATORY
ATTN: TECHNICAL STAFF (PLS ROUTE)
PO BOX 999, MS K7-34
RICHLAND, WA 99352

PACIFIC NORTHWEST NATIONAL LABORATORY
ATTN: TECHNICAL STAFF (PLS ROUTE)
PO BOX 999, MS K7-22
RICHLAND, WA 99352

PACIFIC NORTHWEST NATIONAL LABORATORY
ATTN: TECHNICAL STAFF (PLS ROUTE)
PO BOX 999, MS K6-84
RICHLAND, WA 99352

FRANK PILOTTE
HQ/AFTAC/TT
1030 S. HIGHWAY A1A
PATRICK AFB, FL 32925-3002

JAY PULLI
RADIX SYSTEMS, INC.
6 TAFT COURT
ROCKVILLE, MD 20850

DAVID RUSSELL
HQ AFTAC/TTR
1030 SOUTH HIGHWAY A1A
PATRICK AFB, FL 32925-3002

SANDIA NATIONAL LABORATORY
ATTN: TECHNICAL STAFF (PLS ROUTE)
DEPT. 5704
MS 0979, PO BOX 5800
ALBUQUERQUE, NM 87185-0979

SANDIA NATIONAL LABORATORY
ATTN: TECHNICAL STAFF (PLS ROUTE)
DEPT. 5791
MS 0567, PO BOX 5800
ALBUQUERQUE, NM 87185-0567

SANDIA NATIONAL LABORATORY
ATTN: TECHNICAL STAFF (PLS ROUTE)
DEPT. 5704
MS 0655, PO BOX 5800
ALBUQUERQUE, NM 87185-0655

SANDIA NATIONAL LABORATORY
ATTN: TECHNICAL STAFF (PLS ROUTE)
DEPT. 6116
MS 0750, PO BOX 5800
ALBUQUERQUE, NM 87185-0750

PACIFIC NORTHWEST NATIONAL LABORATORY
ATTN: TECHNICAL STAFF (PLS ROUTE)
PO BOX 999, MS K6-40
RICHLAND, WA 99352

PACIFIC NORTHWEST NATIONAL LABORATORY
ATTN: TECHNICAL STAFF (PLS ROUTE)
PO BOX 999, MS K5-72
RICHLAND, WA 99352

PACIFIC NORTHWEST NATIONAL LABORATORY
ATTN: TECHNICAL STAFF (PLS ROUTE)
PO BOX 999, MS K5-12
RICHLAND, WA 99352

KEITH PRIESTLEY
DEPARTMENT OF EARTH SCIENCES
UNIVERSITY OF CAMBRIDGE
MADINGLEY RISE, MADINGLEY ROAD
CAMBRIDGE, CB3 OEZ UK

PAUL RICHARDS
COLUMBIA UNIVERSITY
LAMONT-DOHERTY EARTH OBSERVATORY
PALISADES, NY 10964

CHANDAN SAIKIA
WOODWARD-CLYDE FEDERAL SERVICES
566 EL DORADO ST., SUITE 100
PASADENA, CA 91101-2560

SANDIA NATIONAL LABORATORY
ATTN: TECHNICAL STAFF (PLS ROUTE)
DEPT. 4115
MS 0329, PO BOX 5800
ALBUQUERQUE, NM 87185-0329

SANDIA NATIONAL LABORATORY
ATTN: TECHNICAL STAFF (PLS ROUTE)
DEPT. 9311
MS 1159, PO BOX 5800
ALBUQUERQUE, NM 87185-1159

SANDIA NATIONAL LABORATORY
ATTN: TECHNICAL STAFF (PLS ROUTE)
DEPT. 5736
MS 0655, PO BOX 5800
ALBUQUERQUE, NM 87185-0655

THOMAS SERENO JR.
SCIENCE APPLICATIONS INTERNATIONAL
CORPORATION
10260 CAMPUS POINT DRIVE
SAN DIEGO, CA 92121

AVI SHAPIRA
SEISMOLOGY DIVISION
THE INSTITUTE FOR PETROLEUM RESEARCH AND
GEOPHYSICS
P.O.B. 2286, NOLON 58122 ISRAEL

MATTHEW SIBOL
ENSCO, INC.
445 PINEDA COURT
MELBOURNE, FL 32940

JEFFRY STEVENS
MAXWELL TECHNOLOGIES
P.O. BOX 23558
SAN DIEGO, CA 92123

DAVID THOMAS
ISEE
29100 AURORA ROAD
CLEVELAND, OH 44139

LAWRENCE TURNBULL
ACIS
DCI/ACIS
WASHINGTON, DC 20505

FRANK VERNON
UNIVERSITY OF CALIFORNIA, SAN DIEGO
SCRIPPS INSTITUTION OF OCEANOGRAPHY IGPP, 0225
9500 GILMAN DRIVE
LA JOLLA, CA 92093-0225

DANIEL WEILL
NSF
EAR-785
4201 WILSON BLVD., ROOM 785
ARLINGTON, VA 22230

RU SHAN WU
UNIVERSITY OF CALIFORNIA SANTA CRUZ
EARTH SCIENCES DEPT.
1156 HIGH STREET
SANTA CRUZ, CA 95064

JAMES E. ZOLLWEG
BOISE STATE UNIVERSITY
GEOSCIENCES DEPT.
1910 UNIVERSITY DRIVE
BOISE, ID 83725

DEFENSE TECHNICAL INFORMATION CENTER
8725 JOHN J. KINGMAN ROAD
FT BELVOIR, VA 22060-6218 (2 COPIES)

ROBERT SHUMWAY
410 MRAK HALL
DIVISION OF STATISTICS
UNIVERSITY OF CALIFORNIA
DAVIS, CA 95616-8671

DAVID SIMPSON
IRIS
1616 N. FORT MEYER DRIVE
SUITE 1050
ARLINGTON, VA 22209

BRIAN SULLIVAN
BOSTON COLLEGE
INSITUTE FOR SPACE RESEARCH
140 COMMONWEALTH AVENUE
CHESTNUT HILL, MA 02167

NAFI TOKSOZ
EARTH RESOURCES LABORATORY, M.I.T.
42 CARLTON STREET, E34-440
CAMBRIDGE, MA 02142

GREG VAN DER VINK
IRIS
1616 N. FORT MEYER DRIVE
SUITE 1050
ARLINGTON, VA 22209

TERRY WALLACE
UNIVERSITY OF ARIZONA
DEPARTMENT OF GEOSCIENCES
BUILDING #77
TUCSON, AZ 85721

JAMES WHITCOMB
NSF
NSF/ISC OPERATIONS/EAR-785
4201 WILSON BLVD., ROOM785
ARLINGTON, VA 22230

JIAKANG XIE
COLUMBIA UNIVERSITY
LAMONT DOHERTY EARTH OBSERVATORY
ROUTE 9W
PALISADES, NY 10964

OFFICE OF THE SECRETARY OF DEFENSE
DDR&E
WASHINGTON, DC 20330

TACTEC
BATTELLE MEMORIAL INSTITUTE
505 KING AVENUE
COLUMBUS, OH 43201 (FINAL REPORT)

PHILLIPS LABORATORY
ATTN: XPG
29 RANDOLPH ROAD
HANSCOM AFB, MA 01731-3010

PHILLIPS LABORATORY
ATTN: GPE
29 RANDOLPH ROAD
HANSCOM AFB, MA 01731-3010

PHILLIPS LABORATORY
ATTN: TSML
5 WRIGHT STREET
HANSCOM AFB, MA 01731-3004

PHILLIPS LABORATORY
ATTN: PL/SUL
3550 ABERDEEN AVE SE
KIRTLAND, NM 87117-5776 (2 COPIES)